Dynamic Model of the Ionosphere for Wide-Field Radio Experiments

Vadym Bidula

Department of Physics

McGill University, Montréal

April, 2023

A thesis submitted to McGill University in partial fulfillment of the requirements of the degree of

Master of Science

Abstract

The hydrogen 21-cm spectral line is a powerful probing tool for the Universe at cosmological scales. One particular application is studying the evolution of the early Universe, up to the era of the cosmic dawn - when the first stars were born. We can read the cosmic history of early star formation by comparing the measured global redshifted 21-cm signal against the backlight of the Cosmic Microwave Background (CMB) radiation spectrum. The CMB interacts with the neutral hydrogen on its way to the observer, tracking changes in global physical conditions during different stages of the Universe's timeline.

Because of cosmic expansion, the signal from the early Universe is redshifted to radio frequencies below 200 MHz. At these frequencies, the distorting effects of the Earth's ionosphere become significant and, if not treated correctly, could prevent instruments from detecting the signal. These effects generally depend on the observation frequency, time and geographical coordinates. Since 21-cm experiments are usually deployed to remote places to avoid radio interference, conducting experiments near the stations that run observations of ionospheric dynamics is not always possible. As a solution, one can use semi-empirical models of the ionosphere, which are based on observations but also use theoretical assumptions to estimate the ionosphere at different locations/times.

This thesis presents a developed model of ionospheric refraction, absorption and emission based on the widely adopted semi-empirical International Reference Ionosphere (IRI) model of ionosphere. The developed model was implemented in Python and made available for public access. I provide example simulations and discuss them in the context

of the MIST (Mapper of the IGM Spin Temperature) experiment. MIST has already conducted several observations, data from which is also provided in this work.

Abrégé

La raie spectrale de l'hydrogène à 21 cm est un outil puissant pour sonder l'Univers à l'échelle cosmologique. Une application particulière est l'étude de l'évolution de l'Univers primitif, jusqu'à l'ère de l'aube cosmique, lorsque les premières étoiles sont nées. Nous pouvons lire l'histoire cosmique de la formation des premières étoiles en comparant le signal global décalé vers le rouge mesuré à 21 cm avec le contre-jour du spectre de rayonnement du Fond Diffus Cosmologique (FDC). Le FDC interagit avec l'hydrogène neutre sur son chemin vers l'observateur, et suit les changements des conditions physiques globales à différentes étapes de la chronologie de l'Univers.

En raison de l'expansion cosmique, le signal de l'Univers primitif est décalé vers le rouge à des fréquences radio inférieures à 200 MHz. À ces fréquences, les effets de distorsion de l'ionosphère terrestre deviennent importants et, s'ils ne sont pas traités correctement, peuvent empêcher les instruments de détecter le signal. Ces effets dépendent généralement de la fréquence d'observation, de l'heure et des coordonnées géographiques. Étant donné que les expériences 21 cm sont généralement déployées dans des endroits éloignés pour éviter les interférences radio, il n'est pas toujours possible de réaliser des expériences à proximité des stations qui effectuent des observations de la dynamique ionosphérique. Comme solution, on peut utiliser des modèles semi-empiriques de l'ionosphère, qui sont basés sur des observations mais utilisent également des hypothèses théoriques pour estimer l'ionosphère à différents endroits/temps.

Cette thèse présente un modèle développé de réfraction, d'absorption et d'émission ionosphérique basé sur le modèle semi-empirique de l'ionosphère de référence internationale

(IRI) largement adopté. Le modèle développé a été implémenté en Python et mis à la disposition du public. Je fournis des exemples de simulations et les discute dans le contexte de l'expérience MIST (Mapper of the IGM Spin Temperature). MIST a déjà réalisé plusieurs observations, dont les données sont également fournies dans ce travail.

Acknowledgements

First and foremost, I would like to thank my supervisor, Prof. Jonathan Sievers, who provided me with invaluable advice and mentorship. Thanks to Jon, my Master's studies were an exciting and inspiring experience.

I am truly fortunate to have been a part of the MIST collaboration; I thank all team members for the useful feedback during weekly telecons. In particular, I am incredibly grateful to Dr. Raul Monsalve, who acted as my de facto co-advisor and provided me with insightful ideas and valuable criticism of my work. It was a pleasure working with Raul and Ian Hendricksen during the MIST expedition to Axel Heiberg Island, the observational data from which was used in this thesis. I thank the Polar Continental Shelf Program for logistical support that made the MIST deployment possible. I am also grateful to Dr. Laura Thompson, who shared her equipment and experience with us during the MIST deployment in the Arctic.

I thank Prof. H. Cynthia Chiang for her insightful ideas and helpful feedback. I would also like to thank all members of Jon and Cynthia's groups for their support and scientific discussions. I am also thankful to Dr. David Themens for his incredible patience in answering my endless questions about the models and physics of the ionosphere.

Finally, I would like to acknowledge the Canada 150 Research Chairs Program for providing funds that supported my Master's studies. I am also grateful to the McGill University Department of Physics for providing travel funds for my participation in the "Cosmology on Safari" conference.

Table of Contents

List of Figures

Acronyms

ΛCDM Lambda Cold Dark Matter.

A-CHAIM Assimilative Canadian High Arctic Ionospheric Model.

AHD angular horizon distance.

ARES Accelerated Reionization Era Simulations.

ASSASSIN All-Sky SignAl Short-Spacing INterferometer.

CDDIS Crustal Dynamics Data Information System.

CHAIN Canadian High Arctic Ionospheric Network.

CHAMP Challenging Minisatellite Payload.

CHIME Canadian Hydrogen Intensity Mapping Experiment.

CMB cosmic microwave background.

COSMIC Constellation Observing System for Meteorology, Ionosphere, and Climate.

COSPAR Committee on Space Research.

CSA Canadian Space Agency.

DCB differential code bias.

E-CHAIM Empirical Canadian High Arctic Ionospheric Model.

EDGES Experiment to Detect the Global EOR Signature.

EoR epoch of reionization.

ESF equatorial spread F.

FWHM full-width at half-maximum.

GAMBIT Global Assimilative Modeling of Bottomside Ionospheric Timelines.

GIRO Global Ionospheric Radio Observatory.

GNSS Global Navigation Satellite System.

GPS Global Positioning System.

GRACE Gravity Recovery and Climate Experiment.

HDF Hierarchical Data Format.

HEALPix Hierarchical Equal Area isoLatitude Pixelization.

HYPEREION HYdrogen Probe of the Epoch of REIONization.

IGRF International Geomagnetic Reference Field.

IRI International Reference Ionosphere.

IRTAM IRI-based Real-Time Assimilative Model.

ISIS International Satellites for Ionospheric Studies.

ISO International Standardization Organization.

ISR incoherent scatter radar.

JPL Jet Propulsion Laboratory.

LFSM Low Frequency Sky Model.

LOFAR Low-Frequency Aaray.

LST local sidereal time.

MARS McGill Arctic Research Station.

MCMC Markov chain Monte Carlo.

MIST Mapper of the IGM Spin Temperature.

PSD power spectral density.

R-CHAIM Reanalysis Canadian High Arctic Ionospheric Model.

REACH Radio Experiment for the Analysis of Cosmic Hydrogen.

RFI radio frequency interference.

RISR-N Resolute Bay Incoherent Scatter Radar - North.

SARAS Shaped Antenna measurement of the background RAdio Spectrum.

SITARA Short spacing Interferometer Telescope probing cosmic dAwn and epoch of ReionisAtion.

SSDC Solar System Data Centre.

SVD singular value decomposition.

TEC total electron content.

UKSSDC United Kingdom Solar System Data Center.

URSI International Union of Radio Science.

WMM World Magnetic Model.

Introduction

The 21cm transition line in hydrogen atoms is a powerful probing tool for the early history of the universe. The processes during the universe's evolution are expected to leave an imprint on a 21cm signal which, due to redshift, is observable in radio frequencies (below 200 MHz). However, this signal is extremely faint; it is many orders of magnitude lower than the galaxy synchrotron emission. Apart from that, there are many other observational difficulties, such as interference from the FM radio stations, whose broadcast range falls directly into the frequencies of interest.

Another challenge is the ionosphere, which inevitably corrupts the incoming from space radio waves. Studies show that the ionospheric influence alone can prevent the detection of the 21cm signal. Unfortunately, the ionosphere is complex, highly variable and hardly predictable, so the effect of the ionosphere is not easily removable. Given that global 21cm experiments are usually deployed far away from civilisation (to avoid data contamination), it is not always possible to get accurate measurements of the local ionosphere during the observation. Most simulations so far assumed a homogeneous and usually static ionosphere, which does not provide an in-depth insight into effects related to ionospheric variability.

The work presented here aims to make a step towards the dynamical model of the ionosphere in 21cm experiments simulations. I use climatological semi-empirical ionospheric electron density models to develop a Python module - `dionpy` - capable of simulating the ionospheric absorption, emission and refraction at any given location accounting for temporal and latitudinal variations of electron density. A significant focus was put on optimising and parallelising computations for the best efficiency.

My direct contributions in this thesis include:

- development and optimisation of wrappers for IRI and E-CHAIM (introduced in Ch. 3) ionosphere models in Python programming language;
- development of the dynamic model of ionospheric absorption and refraction based on created IRI and E-CHAIM models and implementation of the developed model in Python;
- organisation of developed wrappers and model in the form of Python packages and publishing them in open access;
- processing of raw observational data from the MIST experiment (introduced in Ch. 2), obtained in the expedition in which I directly participated, for the later comparison with ionospheric effects simulations;
- evaluation of the developed model in different applications, including:
  - comparison with the static homogeneous model;
  - comparison of integrated electron density with empirical total electron content maps;
  - simulation and exploration of instrument antenna temperature in the context of global 21cm cosmology experiments for specific date and location;
  - simulation of ionospheric effects for the recent deployment of the MIST experiment and comparison with the observed data.

This thesis is structured as follows. Chapter 1 reviews the physics behind the observed signal and theoretical predictions. The practical side of experiments - instrument design, considerations and particular implementation examples are discussed in Chapter 2. A quick overview of the ionosphere structure and an extensive description of electron density models are given in Chapter 3. Chapter 4 provides a detailed derivation of the ionospheric effects in global 21cm experiments, explains the development approach and discusses the model limitations. A few examples of applications of the developed model are shown and discussed in Chapter 5.

Chapter 1

Early Universe and the 21cm Line

One of the keys to understanding the universe's early history is the hydrogen 21cm spin transition. Its unique spectral signature allows studying the universe's infancy, going back to a time when the first stars and galaxies were just forming. A profound theory for the expected global signal is the first step towards successful observations. A significant progress has been made by cosmologists, which, apart from essential physics, includes modelling tools and various hypothetic scenarios of the universe's evolution, reflected in a 21cm signature.

This chapter makes a brief introduction to the theory behind 21cm cosmology experiments. It starts with a short review of the generally accepted theory of the universe's evolution, followed by an explanation of the physics of the 21cm transition in hydrogen atoms and how we can use it to probe the physical conditions in the early universe.

1.1 Chronology of the Universe

1.1.1 Big Bang, Inflation and Nucleosynthesis

The generally accepted theory states that the universe began with the Big Bang and continued to expand and cool to the state as we see it today. The Big Bang model has many solid observational evidences; the two key pieces are:

1. the expansion of the universe (discovered by Hubble (1929)) - proves the continuous expansion of space and also allows us to estimate the age of the universe;

2. the existence of the cosmic microwave background (CMB) (discovered by Penzias and Wilson (1965)); the CMB proves that the universe was indeed dense and hot long before.

The inflation of the universe is a rapid expansion that followed the Big Bang after $\sim 10^{-35}$ s (Dodelson and Schmidt, 2020). The concept of inflation was introduced to solve the "flatness" (why the curvature of the universe is close to zero?) and "horizon" (why the universe looks the same in every direction?) problems. In addition, the inflation explains why the universe looks homogeneous on a large scale (Peebles, 1993). During the inflation, the universe expanded quickly enough to prevent all the small inhomogeneities from annihilation and stretch the local thermal equilibrium so that the overall flatness and similar conditions are seen everywhere in the universe.

After the inflation, light elements formed in a process called Big Bang Nucleosynthesis as the universe cooled below nuclear binding energies. Still, the medium was hot enough to keep the formed nuclei and free electrons in thermal equilibrium with photons, rendering the universe non-transparent for light (Dodelson and Schmidt, 2020).

1.1.2 Cosmic Microwave Background

After approximately 400000 years from the Big Bang, due to the expansion, the universe became colder to the order of 3000 K. This drop in temperature reduced the ionization rate and allowed free electrons and protons to stay in the form of hydrogen atoms after spontaneous recombination. Consequently, the medium became transparent for thermal radiation, which we now call the CMB (Dodelson and Schmidt, 2020). The CMB has emission intensity spectrum B_ν in the form

$$B_\nu = \frac{2\nu^2}{c^2} \frac{h\nu}{\exp\left[h\nu/k_B T\right] - 1}, \tag{1.1}$$

where:

ν – observed frequency;

c – speed of light;

h – Plank constant;

k_B – Boltzmann constant;

T – absolute temperature of emitting body, in this case - the CMB.

The estimated temperature of CMB is $T_{CMB} = 2.725(z+1)$ K, where z is the redshift (Fixsen, 2009). Because Milky Way moves at approximately 600 km/s with respect to the CMB emission, the observed relict radiation has a dipole temperature surface distribution. However, after subtracting a dipole of amplitude around 3.355 ± 0.008 mK (Jarosik et al., 2011), the remaining CMB radiation map is highly isotropic with rms temperature variations less than ~ 80 μK on 1-degree scales and ~ 30 μK on larger scales (> 10 deg) (Planck Collaboration et al., 2020b). As will be shown later, backlight temperature variations are a few orders lower than the expected temperature changes of the global 21-cm signal, which makes the CMB a perfect reference point for observational cosmology.

1.1.3 Dark Ages, Cosmic Dawn and Reionization

Dark ages followed recombination. The universe became transparent, but the only light that filled the medium was the CMB emission. The clouds of hydrogen were still in the process of gravitational collapsing, which means no stars existed during that period. The CMB emission was in the visible range originally. However, due to expansion, it shifted into wavelengths not visible to human eyes (had there been humans), making the universe completely dark (Miralda-Escudé, 2003).

The formation of the first stars began the new era - cosmic dawn. The newly formed stars started processes that largely influenced the following evolution of the universe. In particular, ultraviolet and X-ray emissions from massive stars started ionizing the surroundings, creating regions of HII around them. The ionized gas became transparent, allowing the high-energy photons to travel further and ionize more gas. This lead to a period called epoch of reionization (EoR) when almost all gas in the universe was reionized, making the universe transparent to the starlight, as we see it today (Barkana and Loeb, 2001).

1.2 21cm Line as Cosmological Probe

1.2.1 Hydrogen Spin Transition

The hydrogen atom consists of a proton and an electron. In the ground state, these particles can exist in two configurations: with particle spins aligned parallel or antiparallel (hyperfine energy splitting). The latter state has slightly lower energy; the difference is $E_{10} = 5.874 \cdot 10^{-6}$ eV. The transition between two states is very rare - the lifetime of the exited state is approximately 10 million years (Furlanetto et al., 2006). At the same time, there is much hydrogen in the universe - around 75% (Planck Collaboration et al., 2020a), which makes the transition commonly seen in astronomical observations. During the transition, the extra energy is freed as an electromagnetic wave with a length equal to 21.106 cm. This emission line has a crucial importance for radio observations, including cosmology.

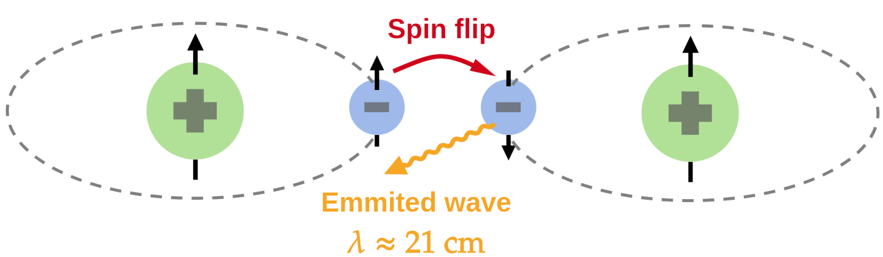

Figure 1.1: Illustration of hydrogen spin transition: a flip of electron spin results in a hydrogen atom in a lower energy state; the excess energy is freed as a 21cm photon.

The excitation temperature of the 21cm line is called the spin temperature (denoted as T_s), and is defined via the Boltzmann distribution in the form

$$\frac{n_1^H}{n_0^H} = \frac{g_1}{g_0} \exp\left[-T_*/T_s\right], \tag{1.2}$$

which describes the ratio of hydrogen number densities - n_1^H and n_0^H in excited and ground states respectively; $g_1/g_0 = 3$ is the ratio of statistical weights; $T_* \equiv E_{10}/k_B = 0.068K$ is the temperature equivalent to the energy of transition E_{10} (Furlanetto et al., 2006).

1.2.2 CMB as a Backlight

Photons, emitted by CMB, when redshifted to the frequency of hydrogen spin transition, can be absorbed and re-emitted in the clouds of hydrogen. If absorption and emission processes balance each other - there will be no visible track left. However, different processes (discussed in following sections) can lead to visible deviations from the background (CMB). In general case, the absorption and emission for the intensity I_ν in the gas along the path of propagation s is described by the radiative transfer equation:

$$\frac{dI_\nu}{ds} = -\alpha_\nu I_\nu + j_\nu, \tag{1.3}$$

where α_ν and j_ν are correspondingly absorption and emission coefficients (Rybicki and Lightman, 1986). It is convenient to write the solution of the radiative transfer equation in terms of optical depth τ, defined as $\tau_\nu(s_1, s_2) = \int_{s_1}^{s_2} \alpha_\nu(s')\, ds'$. The integrated Eq. 1.3 then becomes:

$$I_\nu(s) = I_\nu(s_0)e^{\tau_\nu(s_0,s)} + \int_{s_0}^{s} \frac{j_\nu(s')}{\alpha_\nu(s')} e^{\tau_\nu(s',s)}\, ds'. \tag{1.4}$$

Under the assumption of constant temperature in the absorber, the solution to Eq. 1.4 can be written as:

$$I_\nu^{\text{obs}} = I_R(\nu)e^{\tau_\nu} + I_s(1 - e^{\tau_\nu}), \tag{1.5}$$

with $\tau_\nu \equiv \tau_\nu(s_0, s)$, $I_s = j_\nu/\alpha_\nu$ and $I_R = I_\nu(s_0)$.

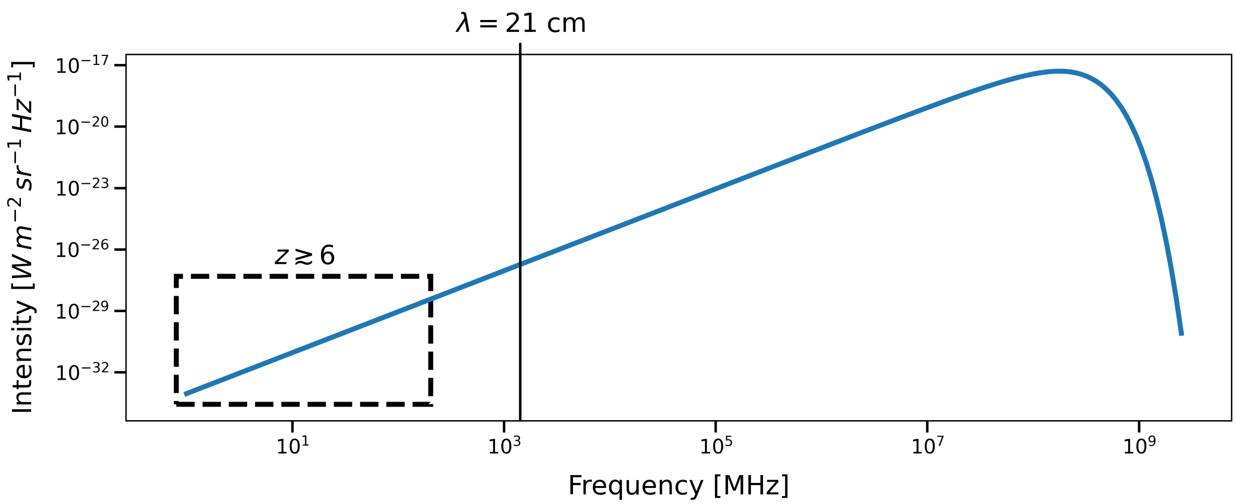

Figure 1.2: CMB black-body spectrum. The solid blue curve is Planck's radiation law evaluated at temperature $T = 2.725$ K. The dashed rectangle outlines frequencies participating in the 21cm processes in the early universe.

In the case of 21cm cosmology, this equation can be used to characterize the transfer of background radiation from CMB, through clouds of neutral hydrogen (Pritchard and Loeb, 2012).

Photons, travelling from the surface of the last scattering, shift in frequency until reaching the hydrogen spin transition frequency; only then can they contribute to the observed 21cm line. The model of the CMB intensity spectrum, as we see it from the Earth (black body with $T = 2.725$ K), is shown in Fig. 1.2. The dashed rectangle highlights the region of the spectrum that participates in processes related to the 21cm line ($z > 0$ for the 21cm line). As seen from the picture, the spectrum in that region follows exponential behaviour, and therefore the Rayleigh-Jeans approximation can be used:

$$I_\nu = 2k_B T \frac{\nu^2}{c^2}. \tag{1.6}$$

After applying assumption in Eq. 1.6 to Eq. 1.5, the latter becomes:

$$T_b = T_R(\nu)e^{\tau_\nu} + T_s(1 - e^{\tau_\nu}), \tag{1.7}$$

where T_b is the observed brightness temperature and T_R is the background temperature (in our case - the CMB temperature).

1.2.3 Practical Application

In practice, the quantity of interest is the differential brightness temperature δT_b, which is a difference of the observed brightness temperature T_b and the background temperature T_R, corrected for the redshift z:

$$\delta T_b = \frac{T_b(z) - T_R}{1+z}, \tag{1.8}$$

which takes a different form in the reference frame of hydrogen cloud:

$$\delta T_b = \frac{T_s - T_R(z)}{1+z}(1 - e^{\tau_\nu}). \tag{1.9}$$

Assuming that the optical depth of 21cm transition is small at all redshifts (Furlanetto et al., 2006), from Eq. 1.9 we get

$$\delta T_b = \frac{T_s - T_R(z)}{1+z}\tau_\nu \tag{1.10}$$

More explicit calculations within the ΛCDM cosmology in Eq. 1.10 result in

$$\delta T_b = 23 x_{HI}(1+\delta_b)(1+z)^{1/2}\left(\frac{\Omega_b h^2}{0.02}\right)\left(\frac{0.15}{\Omega_m h^2}\frac{1+z}{10}\right)^{1/2}\left(\frac{T_s - T_R}{T_s}\right) mK, \tag{1.11}$$

where x_{HI} is the fraction of neutral hydrogen; δ_b is the baryon overdensity; $h = H_0/(100\,\mathrm{km/s/Mpc})$ with H_0 being the Hubble parameter; Ω_b and Ω_m are the critical density parameters for baryons and matter, respectively. (Zaldarriaga et al., 2004).

1.2.4 Spin Temperature Components

Three competing processes determine the spin temperature in the clouds of neutral hydrogen:

1. absorption of background photons (and stimulated emission);

2. collisions with electrons, protons, and other hydrogen atoms;

3. resonant scattering of Lyα photons.

In the Rayleigh-Jeans approximation, T_s is given by

$$T_s^{-1} = \frac{T_\gamma^{-1} + x_\alpha T_\alpha^{-1} + x_c T_K^{-1}}{1 + x_\alpha + x_c}, \tag{1.12}$$

where T_γ is the temperature of the background; T_α is the effective colour temperature of Lyα radiation field evaluated at the Lyα frequency ($T_\alpha \equiv T_c(\nu_{\mathrm{Ly}\alpha})$); T_K is the kinetic temperature of the gas; x_α and x_c are coupling coefficients corresponding to atomic collisions and scattering of Lyα photons (Field, 1958). In the application of global 21cm cosmology experiments, T_γ corresponds to the CMB temperature.

Higher gas density during the dark ages led to more collisions between particles. Consequently, collisional excitation and de-excitation dominate during that era (a process known as "collisional coupling") (Furlanetto et al., 2006). The collisional coupling coefficient for a species i is defined as

$$x_c^i = \frac{n_i^H \kappa_{10}^i}{A_{10}} \frac{T_*}{T_\gamma}, \tag{1.13}$$

where κ_{10}^i is the coefficient of spin de-excitation rate in collisions with species i and A_{10} is the spontaneous decay rate of 21 cm transition (Field, 1958). The total x_c is then given by a sum of coupling coefficients for collisions with hydrogen atoms, electrons and protons:

$$x_c = x_c^{HH} + x_c^{eH} + x_c^{pH}. \tag{1.14}$$

The individual κ_{10}^i are functions of T_K and are calculated through quantum mechanics.

During the cosmic dawn, when the first stars form, the universe reaches another coupling that bonds spin temperature to the colour temperature T_c of Lyα radiation field, also known as the Wouthuysen-Field effect (Wouthuysen, 1952). The T_c is defined by:

$$\frac{h}{k_B T_c} = \frac{\mathrm{d}\log n_\nu}{\mathrm{d}\nu}, \tag{1.15}$$

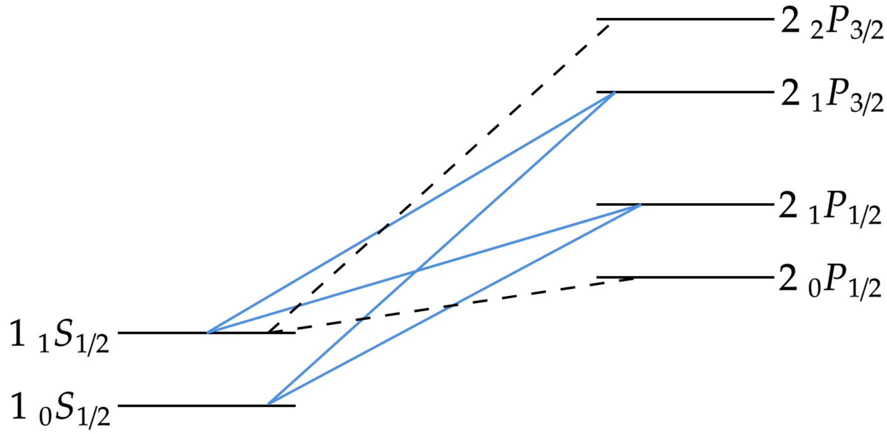

Figure 1.3: Lyα transition diagram. Energy levels labels correspond to $n\,_F L_J$ notation, where n, L and J are radial, orbital angular and total angular momentum quantum numbers; $F = I + J$ is the quantum number with I being the nuclear spin. Blue solid lines show transitions that may contribute to the spin flip in the hydrogen atom. Black dashed lines correspond to transitions that are also allowed but do not cause the spin flip. Reproduced from (Pritchard and Furlanetto, 2006).

where $n_\nu = c^2 J_\nu / 2\nu^2$ is the photon occupation number with J_ν being the mean intensity of the background radiation (Rybicki, 2006). The energy of the Lyman-alpha transition is 10.2 eV - much higher than the excitation energy of the 21cm line. Neutral hydrogen absorbs Lyα photons and then re-emits Lyα photons; consequently, the hydrogen atom may end up in one of the two spin states, as illustrated in Fig. 1.3. The physics of the process is complicated by the fact that the excited state of hydrogen can also be reached through the series of cascades from higher energy levels (Lyn transitions) that at some point reach the $2P$ energy level and end up producing a Lyα photon. Although direct scattering of Lyn photons other than Lyα can also cause the spin flip, it was shown that their contribution to the coupling effect is negligible (Pritchard and Furlanetto, 2006).

The coupling coefficient x_α can be expressed as

$$x_\alpha = S_\alpha \frac{J_\alpha}{J_\nu^c}. \tag{1.16}$$

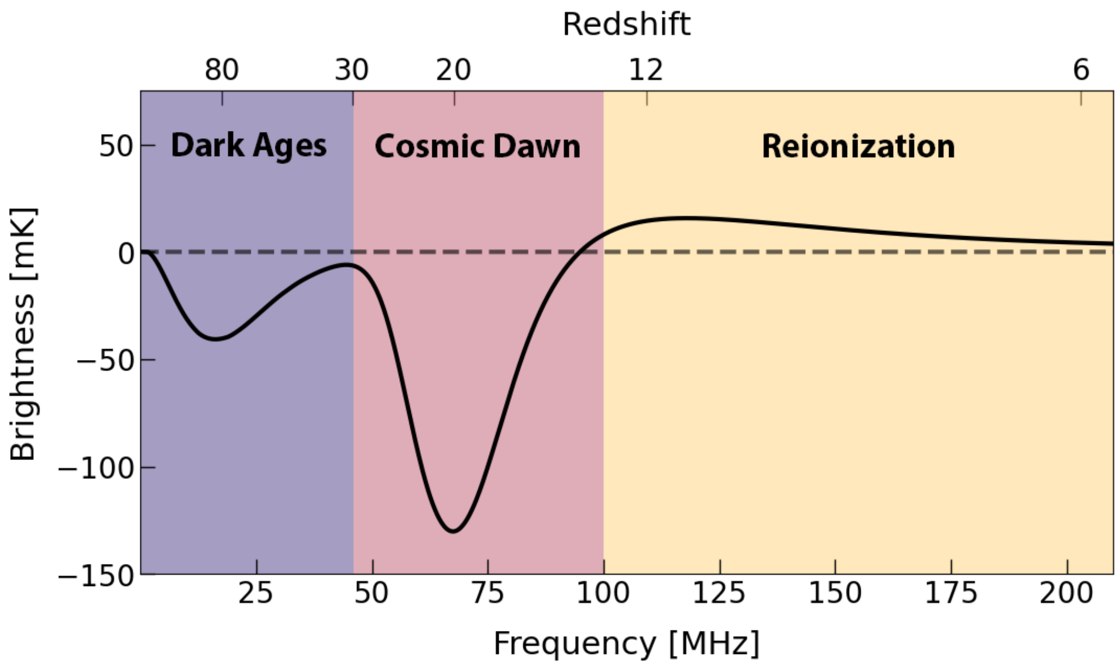

Figure 1.4: Standard prediction of δT_b during dark ages, cosmic dawn and EoR. The 21cm emission deficit during the dark ages ($z \gtrsim 30$) results from collision coupling of T_K and T_γ (Sec. 1.3.1) while the deficit during cosmic dawn ($30 \gtrsim z \gtrsim 15$) is caused by the Wouthuysen-Field effect (Sec. 1.3.2). The excess of 21cm emission during the EoR $15 \gtrsim z$ is a consequence of continuing X-ray heating. The simulated curve was calculated using the Accelerated Reionization Era Simulations (ARES) code with default cosmological and astrophysical parameters (Mirocha et al., 2012).

Here $S_\alpha \equiv \int \phi_\alpha(x) J_\nu(x)/J_\infty \,\mathrm{d}x$ with $\phi_\alpha(x)$ being the Lyα absorption profile; J_α is the J_ν evaluated at Lyα frequency and $J_\infty \,\mathrm{d}x$ is the flux far from the absorption feature; $J_\nu^c = 0.0767\big((1+z)/20\big)^{-2}$ is the number of Lyα photons per hydrogen atom (Furlanetto et al., 2006).

1.3 Standard Prediction for Global 21cm Signal

Fig. 1.4 illustrates the standard prediction for the global 21cm signal described in sections 1.3.1-1.3.3. The picture features the residual temperature δT_b versus frequency of observation; the latter also represents the age of the universe: the lower frequency is, the earlier universe we observe. The plot is split into three areas that represent dark ages ($z \gtrsim 30$) and cosmic dawn ($30 \gtrsim z \gtrsim 15$) absorption features, and EoR emission feature ($15 \gtrsim z$). This particular example was generated with the ARES[1] code. The code implements simulation of the radiative transfer, considering background radiation, galaxy luminosity functions, star formation, and other models (Mirocha et al., 2012; Mirocha, 2014; Mirocha et al., 2017, 2018). It is essential to mention that the plot provided in Fig. 1.4 is only one of the possible scenarios since many details about the universe's evolution are still unknown but hopefully will be explored with ongoing and upcoming cosmology experiments.

1.3.1 Emission Deficit: Dark Ages

As can be seen from Eq. 1.13, the coupling effect largely depends on the number density of electrons, protons and hydrogen atoms. Following the cosmic history from the beginning, during $z \gtrsim 200$, the Compton scattering from residual free electrons maintains thermal coupling of gas with the CMB, setting $T_K = T_\gamma$. Because of the high species number densities, hydrogen gas also experiences effective collisional coupling setting $T_s = T_\gamma$, which leads to $\delta T_b = 0$ and therefore no detectable 21cm signal (Pritchard and Loeb, 2012).

During $200 \gtrsim z \gtrsim 40$, gas cools adiabatically $T_K \propto (1+z)^2$, when the CMB temperature decreases as $T_\gamma \propto (1+z)$, which leads to $T_K < T_\gamma$. At the same time, the collisional coupling still holds, setting $T_s < T_\gamma$ and, consequently, $\delta T_b < 0$ (Loeb and Zaldarriaga, 2004; Hirata and Sigurdson, 2007).

From $z \sim 40$ to z_* (when the first luminous object appear), the universe's expansion leads to a number density drop. As the collisional coupling effect grows weaker, the thermal coupling of gas with the CMB returns the spin temperature to $T_s = T_\gamma$, making $\delta T_b \to 0$ (although it does not reach the zero point) (Pritchard and Loeb, 2012).

[1] https://github.com/mirochaj/ares

1.3.2 Emission Deficit: Cosmic Dawn

In the period of cosmic dawn $z_* \gtrsim z \gtrsim 15$, Lyα emission from the first stars couples with the cold gas through the Wouthuysen-Field effect. The required emissivity for the Lyα coupling is much less than the x-ray emissivity needed for heating T_K above T_γ, so fluctuations in Lyα flux and gas density dominate in the T_s. This leads to $T_s \sim T_K < T_\gamma$, which creates an absorption feature once again (Pritchard and Furlanetto, 2006; Chen and Miralda-Escudé, 2008).

When Lyα coupling saturates, it no longer affects fluctuations in T_b; simultaneously, the x-ray heating of gas becomes more significant. As more gas becomes hotter, more hydrogen is seen in emission, which again balances the absorption and sets $\delta T_b = 0$ (Pritchard and Loeb, 2012).

Fig. 1.5 shows the dependence of the global 21cm signal simulations on two competing processes: the Wouthuysen-Field effect (represented by Lyα intensity J_α) and the X-ray heating from newly formed stars (represented by heating rate ϵ_X). Bigger J_α leads to deeper through when stronger X-ray heating makes the through shallower. The timing of both processes also matters - it impacts the position of the peak on the frequency axis and, correspondingly, in the universe's history.

1.3.3 Emission Excess: Reionization

During the EoR ($15 \gtrsim z \gtrsim 6$), continuous heating by UV and x-ray photons becomes significant and drives $T_s \sim T_K >> T_\gamma$. Consequently, the T_s in Eq. 1.11 may be neglected (Santos and Cooray, 2006). The physics of EoR is complex and is commonly studied through numerical calculations, which compute the radiative transfer through the evolving density field based on ionizing source parameters (for reference, see Gnedin and Ostriker (1997), Razoumov et al. (2002), Zahn et al. (2007)). In short, the heating of the gas leads to excess emission in the δT_b spectrum, which increases with heating and decreases as most hydrogen becomes ionized.

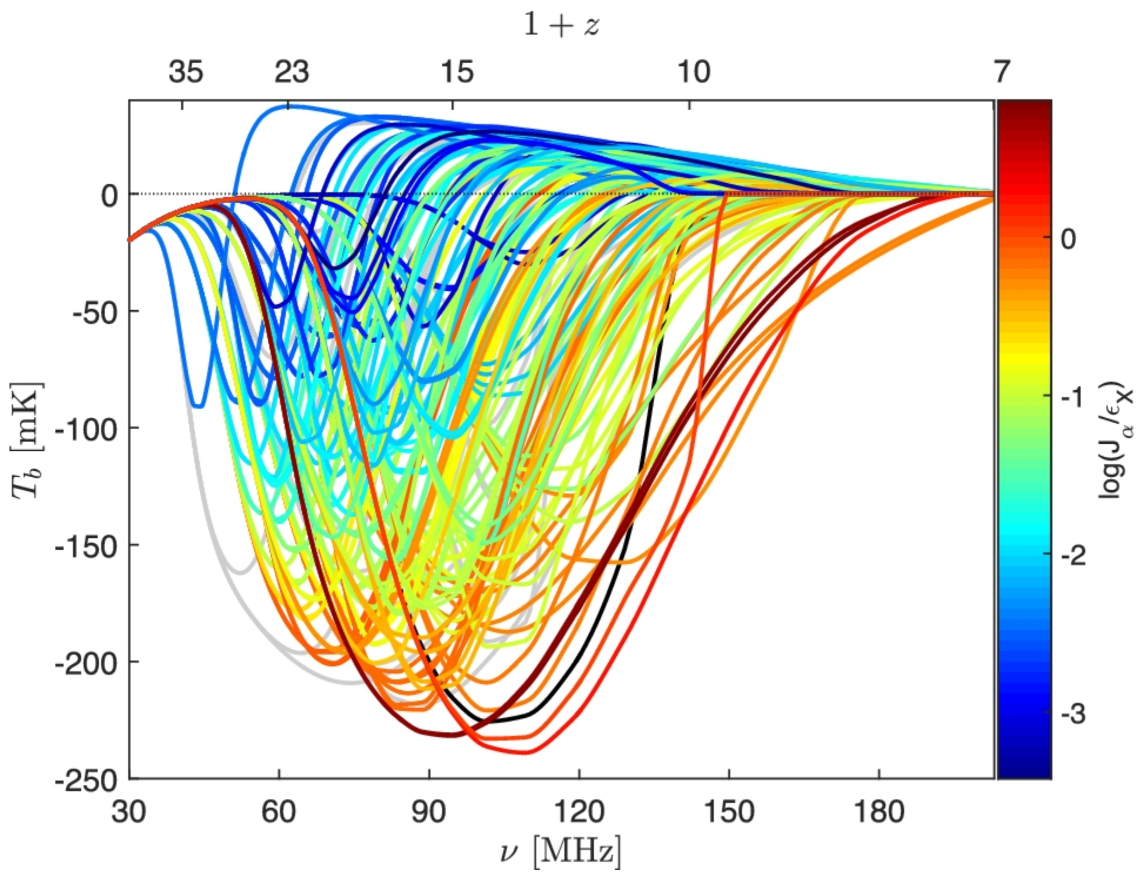

Figure 1.5: The 21cm global signal during cosmic dawn and EoR. The plot shows 129 astrophysical models simulated for different ratios of Lyα intensity J_α and X-ray heating rate ϵ_X, which are represented with different colour according to te colour bar on the right. Reused from (Cohen et al., 2017).

Chapter 2

Experiments to Detect the Global 21cm Signal

The global 21cm signal is expected to be extremely faint and difficult to detect. Various different approaches and implementations exist that try to find the signature of the 21cm signal. They can be grouped into two categories: radio-interferometric arrays and single wide-beam instruments. This chapter is focused on the latter. Here I briefly discuss the general idea behind global 21cm experiments, instrument design and recent advancements in this field.

2.1 General Approach

Although some particular implementation considerations may differ, in general, most global 21cm experiments follow the same design: a single antenna with a wide beam that records the integrated temperature from the whole sky. The observed temperature T_A is modelled as a convolution of the sky brightness temperature T_{sky} with the antenna beam B:

$$T_A(t,\nu) = \frac{\displaystyle\int_0^{2\pi}\int_0^{\pi/2} B(\theta,\phi,\nu)\, T_{sky}(\theta,\phi,t,\nu)\,\mathrm{d}\theta\,\mathrm{d}\phi}{\displaystyle\int_0^{2\pi}\int_0^{\pi/2} B(\theta,\phi,\nu)\,\mathrm{d}\theta\,\mathrm{d}\phi}, \tag{2.1}$$

where θ, ϕ are zenith angle and azimuth in the field of view of the instrument, and t is the time of the observation (Monsalve et al., 2021).

Apart from the 21cm of interest, sky temperature includes strong radio emissions from galactic and extragalactic synchrotron radiation. This emission (also called foreground emission) is many orders of magnitude higher than the 21cm signal; therefore, it must be carefully removed (Huang et al., 2018; Liu and Shaw, 2020). The effects of the ionosphere are included in T_{sky}.

The beam B is a characteristic of an instrument and depends mainly on instrument design. However, signal reflections from the surface underneath the instruments can impact the shape of the beam pattern. If the instrument stands on the soil, and soil characteristics (such as conductivity and permittivity) evolve in time, the resulting beam will also change with time. One possible solution could be placing a ground plane (a huge conductive sheet) under the instrument. Assuming the infinite size of the ground plane, one can derive a static antenna beam model based on the properties of the ground plane used. However, the reflections from areas outside the ground plane will still impact the beam, which must be appropriately addressed in the data analysis. Another possible solution would be to monitor soil properties during observations and reconstruct the beam with simulations later.

During the observations, the instrument periodically switches between the antenna and calibration sources, which are later used for converting recorded power spectral densities (PSD) to antenna temperature (initial calibration) (Monsalve et al., 2017; Patra et al., 2013). Then the spectra is usually brought to an absolute noise temperature scale using the lab measurements at a fixed reference frame (Rogers and Bowman, 2012). At this point, other corrections could be applied, such as accounting for antenna and receiver losses, radio frequency interference (RFI), beam chromaticity, soil/ground plane effects, or ionospheric corruption.

After these corrections are applied, the remaining signal is described by Eq. 2.1. To find the faint 21cm signal, the dominating foreground emission must be removed by fitting the theoretical model to the spectrum. Different foreground parameterizations exist; in this work, we use the `LINLOG` model (polynomials in the logarithm scale):

$$T_{model}(\nu, t) = \left(\frac{\nu}{\nu_0}\right)^{-\beta} \sum_{m=0}^{M-1} a_{m,t} \cdot \left[\ln\left(\frac{\nu}{\nu_0}\right)\right]^m, \tag{2.2}$$

where T_{model} is the model of foreground to be subtracted; ν_0 is a centre frequency for the observed band; $a_{m,t}$ are the fitted coefficients with m representing the power of each term in the linear expansion and t representing change in time (in this case - local sidereal time (LST)); β is the assumed spectral index of the foreground emission.

In simulations of global 21cm experiments, the `LINLOG` is usually used up to the seventh order. The spectral index β must not necessarily be assumed from physical consideration; the β can also be included as a free parameter in the non-linear fitting procedure. However, the beam chromaticity would severely affect the β as a free parameter, which will complicate the physical interpretation of the fitting results (Monsalve, 2023). In this work's later analysis of ionospheric effects, the assumption $\beta = -2.505$ is used (Mozdzen et al., 2017, 2019; Spinelli et al., 2021). The uncertainty in the assumed spectral is expected to have a negligible impact on the fitting residuals (Monsalve, 2023).

The model of the global 21cm signal is fitted to the data simultaneously with the foreground - to avoid accidental signal removal with polynomials. Direct simulations of the 21cm signal in the vast astrophysical parameter space are time-consuming, which, for some models, can make it impractical to employ them in the fitting process. One solution is to use a simplified empirical model, for instance, a flattened gaussian. This model does not reflect the underlying physics of the 21cm signal but is good enough to find and characterize the absorption profile (Bowman et al., 2018). Another approach consists of using emulators of 21cm global signal - for example - machine learning models trained on accurate simulations. For such an approach, a number of implementations already exist, including `globalemu` (Bevins et al., 2021), `21cmGEM` (Cohen et al., 2020), `21cmVAE` (Bye et al., 2022).

2.2 Existing Implementations

2.2.1 EDGES

Experiment to Detect the Global EOR Signature (EDGES)[1] was the pioneer in the field and the first experiment to report evidence for the detection of a flattened absorption profile around ~ 78 MHz (Bowman et al., 2018). The two low-band (50-100 MHz) instruments were deployed at the Murchison Radio-astronomy Observatory in Western Australia. For the result in (Bowman et al., 2018), the instruments collected data for nearly two years. As described in the Sec. 2.1, the EDGES data were calibrated, filtered and integrated within LST blocks. A five-term polynomial foreground model (similar to Eq. 2.2 but with modifications that consider underlying physics) was first fitted to the data to discard outlying LST data blocks (Rogers et al., 2015). Then it was fitted again to the final integrated spectra, together together with the 21cm global signal model T_{21} in the form of a flattened gaussian:

$$T_{21}(\nu) = -T_0 \left(\frac{1 - e^{-\tau_f e^{\varkappa}}}{1 - e^{-\tau_f}} \right), \tag{2.3}$$

where

$$\varkappa = \frac{4(\nu - \nu_{ctr})^2}{\Delta\nu_{hm}^2} \log\left[\frac{1}{\tau_f} \log\left(\frac{1 + e^{-\tau_f}}{2}\right)\right], \tag{2.4}$$

T_0 is the absorption amplitude, ν_{ctr} is the centre frequency of the model, $\Delta\nu_{hm}$ is the full-width at half-maximum (FWHM), and τ_f is the flattening factor. The reported best-fit parameters are: $A = 0.5^{+0.5}_{-0.2}$ K, $\nu_{ctr} = 78 \pm 1$ MHz, $w = 19^{+4}_{-2}$ MHz and $\tau_f = 7^{+5}_{-3}$, where the error corresponds to 99% confidence. Replace with: Fig. 2.1 is reused from (Bowman et al., 2018) and shows the absorption feature extracted from several EDGES data sets.

The observed absorption profile caused high interest and active discussions not only from being the first reported detection but also because of its unexpected characteristics. In particular, the absorption feature amplitude of ~ 0.5 K is almost twice the maximum

[1] https://www.haystack.mit.edu/astronomy/astronomy-projects/edges-experiment-to-detect-the-global-eor-signature/

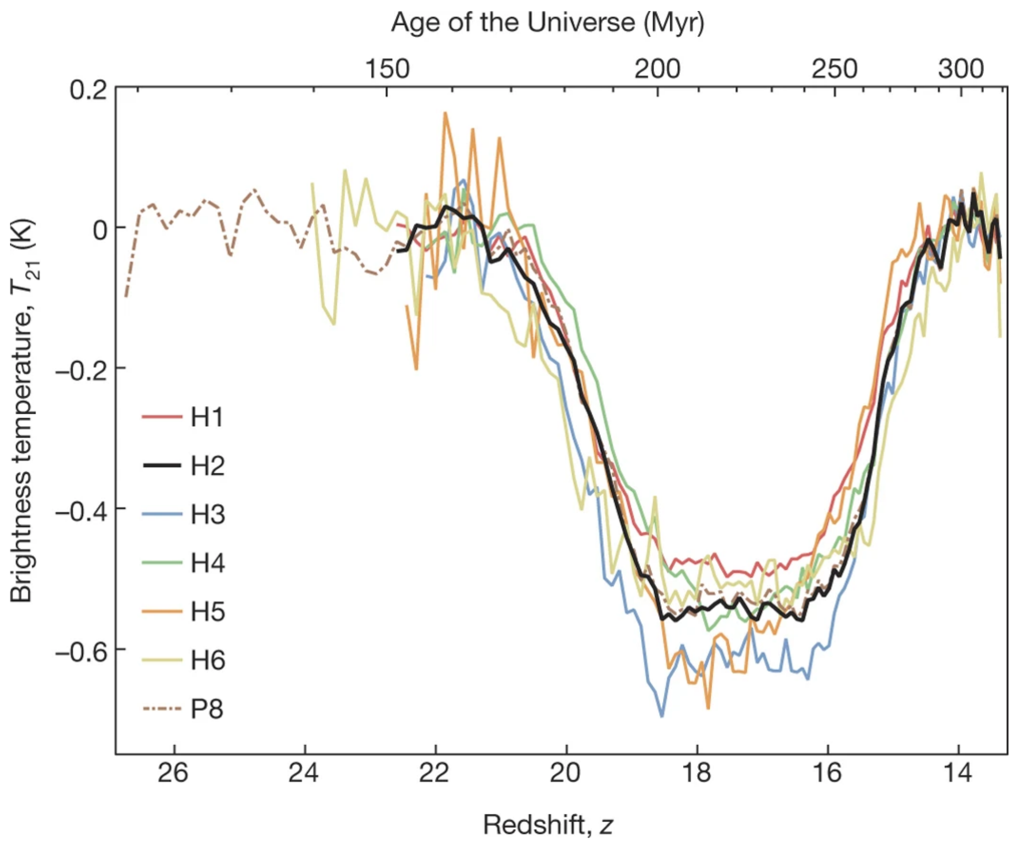

Figure 2.1: Reported cosmic dawn absorption profile by EDGES. Solid lines of different colours represent model fits plus residuals for different hardware and analysis configurations; all H-models were processed using data from the $60 - 99$ MHz band and a four-term polynomial foreground model. The thick black line is the best fit with the highest signal-to-noise ratio ($SNR = 52$). The dash-dotted line (P8) uses the same data as the H2 model but a different foreground model and the full frequency band. Reused from (Bowman et al., 2018) with permission, Copyright © 2018, Macmillan Publishers Limited.

depth predicted by the standard scenarios based on ΛCDM cosmology (Liu and Shaw, 2020). One possible explanation of the very large amplitude suggests existing of an undetected population of high-redshift radio sources that boost the background radiation, increasing the contrast between background temperature T_γ and spin temperature T_s (Feng and Holder, 2018; Fialkov and Barkana, 2019). Another explanation assumes previously undetected interaction between baryons and dark matter particles (Barkana, 2018; Berlin et al., 2018; Muñoz and Loeb, 2018). At the same time, the debates about possible systematics in the EDGES data continue. For example, Bradley et al. (2019) argue that the found absorption profile could result from resonances in the ground plane. Other authors express concerns about the data analysis methods (Hills et al., 2018; Singh and Subrahmanyan, 2019)

In summary, the EDGES result is still to be confirmed by other ongoing and planned experiments. Currently, EDGES continues observations and was recently deployed to Devon Island in Nunavut, Canada.

2.2.2 SARAS and Other Global Experiments

The Shaped Antenna measurement of the background RAdio Spectrum (SARAS) is an independent experiment with a purpose similar to EDGES. The main difference in design is a cone-shaped antenna mounted above the reflector disk; the whole instrument is deployed on the surface of a lake (Raghunathan et al., 2021). The SARAS 3 implementation claimed non-detection of the EDGES best-fit profile in their data with 95.3% confidence (Singh et al., 2022).

The data frequency band used in SARAS 3 analysis was 55-85 MHz, as illustrated in Fig. 2.2 and did not cover the EDGES reported profile fully. The presence of the EDGES profile was tested applying an Markov chain Monte Carlo (MCMC) fitting procedure to the model in the form

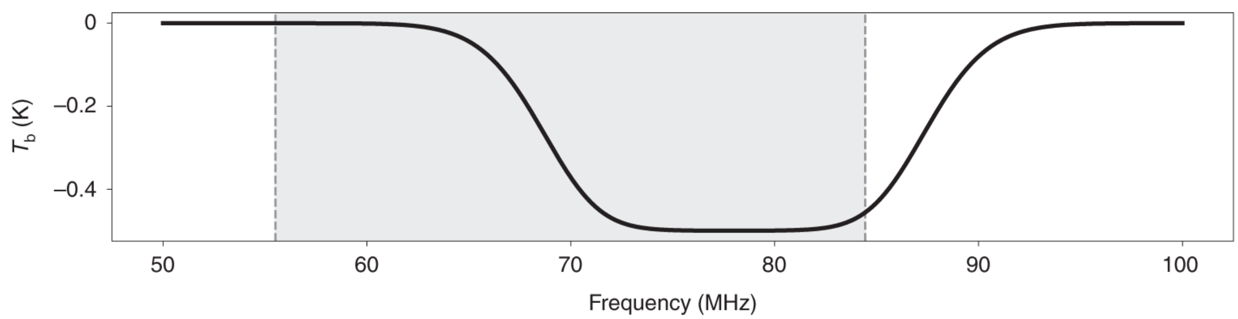

Figure 2.2: The best-fit profile reported by Bowman et al. (2018). The shaded region represents the frequency range used in SARAS-3 data analysis (55-85 MHz); frequencies outside the specified were cut off because of excessive . Reused from (Singh et al., 2022) with permission, Copyright © 2022, The Author(s), under exclusive license to Springer Nature Limited.

$$\log_{10}\left(\frac{T(\nu)}{1\,K} - s\frac{T_{EDGES}(\nu)}{1\,K}\right) = \sum_{i=0}^{6} a_i \mathfrak{R}\left[\log_{10}\left(\frac{\nu}{1\,\mathrm{MHz}}\right)\right]^i, \tag{2.5}$$

where $\mathfrak{R}$ operator linearly rescales values into range $[-1, +1]$. The one dimensional probability distribution for the s parameter is shown in Fig. 2.3 (the s notation used here is not related to the path length defined in previous chapter and is used only in context of the SARAS result). The obtained best fit value os s is close to zero with 1σ interval of ± 0.6. Although the SARAS data shows no evidence for the EDGES profile, the existence of the profile still cannot be ruled out with high significance.

In light of these two conflicting results, other independent experiments are either collecting data or being constructed, including:

- Radio Experiment for the Analysis of Cosmic Hydrogen (REACH) (de Lera Acedo, 2019)
- All-Sky SignAl Short-Spacing INterferometer (ASSASSIN) (McKinley et al., 2020),
- Short spacing Interferometer Telescope probing cosmic dAwn and epoch of ReionisAtion (SITARA) (Thekkeppattu et al., 2022),

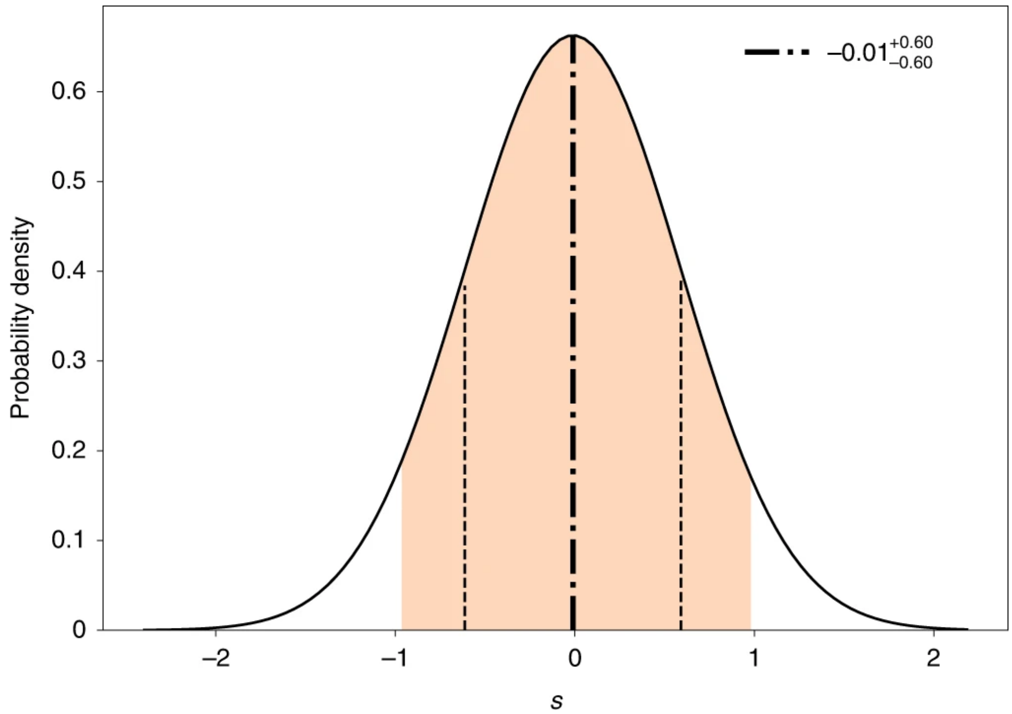

Figure 2.3: One dimensional distribution of the s parameter fitted during analysis of SARAS-3 data. The s parameter is the multiplier of the EDGES reported profile in the fitted model described by Eq. 2.5. Dashed black lines outline 1σ confidence interval. Reused from (Singh et al., 2022) with permission, Copyright © 2022, The Author(s), under exclusive license to Springer Nature Limited.

and others. There are also plans to deploy an instrument to the far side of the Moon in order to avoid RFI contamination and ionospheric influence. (Bale et al., 2023).

2.3 The MIST Experiment

The Mapper of the IGM Spin Temperature (MIST)[2] is another experiment to detect the global redshifted 21cm signal with high precision. I have been the member of the MIST collaboration since September 2021. The work presented in this thesis is first and foremost to support MIST analysis.

[2] `http://www.physics.mcgill.ca/mist/`

The MIST instruments are wide-beam single-antenna (blade dipole) measuring the sky in the frequency range of $25 - 105$ MHz, focusing on finding cosmic dawn and dark ages signature. The standard design of MIST does not include a ground plane. Two battery-powered instruments have been built so far with a focus on portability and high calibration accuracy; MIST's portability enables its deployment at different remote locations to:

- minimize the RFI;
- access sites with different soil properties to better to separate the 21-cm signal from other spectral contributions.

The full description of the MIST instruments will be provided in (Monsalve et al., 2023) (in preparation).

MIST has already conducted several field measurements. A preliminary test run was performed in August 2021 at Uapishka station ($51.4712°$ N, $68.2358°$ W) in Quebec, Canada. In May 2022 the instruments were deployed to Deep Springs Valley in California ($37.34583°$ N, $118.02555°$ W) and to Death Valley in Nevada ($37.21333°$ N, $117.09111°$ W). In July 2022, MIST conducted deployment to the McGill Arctic Research Station (MARS) located on the Axel Heiberg island, in which I participated directly; Fig. 2.4 shows the process of installation of the instrument at MARS. MARS ($79.37980°$ N, $90.99885°$ W) is located away from cities and provides a very radio-quiet environment, previously discovered in 2019 exploratory campaign (Dyson et al., 2021). Fig. 2.5 summarizes the list of deployment sites in 2021-2022. Some preliminary MIST data examples and exploratory analysis will be provided in Sec. 5.5. Very recently, in April-May 2023, MIST was once again deployed to MARS.

The analysis of the ionospheric effects in this work is performed in the context of the MIST experiment. For most ionospheric simulations, instrument location is usually chosen between MARS and Death Valley coordinates. The starting dates chosen for

Figure 2.4: MIST installation process at Axel Heiberg island in July 2022. The blue plastic wrap was used to protect the instrument from bad weather conditions.

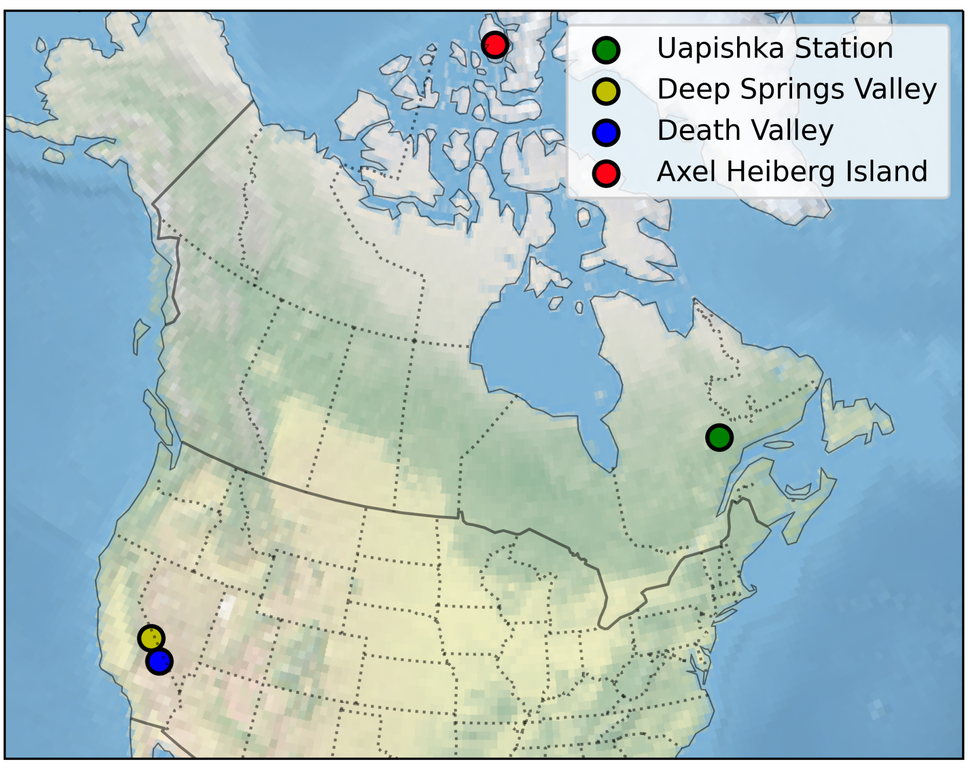

Figure 2.5: MIST deployment locations in 2021-2022.

simulations are 15 July 2022 or 7 May 2022, corresponding to the first day of observations during the deployments.

Chapter 3

Ionosphere: an Overview and Models

The ionosphere is a layer in the Earth's atmosphere ionized by solar radiation and (much less) by solar wind. Although only a tiny fraction of neutral gas is ionized, the ionosphere plays an essential role in the propagation of electromagnetic waves, such as absorption and refraction, especially below 300 MHz. This chapter briefly overviews ionospheric structure, followed by an extensive description of semi-empirical ionospheric models used in simulations of electron density, electron temperature and frequency of electron collisions in the ionosphere.

3.1 Structure and Behaviour of the Ionosphere

3.1.1 Regions of Ionization

Three layers of ionisation can be distinguished in the Earth's ionosphere. These layers differ in ionisation sources, chemical content and, most importantly, their influence on propagating radio waves. The ionosphere starts with the D-layer, which extends from ~ 60 km to ~ 90 km, followed by the E-layer (~ 90 km to ~ 150 km) and the F-layer (~ 150 km to ~ 500 km). Fig. 3.1 illustrates the vertical extent of ionospheric layers.

The first historically discovered ionospheric layer was the E-layer (also called the Kennelly–Heaviside layer) (Appleton and Barnett, 1925). Occasionally, the localized clouds

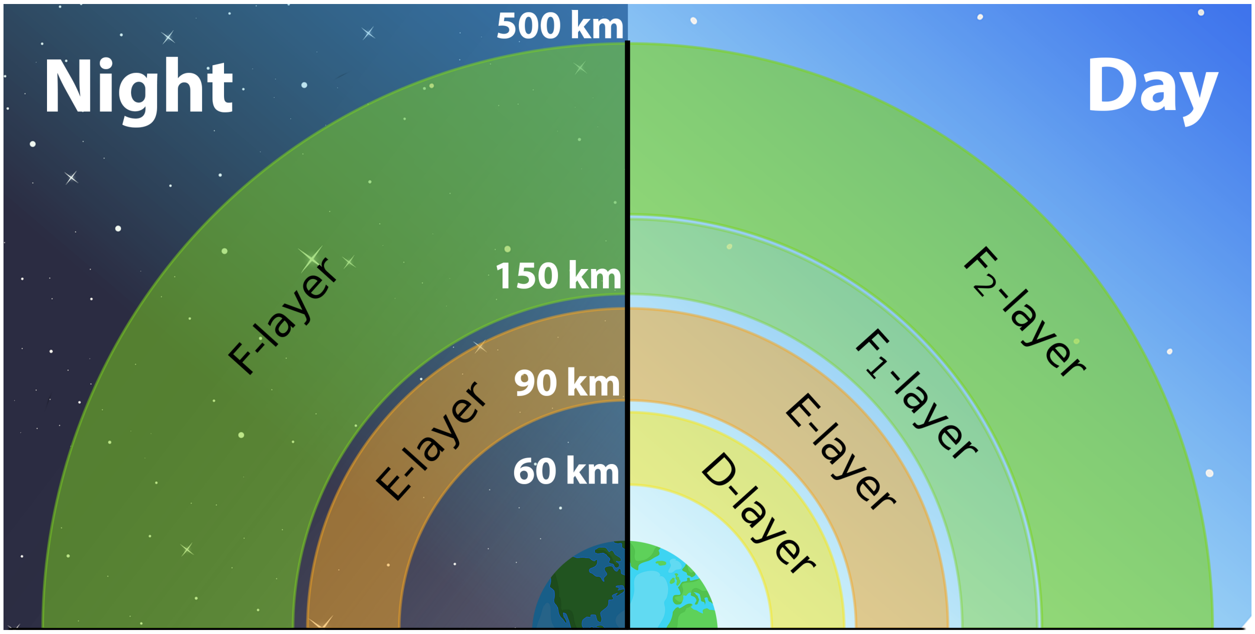

Figure 3.1: Illustration of ionization regions in the Earth's ionosphere. The D-layer ($\sim 60-90$ km) exists only during the daytime and disappears at night, but some residual ionization remains. The F-layer ($\sim 150-500$ km) has the highest concentration of free electrons that peaks at ~ 250 km; during the day, another - smaller peak appears in the lower part of the F-layer, which is nominally separated as an F_1-layer, while the remaining part is named an F_2-layer. The E-layer, at altitudes of $\sim 90-150$ km, is between the F and D layers.

of plasma emerge into sub-layer called sporadic E-layer, or E_s-layer. It mostly appears during the day time with seasonal variation. The typical estimated electron density in E_s layer is $\sim 10^{11}$ m^{-3}. The distinctive feature of the E_s-layer is that it can reflect waves up to 100 MHz, making intercontinental radio communications possible (Davies, 1990).

The next discovered ionization region was the F-layer, also called the Appleton–Barnett layer (Appleton and Naismith, 1932). The F-layer has the highest concentration of free electrons in the atmosphere - up to $\sim 10^{13}$m^{-3}, which corresponds to a plasma frequency $\nu_p \sim 30$ MHz (all radio waves with frequency $\nu < \nu_p$ cannot propagate in plasma - this is also known as a low-frequency cut-off). A typical peak electron density of the F-layer (denoted as $N_m F_2$) is $\sim 10^{12}$m^{-3}, corresponding to $\nu_p \sim 10$ MHz. The lower part of the F-layer with the peak electron density $\sim 10^{11}$m^{-3}) at heights 150-220 km exists only during the day and is called the F_1-layer, while the upper part, F_2-layer, exists during both day and night (Evans and Hagfors, 1968).

The D-layer is the lowest ionized ionospheric layer. The peak electron density in the D region reaches up to $\sim 10^{10}$ m^{-3}, which corresponds to $\nu_p \sim 0.9$ MHz (Friedrich and Torkar, 1992). Because of relatively low electron content, this layer's contribution to the ionospheric refraction is negligible. On the other hand, passing EM wave causes electrons to move, which then collide with neutral particles and make the wave lose energy (in other words - the energy is absorbed). Higher electron densities persist in the D-layer only during the daytime, resulting in higher attenuation effects. During the night, due to the lack of ionizing radiation, the electron density decreases to $\sim 10^8$ m^{-3} (Friedrich and Torkar, 1992), which, however, still contributes to the absorption. The typical absorption estimations for waves at 100 MHz are ~ 0.05 dB during the daytime and ~ 0.005 dB during the nighttime (Thompson et al., 2017).

3.1.2 Latitudinal Variations

The ionosphere can be divided into three regions according to their geomagnetic latitude. The first and best understood one is the mid-latitude region (approximately from 30° to 60° on either side of the magnetic equator). The ionization in this region is mainly caused by solar UV and X-ray emissions, and the ion movements are controlled by winds in neutral air. The mid-latitude processes in the ionosphere also exist at other latitudes; however, at low and high latitudes, other processes become critical (Hunsucker and Hargreaves, 2007).

Magnetic fields strongly influence the low-latitude zone (0° to ~25°); the Earth's magnetic field flows almost horizontally over the magnetic equator (Lühr et al., 2021), producing anomalies and irregularities (Fejer and Maute, 2021; Abdu, 2020). The magnetic field interacts with the electric field, creating the $\vec{E} \times \vec{B}$ drift that pushes electrons upwards at the equator. The electrons then move downwards and away from the equator, which, in turn, forms ion density enhancements to the north and south of the equator. The described process is also called a ”fountain effect”. The fountain effect can be noticed in visualizations of ionosphere simulations performed in later chapters, specifically in Fig. 5.7. The equatorial spread F (ESF) effect (which unites many small-scale irregularities) is another anomaly in the equatorial F-layer, which usually happens after sunset. The rapid changes in the vertical transport of plasma, caused by the Rayleigh–Taylor instability, result in the creation of bubbles of lower electron density. These bubbles disrupt the traversing radio waves, causing the ”scintillation” effect (Li et al., 2021).

At high latitudes, the situation is the opposite. The magnetic field is almost vertical, making the ionosphere much more complex in that region. The high-latitude ionosphere is more accessible for the solar particles, which makes it behave in a pattern controlled by the variable solar wind. An example of this is the auroral zones that occur at about 60°-80° N/S magnetic latitude. Auroral zones are caused by the connection of the Earth's internal magnetic field with the interplanetary magnetic field, which makes energetic electrons able to precipitate deep into the atmosphere. In the polar cap region, the density irregularities ($> 80°$) are observed and described as polar patches (”islands” of dense plasma in the F-layer) (Watson et al., 2011) and auroral arcs. Another complication is occasional transfers of plasma from mid-latitudes in the form of a tongue of ionization or patches (Foster et al., 2005).

The semi-empirical models presented in the following sections try to account for the anomalies listed in this section with variable success. While the irregularities in the equatorial region can be modelled with the complex physics theory, the ionosphere at high latitudes is very sensitive to sporadic solar events, making it highly dynamic and unpredictable; the small amount of observational stations at high latitudes makes the modelling even more difficult.

3.2 IRI

International Reference Ionosphere (IRI)[1] is the semi-empirical model of the Earth ionosphere in the 60-2000 km altitude range. It represents monthly averages of ionospheric electron density, electron temperature, ion temperature and ion composition. The IRI considers diurnal, seasonal and geographical ionospheric variations. The data used in the development of the IRI model, among others, includes hundreds of ground- and space-based instruments, such as:

- ionosondes - instruments that transmit radio waves to the ionosphere and measure the return time of reflected waves;
- incoherent scatter radars (ISRs), which study the incoherent scatter of transmitted radio beam off the free electrons in the ionosphere. The scattered beam contains information about electron density, electron and ion temperatures, ion composition and other;
- sounding rockets, which continuously measure currents at different altitudes as they move through the ionosphere;
- satellites, which include:
  1. Constellation Observing System for Meteorology, Ionosphere, and Climate (COSMIC);
  2. Alouette-1 and Alouette-2;
  3. International Satellites for Ionospheric Studies (ISIS) -1 and -2;
  4. Intercosmos 19.

  The first three mentioned satellites performed topside sounder measurements, which were used for recovering the topside electron density profile. The COSMIC satellite was mainly used for global modelling of h_mF_2 (Shubin, 2015).

[1] https://irimodel.org/

- Global Navigation Satellite System (GNSS) stations, allowing to estimate the ionospheric total electron content (TEC) by measuring the phase delay in the signal emitted by GNSS satellites.

The IRI project was initiated by Committee on Space Research (COSPAR) and International Union of Radio Science (URSI) in 1968 with aim to develop and support an international standard for most needed physical parameters of the ionosphere (Rawer et al., 1978). Since then, the model was actively improved and published several model versions; the latest available model is IRI-2020 (Bilitza et al., 2022). In April 2014, the IRI became the International Standardization Organization (ISO) standard for the ionosphere (ISO-16457:2022, 2022).

3.2.1 Model Structure

The ionospheric electron density profile within IRI is divided into topside and bottomside models with separation line located at the height of the peak electron density in the F_2-layer (denoted as h_mF_2). The topside profiled is based on satellites measurements, while bottomside profile is constructed from ground-based (for instance, ISRs or ionosondes) and rocket measurements. Both profiles are normalized to the F2-peak electron density N_mF_2 to result in a continuous profile. The example electron density profile and corresponding N_mF_2 separation line are shown in the left part of Fig. 3.2.

While representation of the topside ionosphere involves a single model (for instance, IRI-2001 (Rawer et al., 1978) or NeQuick topside (Nava et al., 2008)), the bottomside profile is more complicated and requires several models - one for each distinct region of the lower ionosphere. This includes models for (from top to bottom) the F2 bottomside region, the F1 region, the intermediate region (provides a smooth transition between the F1 and E regions), the E region (consists of E-valley on top, E-peak and E bottomside region) and the D region (Bilitza et al., 2022). All distinctive features of bottomside regions can be noticed on the right picture in Fig. 3.2.

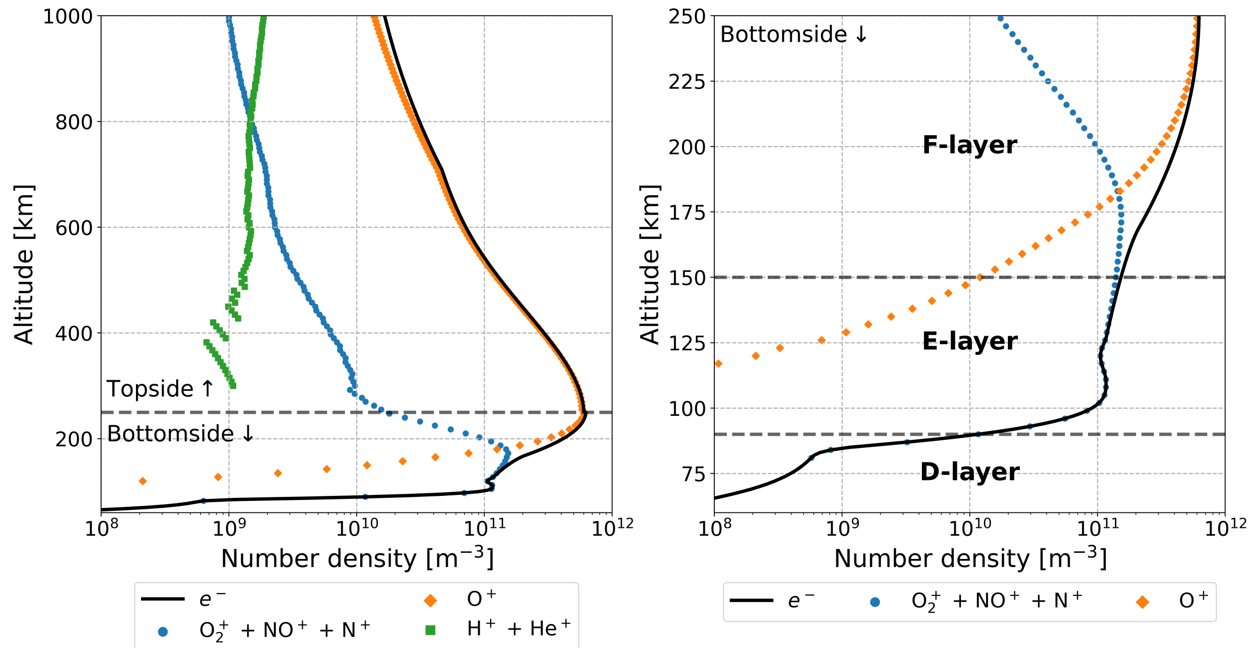

Figure 3.2: The example of the altitude profile of electron density (black solid curve) and the contributing ions (shaped coloured markers, see the plot legend). The left panel illustrates model separation for topside and bottomside ionospheric profiles. The right panel shows the zoomed-in bottomside ionosphere. The profiles were generated with IRI-2020.

3.2.2 IRI Drivers

The instrumental data collected from past ionosphere observations provided a base for creating IRI models for different ionospheric regions. However, the ionosphere is dynamic and cannot be accurately predicted using only past measurements. As a solution, the IRI uses external drivers, namely - solar, magnetic and ionospheric indices, which represent the change of ionosphere over time.

One of the solar indices used in IRI is the R_{12} - the 12-month moving average of monthly values of sunspot number. In particular, the R_{12} is used in calculation of h_mF_2 (Altadill et al., 2013), F-layer bottomside electron density (Altadill et al., 2009), D-layer electron density (Rawer et al., 1981) and others.

The second index used is $F10.7$ - the solar radio flux af wavelength 10.7 cm. Besides the daily $F10.7_d$, the IRI uses $F10.7_{81}$ and $F10.7_{365}$ - the 81-day and 365-day moving averages of $F10.7$, and also their combinations, such as $PF10.7 = (F10.7_d - F10.7_{81})/2$. The $F10.7$ and its derivatives are involved in calculation, for example, of topside electron temperature (Truhlik et al., 2012) and ion composition (Truhlik et al., 2015; Richards et al., 2010), equatorial ion drift (Fejer et al., 2008), D-region electron density (Friedrich et al., 2018), and solar dependence of h_mF_2 (height of F_2-layer electron density peak) (Shubin, 2015). Solar indices in the IRI are updated twice a year. The model also allows one to use solar indices provided by other models (see Sec. 3.3) that are updated daily.

The Ionosonde Global index IG is produced by UK Solar System Data Centre (SSDC)[2] based on monthly averages of the noontime ionosonde measurements of f_oF_2- a measure of the highest radio frequency that can be reflected back by the F_2-layer (Liu et al., 1983). Being obtained from direct ionospheric measurements, the IG index performs better than solar indices; the IRI uses IR in the modelling of the F region peak (Fuller-Rowell et al., 2000). The IG is a global index (calculated as global median) and smooths out small scale variations. Consequently, the 12-month running average IG_{12} was found to better correlate with f_oF_2, and, therefore the IRI model uses IG_{12} by default (Bilitza and Xiong, 2021).

The geomagnetic indices used by IRI include:

- K_p - describes the impact of solar wind on the geomagnetic field within the 3-hour interval. The K_p is derived from sub-auroral magnetic measurements and equals to one of the standard numbers: $0°$, 0^+, 1^-, $1°$, 1^+, 2^-, $2°$, 2^+, ..., 9^-, $9°$, where $0°$ represents the lowest disturbance in magnetic field and the $9°$ corresponds to the highest disturbance (Menvielle and Berthelier, 1991);

- a_p - a linearized version of the K_p index, which maps the $[0°, 9°]$ K_p scale to a $[0, 400]$ scale of integers.

[2] https://www.ukssdc.ac.uk/

Within the IRI, the K_p index is used to derive the auroral boundaries (Zhang et al., 2010), when the a_p index is involved in calculation of electron density in the E-layer and the storm model of f_oF_2 in the auroral region (Mertens et al., 2013). Both indices are calculated bi-weekly.

3.3 E-CHAIM

Although IRI accounts for some irregularities at high-latitudes, it still poorly represents the auroral and polar cap ionosphere. For example, Themens et al. (2014) found significant errors in IRI's representation of the F_2-peak at high latitudes. In (Xiong et al., 2013), IRI demonstrated poor performance for electron density predictions in sub-auroral regions, compared to measurements from Challenging Minisatellite Payload (CHAMP) and Gravity Recovery and Climate Experiment (GRACE) satellites. Themens and Jayachandran (2016) showed that IRI poorly represents the TEC in the polar cap, auroral oval, and sub-auroral regions, particularly during high solar activity.

This motivated the creation of Empirical Canadian High Arctic Ionospheric Model (E-CHAIM)[3,4] - a model of the ionospheric electron density, which was developed as a replacement for the IRI for high geomagnetic latitudes ($> 50°$). The advantages of the E-CHAIM are:

- the model of quiet N_mF_2 and h_mF_2 was developed by using a few networks of ionosondes located at the high latitudes. These networks include: Canadian High Arctic Ionospheric Network (CHAIN)[5], Global Ionospheric Radio Observatory (GIRO)[6], United Kingdom Solar System Data Center (UKSSDC)[7] and others - with total number of 82 ionosondes. The E-CHAIM also includes the N_mF_2 perturbation model to

[3] https://www.rspl.ca/index.php/projects/chaim/e-chaim

[4] E-CHAIM, A-CHAIM, and R-CHAIM are supported under Defence Research and Development Canada contract number W7714-186507/001/SS and are maintained by the Canadian High Arctic Ionospheric Network (CHAIN) with operations support from the Canadian Space Agency.

[5] http://chain.physics.unb.ca/

[6] http://giro.uml.edu/

[7] http://www.ukssdc.ac.uk/

account for ionospheric storms. This altogether shows $\sim 30\%$ improvement in terms of accuracy over the IRI model in the auroral and polar regions (Themens et al., 2017);

- the topside electron density model in E-CHAIM is based on the NeQuick model, which is also a default option in the IRI. However, in E-CHAIM the NeQuick was re-fitted on a new data and re-parametrized, resulting in a $\sim 35\%$ accuracy improvement over IRI (Themens et al., 2018);

- E-CHAIM uses a principally different model of bottomside ionospheric profile. Instead of modelling electron density directly, E-CHAIM models the scale height $H(h)$ that defines a shape of the bottomside profile; the electron density is then derived from $H(h)$ using the $N_m F_2$ for scale. This shows accuracy improvement up to 40% during winter and up to 25% during summer (Themens et al., 2019);

- the upcoming E-CHAIM v4.0 will implement model of solar energetic proton precipitation, which is expected to improve model accuracy in the auroral and polar cap D-layer (Themens et al., 2022).

As in the case of IRI, the E-CHAIM is driven by solar, geomagnetic and ionospheric indices. The solar indices for E-CHAIM are updated daily and are publicly available[8,9]; these indices can be optionally used in IRI. The official website of E-CHAIM[10] features model implementations in C, Matlab and and IDL programming languages.

3.4 Electron Collision Frequency Model

As a radio wave propagates through the ionosphere, it creates an oscillating electric field. While the ions remain stationary due to high mass, the electrons respond to the oscillation of the field and collide with other particles. These collisions cause the wave to lose energy,

[8] https://chain-new.chain-project.net/echaim_downloads/apf107.dat
[9] https://chain-new.chain-project.net/echaim_downloads/ig_rz.dat
[10] https://chain-new.chain-project.net/index.php/projects/chaim/e-chaim

reducing the signal strength. The amount of attenuation is a function of electron density and collision frequency, which represents the number of collisions per unit time.

The monoenergetic collision frequency is defined as

$$\nu_m = n_g v_e Q_m(v_e), \tag{3.1}$$

where n_g is the number density of gas particles; v_e is the relative velocity between the colliding particles, but here we assume that ions/neutral particles are stationary and the velocity is equal to electron's velocity; $Q_m(v_e)$ - is the collisional cross-section, that depends on electron's velocity. (Shkarofsky et al., 1961)

However, the monoenergetic collision frequency is not typically used, because free electrons in the ionosphere have a Maxwellian distribution of energy. Therefore, it is more appropriate to define an effective collision frequency $\langle \nu_c \rangle$, which is the average of ν_m over the energy distribution function:

$$\langle \nu_c \rangle = \frac{4}{3\sqrt{\pi}} \int_0^\infty \nu_m(v) w^{3/2} \exp^{-w} \, dw, \tag{3.2}$$

where $w = m_e v_e^2 / 2k_B T_e$, k_B and T_e being the Boltzmann constant and the electron temperature respectively (Itikawa, 1971). For the rest of this work, $\langle \nu_c \rangle$ will be denoted ν_c and referred to as "collision frequency"

The electrons collide both with ions and neutral particles, so the total collision frequency will be the sum of electron-ion ν_{ei} and electron-neutral ν_{en} collision frequencies:

$$\nu_c = \nu_{ei} + \nu_{en}. \tag{3.3}$$

In the upper ionosphere, due to high levels of ionization, the electron-ion collisions dominate, while the electron-neutral collisions dominate in the lower ionosphere - in accordance with higher density of neutral particles (Itikawa, 1973).

Using lab-measured values of collision cross-section for N_2, O_2 and Ar particles (dominating in the lower ionosphere) and theoretical values for N, O, He and H atoms, Aggarwal et al. (1979) created a unified model of ionospheric collision frequency for the altitude range 50-500 km. As shown in the Fig. 3.3, the ionospheric ν_c exhibits near-power-law behaviour in the D-layer.

Aggarwal et al. (1979) noticed a small deviations in electron-neutral collision frequency due to the latitudinal and seasonal variations above 80 km. At 90 km height, the variations from the mean value are $\sim 15\%$ for latitudes in the range $0^\circ - 60^\circ$ and $\sim 20\%$ for different seasons. A quick estimation of the absorption factor (derived later in Sec. 4.2.3) for 45 MHz using typical daytime values for electron density leads to $\Delta f_a \approx 0.02$ (or ~ 0.2 in dB scale). This uncertainty may be impactful for precise modelling, but for now, we adopt a static model of collision frequency (shown in Fig. 3.3). The more in-depth investigation (and possible implementation) of the dynamic collision frequency model is left for future work. They also found a significant diurnal variation in the electron-ion collision frequency, which we also ignore since, in the D-layer, its contribution to the total collision frequency is a few orders lower than from electron-neutral collisions. For instance, the estimated daytime value of ν_{ei} at midday is $\sim 10^3$ Hz.

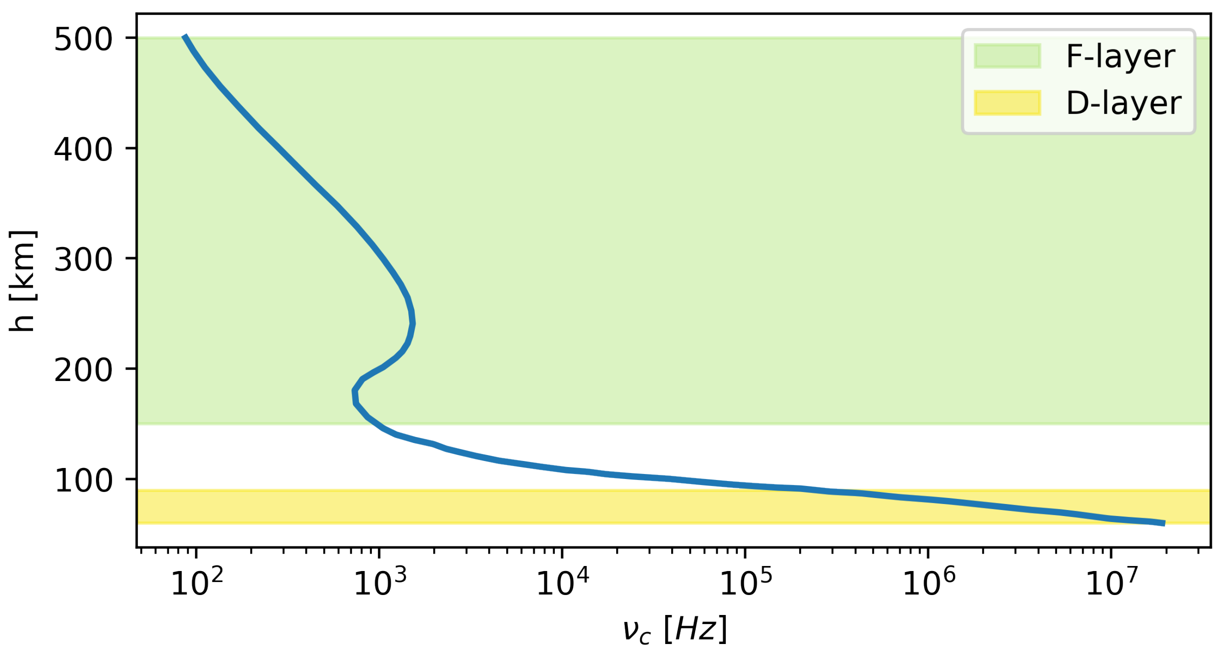

Figure 3.3: Model of electron collision frequency in the ionosphere adopted from (Aggarwal et al., 1979). The calculated ν_c corresponds to the average daytime conditions.

Chapter 4

Ionosphere Model for Global 21cm Experiments

The semi-empirical ionosphere models introduced in the previous chapter allow for generating ionospheric electron density profiles at any time and location. By calculating electron density on the instrument's line of sight and performing the ray tracing procedure, we can simulate dynamic ionospheric effects for the whole field of view. This simulation will allow us to study inhomogeneity and temporal effects of the ionosphere impact on global 21cm experiments. I developed and implemented such a model, which is presented in this chapter. One of the challenges in implementing the model was that the modelling of the entire sky requires a large number of calculations. At the same time, official implementations of IRI and E-CHAIM - were not optimized for bunch calculations over coordinate grids. Therefore, a significant focus during model implementation was put on the efficiency of computations, particularly optimization of the dependencies and parallelization of calculations.

In this chapter, I describe all the details behind implementing the dynamic model of the ionosphere, specifically developed for simulations of global 21cm experiments. The chapter starts with a theoretical derivation of the refractive index in the D-layer and F-layer of the ionosphere. I then discuss the implementation approach: the coordinate grid, discretization of different axes and final equations for attenuation and refraction, followed by an examination of model frequency constraints. The final section introduces the developed Python packages for IRI and E-CHAIM models, presents the Python implementation of the developed ionosphere model and, in brief, explains the program workflow.

4.1 Chromatic Ionospheric Distortions

4.1.1 Radio Wave Propagation in Cold Plasma

The movement of the EM wave through a medium can be described by defining a complex refractive index

$$\eta = n + i\kappa. \tag{4.1}$$

The real part n of the Eq. 4.1 is called the refractive index and indicates how much the light is bent (refracted) as the wave propagates through the medium, while the imaginary part κ is the extinction coefficient and tracks the absorption (Hecht, 2016).

Earth's ionosphere is a cold magnetized plasma. In such a medium, the complex refractive index is described by the Appleton-Hartree equation (Shkarofsky, 1961):

$$\eta^2 = 1 - \frac{x}{1 - iz - \frac{y^2 \sin^2 \varphi}{2(1-x-iz)} \pm \left[\frac{y^4 \sin^4 \varphi}{4(1-x-iz)^2} + y^2 \cos^2 \varphi\right]^{1/2}}. \tag{4.2}$$

Definition of terms in Eq. 4.2:

$x = \omega_p^2/\omega^2,$

$y = \omega_b/\omega,$

$z = \nu_c/\omega,$

$\omega_p = \sqrt{\dfrac{n_e e^2}{\varepsilon_0 m_e}}$ – angular electron plasma frequency,

$\omega_b = \left|\dfrac{eB}{m_e}\right|$ – cyclotron angular frequency,

ω – wave angular frequency,

e – electron charge,

m_e – electron mass,

n_e – electron number density,

ε_0 – permittivity of vacuum,

φ – angle between the wave vector and magnetic field.

The Eq. 4.2 is ready for wave propagation modelling. In our case, however, we will make a few assumptions that will significantly simplify the equation. These assumptions include ignoring the effect of the magnetic field and further simplification for different ionospheric layers based on their properties.

4.1.2 Magnetic Field and Approximations for Layers

The first step towards simplifying the Eq. 4.2 is estimating impact of the terms corresponding to the magnetic field. Usually, studies of the ionosphere in the context of global 21cm experiments assume magnetic field effect to be negligible (Vedantham et al., 2014; Shen et al., 2021; Datta et al., 2016), but, according to our estimates, the impact of the magnetic field can be significant, at least in the D-layer absorption. For example, Vedantham et al. (2014) (which will be referred to as Ved14), in their work, has estimated the influence of the Earth's magnetic field on the radio wave propagation in the ionosphere to be negligible; according to that estimation, the change in refraction index is $< 2\%$ in the D-layer and $< 0.01\%$ in the F-layer. We reproduced the estimation using the values close to those used in Ved14 (for details see Appendix A). We estimated that the influence of magnetic field changes the refractive index if the F-layer by about 0.01% at 30 MHz, confirming the estimation by Ved14; however, in the D-layer, our estimation shows the change in the refractive index up to 40% at 30 MHz for specific combination of wave polarization and angle with magnetic field.

The effect of the magnetic field adds another level of complexity, which must be modelled separately. Still, for simplicity, we ignore the magnetic field effect in the current model implementation. Possible next steps to introduce the magnetic field into the model are discussed in Sec. 6.

Ignoring the magnetic field simplifies Eq. 4.2 to

$$\eta^2 = 1 - \frac{(\omega_p/\omega)^2}{1 - i(\nu_c/\omega)} \tag{4.3}$$

As shown in Fig. 3.2, the typical electron density in the F-layer is order of $10^{11} - 10^{12}$ m^{-3}, which is much higher than in the D-layer - $10^8 - 10^9$ m^{-3}. On the other hand, according to (Aggarwal et al., 1979), the collision frequency in the F-layer is an order of $10^2 - 10^3$ Hz, which is much smaller than in the D layer - $10^6 - 10^7$ Hz.

If we ignore the effect of electron collisions by setting $\nu_c \to 0$, the refraction index in the F-layer becomes

$$\eta_F \approx \sqrt{1 - (\omega_p/\omega)^2}. \tag{4.4}$$

It is a real number and describes the refraction in the F-layer, while the imaginary part is negligible because of the low collision rate.

As for the D-layer, we can use the fact that the plasma frequencies are much smaller in the D-layer than in higher layers (see Sec. 3.1.1). Therefore the radio waves with $\omega \sim \omega_{p,D}$ will never reach the D-layer. This allows to assume $\omega_p/\omega \to 0$ in the Eq. 4.3. Using Taylor expansion up to the first order, the expression for the refraction index becomes

$$\eta = 1 - \frac{1}{2}\frac{(\omega_p/\omega)^2}{1 - i(\nu_c/\omega)} \tag{4.5}$$

Multiplying the numerator and denominator of the second term by $1 + i(\nu_c/\omega)$:

$$\eta = 1 - \frac{1}{2}\frac{(\omega_p/\omega)^2}{1+(\nu_c/\omega)^2} - \frac{i}{2}\frac{(\omega_p/\omega)^2}{1+(\nu_c/\omega)^2}\frac{\nu_c}{\omega} \tag{4.6}$$

The real part of the Eq. 4.6 is negligible compared to the F-layer refraction. The imaginary part cannot be ignored and is used to model attenuation in the D-layer

$$\eta_D = -\frac{1}{2}\frac{(\omega_p/\omega)^2}{1+(\nu_c/\omega)^2}\frac{\nu_c}{\omega} \tag{4.7}$$

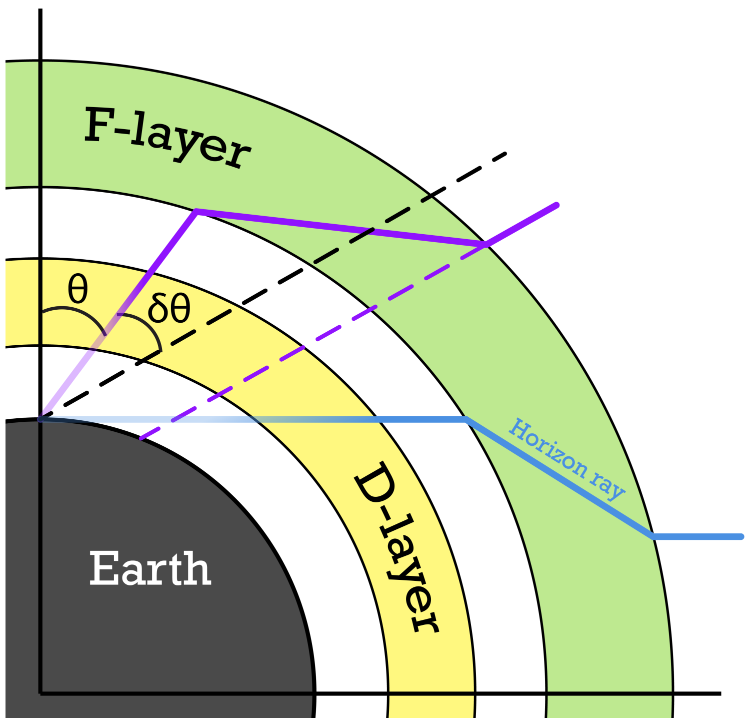

Figure 4.1: Two dominating ionospheric effects: attenuation in the D-layer and refraction in the F-layer. The refraction causes the incoming ray to bend towards the zenith. Consequently, the instrument observing at zenith angle θ will see the sky at $\theta + \delta\theta$. Although the continuation of the sky signal trajectory (dashed purple line) and the trajectory defined by $\delta\theta$ (dashed black line) are slightly misplaced, they are parallel to each other and end up at the same point in the sky at the infinite distance limit. Attenuation in the D-layer implies reducing signal strength via collisional absorption. The blue ray shows the case of refractions at the horizon, which allows to see the sky below the horizon line.

Figure 4.1 illustrates the effects of the ionosphere discussed earlier. First, the signal that comes from space is refracted in the F-layer. Because of the refraction, the instrument can see slightly below the horizon (blue ray in the picture). After that, the signal undergoes absorption in the D-layer.

4.2 Model Implementation Principle

The calculation of electron density profiles requires a lot of processing time. Therefore, the discrete coordinate grid must contain as few points as possible, but at the same time, it must be dense enough to describe the electron density accurately after interpolation. To maximize the model's efficiency, we first estimate the area in which electron density must be calculated (Sec. 4.2.1). After the area is defined, it is necessary to discretize the model in 3D space, which means defining vertical layers along the altitude axis and constructing a pixel grid in the plane of radial and angular axes (Sec. 4.2.2). We then implement a backward ray tracing procedure, tracking the imaginary signal from the position of the instrument back to the sky, calculating the ionospheric attenuation and refraction on the way (Sec. 4.2.3-4.2.4). The final part of the section describes model behaviour in extreme frequency cases (Sec. 4.2.5), introduces a model of tropospheric refraction, which is applied before ray tracing (Sec. 4.2.6), and overviews the process of accounting for the ionospheric effects in antenna temperature simulations (Sec. 4.2.7).

4.2.1 Angular Horizon Distance

Before calculating electron density, we must find the geographic coordinates range in the instrument's field of view. Horizon ray is the line of sight tangent to the Earth's surface. The instrument's field of view is outlined by a circle with angular radius α_h, defined as an angle between the zenith and the intersection of horizon ray and the upper limit of an ionospheric layer (see Fig. 4.2). We will denote α_h the angular horizon distance (AHD).

Assuming spherical symmetry for the Earth:

$$\alpha_h = \arccos\frac{R}{R+h_{in}} + \arccos\frac{R}{R+h_l}, \tag{4.8}$$

where R is the Earth's radius, h_{in} - altitude of the instrument above the sea level and h_l is the upper limit height of an ionospheric layer.

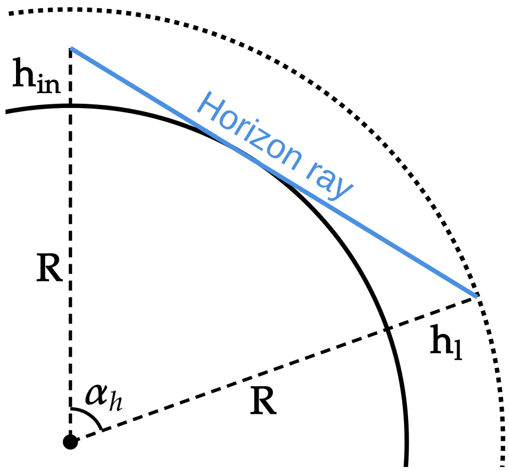

Figure 4.2: Angular horizon distance α_h for the instrument at height h_{in} above the sea level, which observes an ionospheric layer with the upper limit at height h_l.

Fig. 4.3 shows example calculations of the AHD for the instrument located at McGill coordinates and observing at the sea level. The D-layer's upper limit is at $\sim$ 90 km, resulting in $\alpha_h \sim 10°$, as shown in Fig. 4.3a. As for the F-layer, whose upper limit is at $h_l = 500$ km, the estimation shows an $\alpha_h \sim 23°$ (Fig. 4.3b). Because of refraction in the F-layer, the actual AHD will be slightly higher than the estimated value, which also must be considered in the model implementation.

4.2.2 Model Discretization

For further analysis, we will need to "pixelize" the visibility field to perform discrete electron density calculations. For this purpose we use the Hierarchical Equal Area isoLatitude Pixelization (HEALPix), which provides robust procedures for the pixelization of data on a sphere (Górski et al., 2005). The essential properties of HEALPix are:

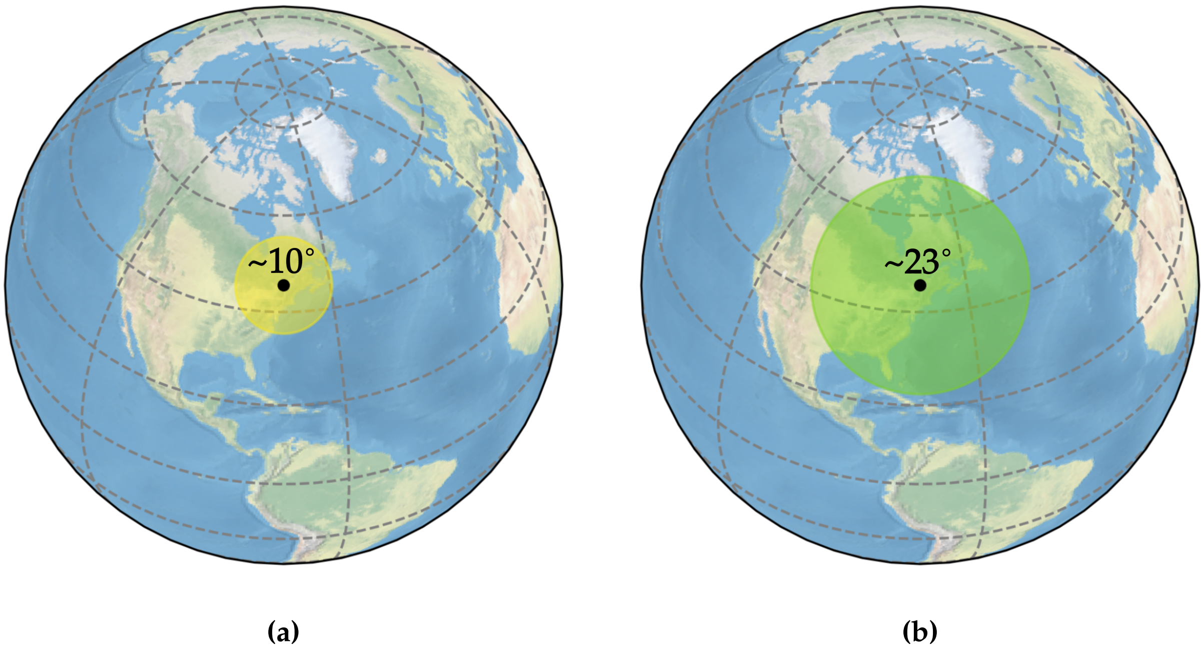

Figure 4.3: Estimation of an AHD for the instrument observing from McGill location at the sea level using typical values for upper layer limits of the D-layer **(a)** and the F-layer **(b)**.

1. At the given resolution, areas of all pixels are identical;
2. Pixels are located on lines of constant latitude;
3. The pixel grid has a hierarchical structure. At the lowest resolution, the sphere is split into twelve base pixels (see Fig. 4.4a). The resolution is controlled by `NSIDE` parameter, $\texttt{NSIDE} = 2^x,\ x \in \mathbb{Z},\ x > 0$. A one-step increase in resolution splits each pixel into four new ones - see Fig. 4.4b and Fig. 4.4b.

In this work, the Python implementation of HEALPix - the `healpy` library[1] is used. In particular, the `healpy` has implemented the `query_disc()` procedure that returns indices of pixels that lie inside the disc of a given radius at a specified location. This procedure is especially useful for implementing Eq. 4.8 in the final model.

[1] http://healpy.readthedocs.io

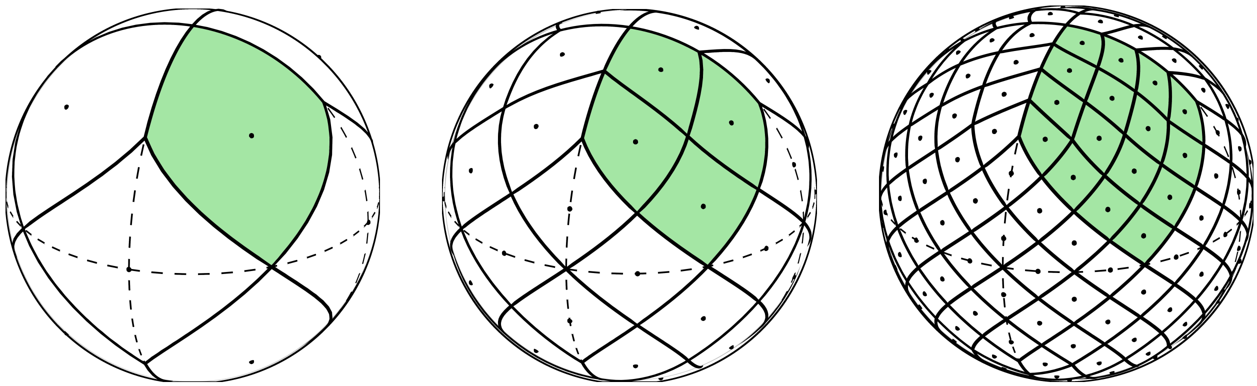

(a) `NSIDE = 1` **(b)** `NSIDE = 2` **(c)** `NSIDE = 4`

Figure 4.4: Orthographic view of the HEALPix partition of the sphere. In the base case, the sphere is split into twelve equal pixels. The `NSIDE` parameter controls the discretisation level of base pixels. The total number of pixels is $12 * \texttt{NSIDE}^2$. Reproduced from (Górski et al., 2005) for higher resolution.

The vertical extent of the ionospheric layer is described by h_{bot} and h_{top} parameters, which are corresponding bottom and top limit heights. Calculating characteristic profiles also requires vertical discretization, which splits the ionospheric layer into thinner sub-layers, as shown in Fig. 4.5. Electron density n_e and electron temperature T_e are calculated at each sub-layers; the model's vertical resolution is controlled by the N_l (number of sub-layers) parameter.

4.2.3 D-layer Absorption

The electric field of a wave travelling in a homogeneous ionospheric layer is given by

$$E(\Delta s) = E_0 \exp\left(-i\frac{\omega}{c}\eta\Delta s\right), \tag{4.9}$$

where E_0 is the initial amplitude of the wave, and Δs is the length of the propagation path. The imaginary part of the complex refractive index η is the one responsible to the exponential decay, therefore in Eq. 4.9 we keep only $i\eta_D$ part. The attenuation factor is

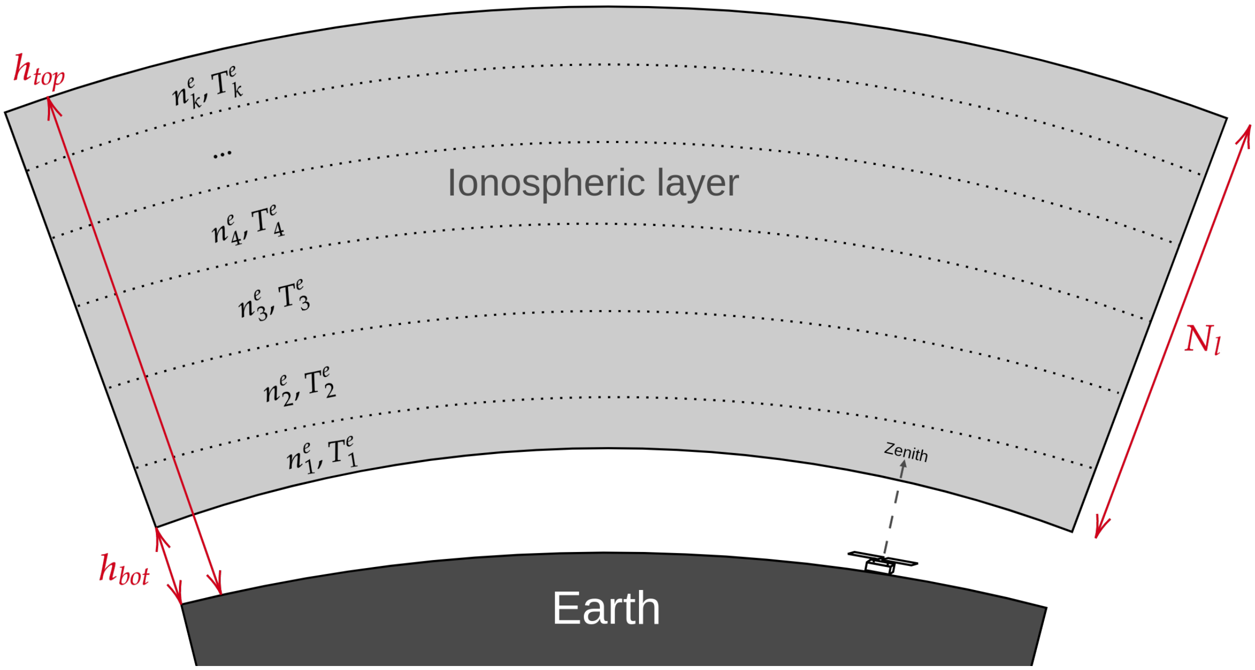

Figure 4.5: Characteristic parameters of an abstract ionospheric layer. The h_{bot} and h_{top} define bottom and upper limits of the layer, while N_l specifies the amount of sub-layers (vertical discretization).

defined as

$$f_a = \frac{E(\Delta s)}{E_0} = \exp\left(\frac{\omega}{c}\eta_D \Delta s\right). \tag{4.10}$$

In general, the attenuation factor depends on the direction of the observation, time and frequency. Note that $\eta_D \leq 0$ (see Eq. 4.7), and therefore the attenuation factor is always $f_a \leq 1$.

Following the vertical discretization introduced in section 4.2.2 and assuming $\eta_D(h_i)$ to be an average refractive index in the sub-layer of thickness Δs_i at height h_i, the total attenuation is calculated as

$$f_a = \frac{E(\Delta s)}{E_0} = \exp\left(\frac{\omega}{c}\sum_{i=1}^{N_l} \eta_D(h_i)\cdot \Delta s_i\right) = \prod_{i=1}^{N_l} f_a(h_i), \tag{4.11}$$

where $f_a(h_i)$ is the attenuation coefficient of a sub-layer at height h_i.

After absorption of the incoming wave's energy, the D-layer emits at the temperature of local electrons $T_e(h_i)$, which is a function of altitude. The total emission temperature

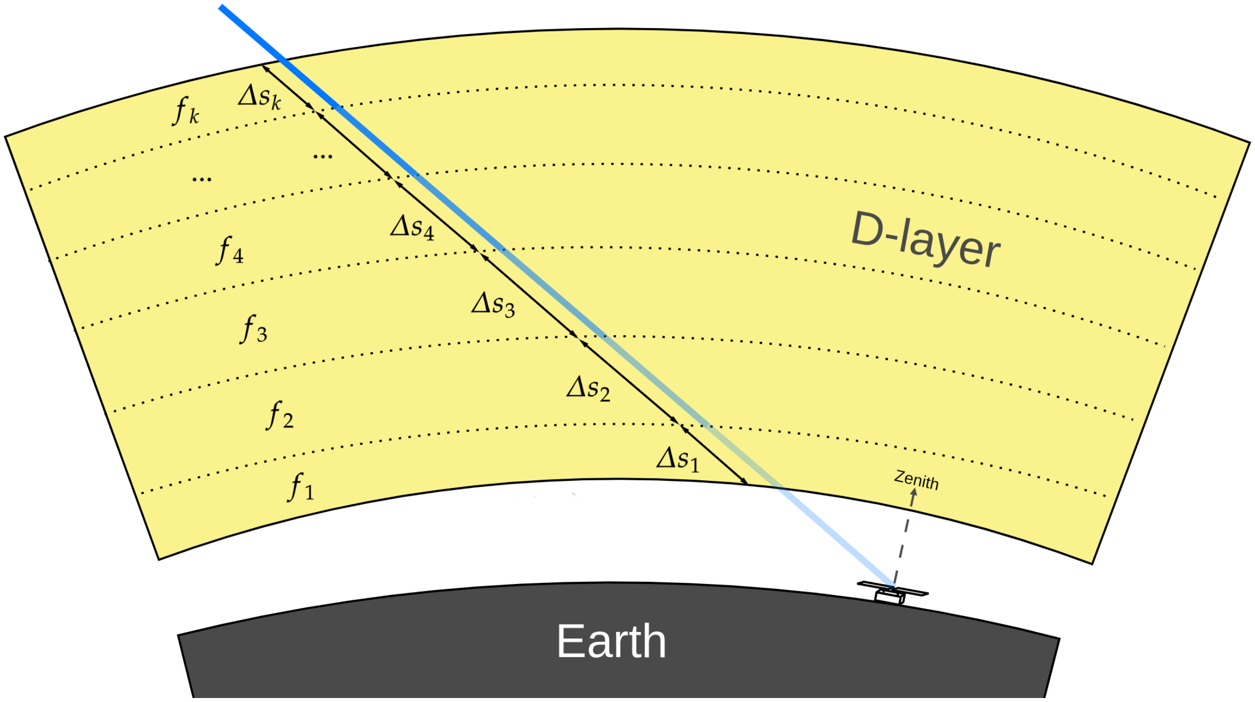

Figure 4.6: Implementation of the D-layer attenuation. The total attenuation is a product of attenuation factors f_i in sub-layers, which are exponentially proportional to the local value of attenuation coefficient $\eta_D(h_i)$ and the path length Δs_i travelled by the wave.

T_{em} is then a sum of local emission temperatures at each layer height h_i:

$$T_{em} = \sum_{i=1}^{N_l} [1 - f_a(h_i)]\, T_e(h_i) \tag{4.12}$$

4.2.4 F-layer Refraction

Refraction is described by Snell's law

$$\sin\theta_{i+1} = \frac{n_i}{n_{i+1}} \sin\theta'_i, \tag{4.13}$$

where θ'_i is the incident angle in the i-th medium, θ_{i+1} is the refracted angle in the next medium, n_i is the refraction index in the i-th medium. In the application to the ionosphere, $n_i \equiv \eta_F(h_i)$, where $\eta_F(h_i)$ is the refraction index in the F-layer at height h_i.

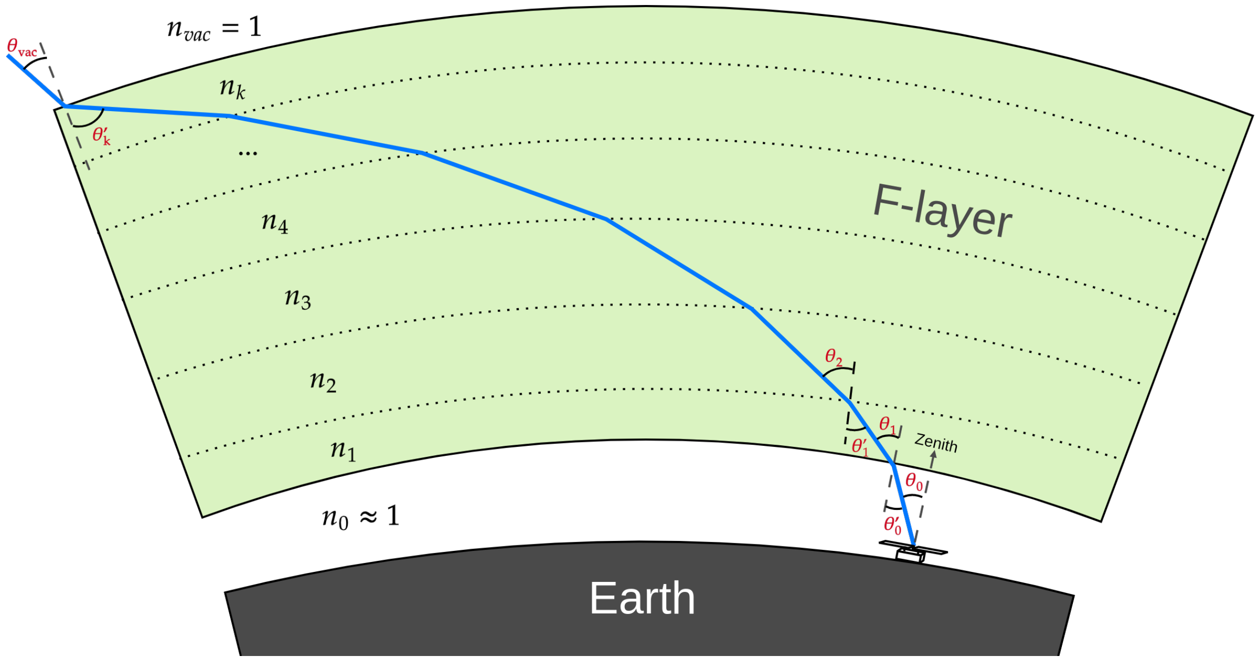

Figure 4.7: Implementation of the F-layer refraction. The total refraction angle is a sum of local deviations $\delta\theta_i = \theta_i - \theta'_{i-1}$, calculated by applying the Snell's law at sub-layers boundaries.

It is convenient to use backward ray tracing to track the refraction in the ionosphere (see Fig. 4.7). The process starts from the instrument's location - an imaginary ray with zenith angle θ_0 is sent towards the F-layer. Because of the Earth's curvature, the incident angle of the ray θ'_0 at the first sub-layer will be slightly different from θ_0. The refraction index of unionized air is close to unity: $n_0 = 1.0003$ (Hecht, 2016). The local refraction index of the ionosphere is calculated using Eq. 4.4.

Although real refraction is a continuous process, we model it with a discrete set of refraction surfaces - to simplify calculations. In this model, after the first refraction, the imaginary ray leaves the bottom surface at refracted angle θ_1. It moves towards the second surface with the incident angle θ'_1, gets refracted again, and the algorithm repeats for the next sub-layer. The total refraction repeats N_l times, according to the vertical grid resolution set. At the last surface, the outer medium is assumed to be a vacuum with refractive index $n_{vac} = 1$.

Finally, the total refraction angle $\delta\theta_{ion}$ is

$$\delta\theta_{ion} = \sum_{1}^{N_l+1} \theta_i - \theta'_{i-1}, \tag{4.14}$$

with $\theta_{N_l+1} \equiv \theta_{vac}$.

4.2.5 Extreme Frequency Cases

At high frequencies, the listed ionospheric effects are negligible. Indeed, for the D-layer attenuation:

$$\lim_{\omega\to\infty} f_a = \lim_{\omega\to\infty} \exp\left(\frac{\omega}{c}\eta_D \Delta s\right) = \lim_{\omega\to\infty} \exp\left(-\frac{\nu_c \omega_p^2}{2c(\omega^2 + \nu_c^2)}\Delta s\right) = 1. \tag{4.15}$$

For the refraction in the F-layer:

$$\lim_{\omega\to\infty} \eta_F = \lim_{\omega\to\infty} \sqrt{1 - (\omega_p/\omega)^2} = 1. \tag{4.16}$$

Ignoring the magnetic field in the Maxwell equations leads to the following dispersion relation:

$$c^2 k^2 = \omega^2 - \omega_p^2, \tag{4.17}$$

where k is the wave vector. Since electric field $|\vec{E}| \propto \exp\left(-i\vec{k}\vec{r}\right)$, for all signal frequencies lower than plasma frequency the wave amplitude will decrease exponentially (as illustrated in Fig. 4.8). Radio waves in the ionosphere stop propagating if, somewhere on their path, the local plasma frequency is greater than the signal frequency. Since $\omega_p \propto \sqrt{n_e}$, the low-frequency cut-off in the ionosphere is determined by the peak value of the electron density in the F-layer.

Refraction also increases with decreasing frequency. At low elevations, during the backward ray tracing procedure, the ray can bend so much that, at some point, the incident angle of the ray will reach zero. The tracked ray will be refracted back to the

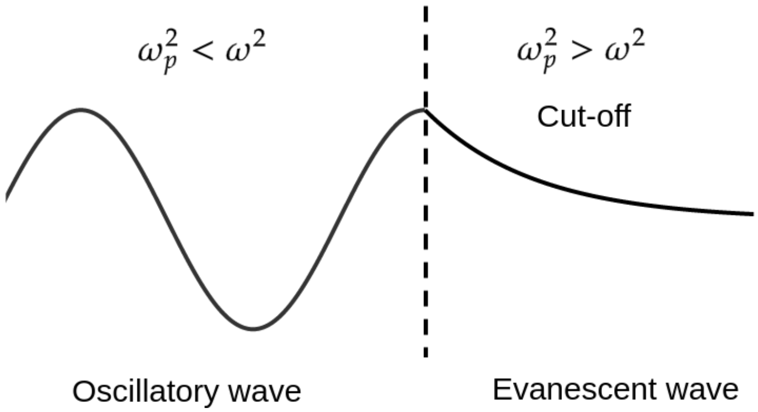

Figure 4.8: Time behaviour of the wave amplitude in plasma with different plasma frequencies ω_p compared to the wave frequency ω.

Earth's surface in these cases. This effect looks like a reflection at long distances and is called a "sky wave". Sky waves are used as a method of long-distance radio communication (Norton, 1941). However, in our case, the low elevation reflection makes it much harder to track the signal's origin in the given direction since the wave could be reflected several times from the ionosphere and Earth's surface, requiring much more computations. In this work, we assume the intensity of the reflected signal to be zero since:

1. the backtracked reflected ray undergoes at least three absorption interactions with the D-layer (instrument $\xrightarrow{\text{D-layer}}$ F-layer reflection $\xrightarrow{\text{D-layer}}$ ground reflection $\xrightarrow{\text{D-layer}}$ space) and the absorption in the D-layer grows exponentially with frequency decreasing. The tracked ray also at least once experiences energy loss during the ground reflection;
2. cosmology experiments, such as MIST, have lower sensitivity towards low elevations (see Sec. 5.4).

4.2.6 Tropospheric Refraction

The troposphere is the lowest layer of the Earth's atmosphere (non-ionized), extending from the ground to $\sim$ 13 km (in average). The gradient of the refraction index in the troposphere causes additional refraction of radio waves. The tropospheric refraction

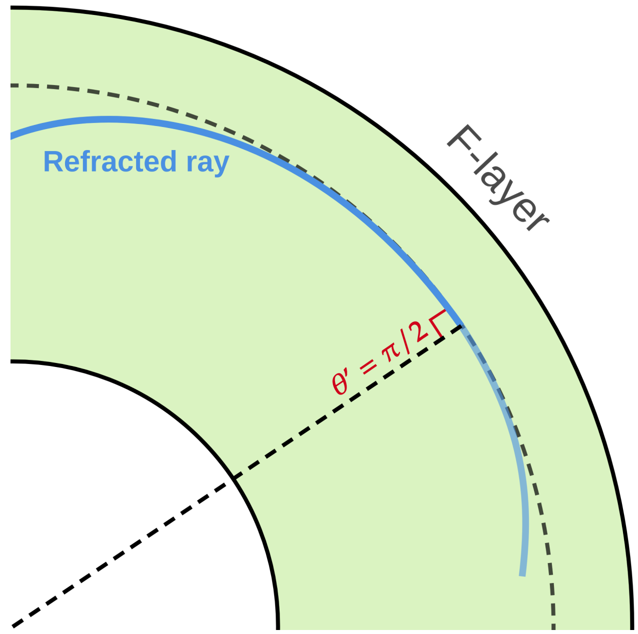

Figure 4.9: Illustration of low-elevation reflection, which happens when the low-frequency radio wave, which was sent in the direction close to the horizon, refracts back to the ground.

does not depend on the frequency of the signal if refraction index n does not change significantly on the wavelength scale. In our model, we use an approximation of tropospheric refraction for a typical atmosphere in the form

$$\theta_{trop} = [A_1 + B_1\alpha + C_1\alpha^2 + (A_2 + B_2\alpha + C_2\alpha^2)h_{in} + A_3h_{in}^2]^{-1}, \tag{4.18}$$

where θ_{trop} is the tropospheric refraction correction in degrees, α is the elevation angle in degrees, h_{in} is the height of the instrument above the surface measured in km, $A_1 = 1.314$, $B_1 = 0.6437$, $C_1 = 0.02869$, $A_2 = 0.2305$, $B_2 = 0.09428$, $C_2 = 0.01096$, $A_3 = 0.008583$, as recommended by International Telecommunication Union (ITU) (ITU-T, 2017). Figure 4.10 features Eq. 4.18 as a function of zenith angle $\theta = 90^\circ - \alpha$, assuming $h_{in} = 0$ km.

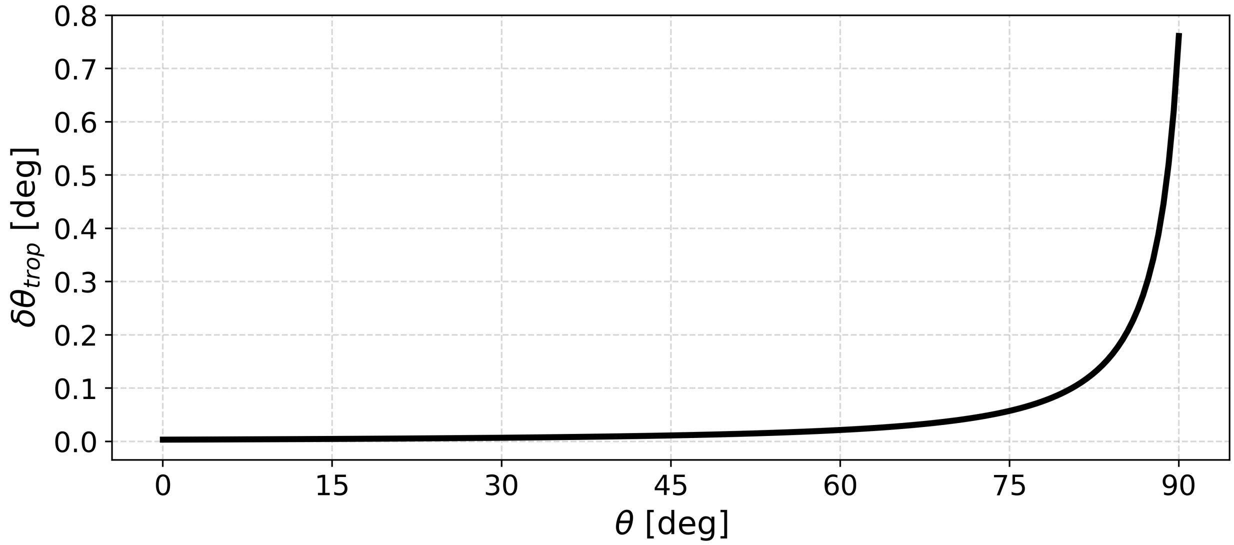

Figure 4.10: Calculated from Eq. 4.18 model of tropospheric refraction as a function of zenith angle θ at $h_{in} = 0$ km. The model does not depend on azimuth, frequency and time of observation.

4.2.7 Accounting for Ionospheric Effects

Corrections for the ionospheric effects can be applied by modifying the Eq. 2.1 (all quantities listed below are functions of frequency ν, zenith angle θ and azimuth ϕ):

1. the multiplicative loss factor represents absorption in the D-layer: $T_{sky} \rightarrow f_a T_{sky}$;
2. Emission in the D-layer depends on the loss factor and the electron temperature (see Eq. 4.12. It is simply added to the sky temperature after accounting for absorption: $f_a \cdot T_{sky} \rightarrow f_a \cdot T_{sky} + T_{em}$;
3. refraction in the F-layer modifies the zenith angle at which the model of sky temperature is evaluated: $T_{sky}(\theta) \rightarrow T_{sky}(\theta + \delta\theta_{ion})$. It is useful to notice that some other works (for example, (Vedantham et al., 2014)) apply ionospheric correction to the beam model instead of modifying the sky picture. Consequently, the "stretched" antenna beam integrates to a value larger than unity. In such a case, the integration must also include a correction for the beam stretching $\frac{\partial B}{\partial \theta}$ (which is missing in (Vedantham et al., 2014)). One can think of it as placing the stretched beam inside a sphere with

uniform emission temperature; without correction for beam sensitivity per angle, the integrated antenna temperature will be higher than that of the emitter, which violates the energy conservation principle.

4. since backward ray tracing starts from the instrument location, the tropospheric refraction must be applied before anything else. Therefore attenuation and emission in the D-layer are calculated at the modified zenith angle: $f_a(\theta) \to f_a(\theta + \delta\theta_{trop})$ and $T_{em} \to T_{em}(\theta + \delta\theta_{trop})$. Similarly, for the F-layer refraction: $\delta\theta_{ion}(\theta) \to \delta\theta_{ion}(\theta + \delta\theta_{trop})$.

The modified version of Eq. 2.1 is then

$$T_A = \frac{\displaystyle\int_0^{2\pi}\int_0^{\pi/2} B \cdot \Big(f_a\big(\theta + \delta\theta_{trop}\big)\, T_{sky}\big(\theta + \delta\theta_{ion}(\theta + \delta\theta_{trop})\big) + T_{em} \Big)\, \mathrm{d}\theta\, \mathrm{d}\phi}{\displaystyle\int_0^{2\pi}\int_0^{\pi/2} B\, \mathrm{d}\theta\, \mathrm{d}\phi}. \tag{4.19}$$

In Eq. 4.19, blue colour highlights the modifications reflecting the ionospheric impact; B, T_{sky}, f_a and $\delta\theta_{ion}$ depend on θ, ϕ and ν; the T_A and T_{sky} also depend on time.

4.3 Implementing Electron Density Models

The ionosphere model described in this work is developed in the context of the MIST experiment. Since all existing MIST data pipelines and simulation software are written in Python, this programming language was also chosen to implement the ionosphere model. However, the empirical ionosphere models, such as IRI and E-CHAIM, do not have native Python implementations, which in turn, requires the creation of Python wrapper solutions.

4.3.1 The `iricore` Python Package

The `iricore` package[2] is a Python wrapper for the IRI-2016 and IRI-2020 models. The package was first introduced in the MIST Memo 62 (Bidula, 2022b). The `iricore` consists of:

- the IRI source code developed in Fortran 77;
- a higher level wrapper implemented in Fortran 90, which implements inner loops over the coordinate grid to minimize the number of communications with Python;
- a Python interface, which uses the `ctypes` library to send requests and receive output from the compiled IRI source code.

A High-level Python interface also includes a routine that reads IRI data only once in advance, saving time significantly during execution. This single solution increased the overall performance by the factor of ~ 50 compared to the previously existing `iri2016` wrapper[3]; the proposed changes were also adopted in the official IRI model. The structure of the `iricore` is visualized in Fig. 4.11. Overall, the developed algorithm shows up to ~ 100 times better performance (Bidula, 2022b).

4.3.2 The `echaim` Python Package

The official E-CHAIM model has only Matlab, IDL and C implementations. Therefore, it was necessary to develop a new Python wrapper for E-CHAIM. For this purpose, a C implementation was selected since it is the most convenient to work with from the Python perspective. As in the case of `iricore`, the `echaim` consists of the C source code compiled into a shared library and a Python interface that implements communication processes through `ctypes`.

The developed package was uploaded to Python Package Index (PyPI) and made available for public use. The package documentation includes an overview, installation

[2] https://github.com/MIST-Experiment/iricore
[3] https://github.com/space-physics/iri2016

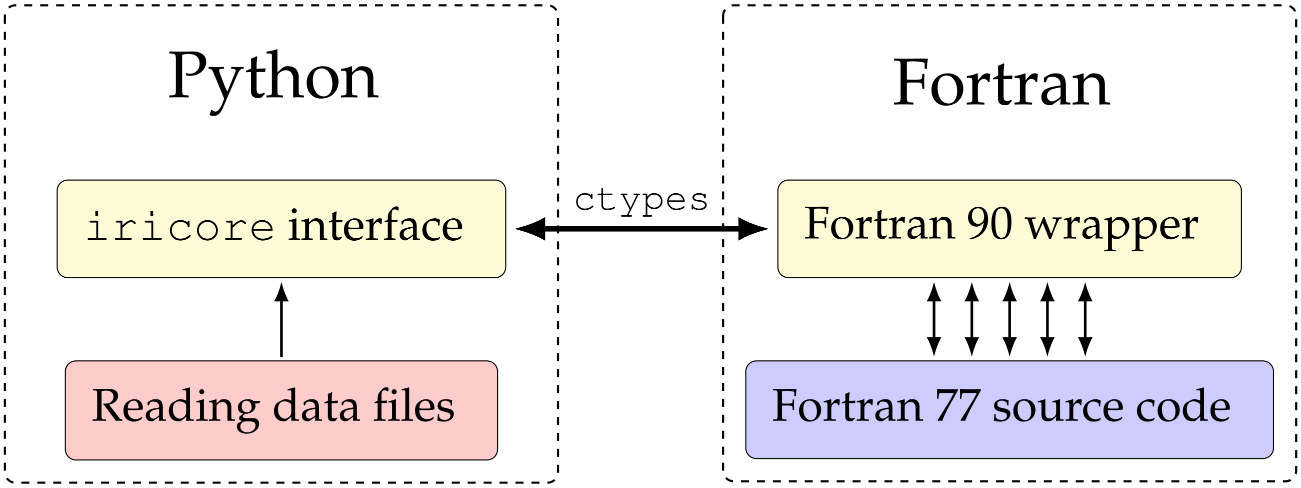

Figure 4.11: Diagram of the `iricore` implementation. The data files are read only once for efficiency (in contrast with the official implementation) in the Python interface. The Python part then communicates with created high-level Fortran-90 wrapper, which, in turn communicates with the IRI source code

.

notes, complete functionality reference and some examples[4]. The version of E-CHAIM used in the package at this moment is 3.2.4, but is expected to be updated in the future.

4.4 The dionpy Package

The `dionpy` Python package implements the algorithm described in Sections 4.1-4.2 and performs calculations based on `iricore` and `echaim` libraries (Bidula, 2022a). The package is hosted and maintained on GitHub[5]. In addition, documentation and examples are available at the Read the Docs website[6].

The `IonFrame` is the base user-interaction class, representing the state of the ionosphere at a specific point in time. It provides access to electron density, electron temperature, D-

[4] https://echaim.readthedocs.io/en/latest
[5] https://github.com/MIST-Experiment/dionpy
[6] https://dionpy.readthedocs.io/en/latest/

layer attenuation and emission, and F-layer refraction data, both in numeric and predefined graphical formats. The program workflow goes as follows:

1. the user initiates an `IonFrame` instance and specifies required model parameters - instrument position and time of observation;

2. based on the instrument position and other parameters (such as upper limits of ionospheric layers), the program selects a grid of geographical coordinates needed for model evaluation. The selection is made by estimating the angular horizon distance α_h and finding all points on the HEALPix grid that lie in a circle of radius α_h;

3. the program performs calculations of ionospheric n_e and T_e in different layers separately (using either `iricore` or `echaim`) and stores them in memory. Computations are performed in parallel using the Python `multiprocessing` module.

4. as an optional step, it is possible to save the calculated model to the file using the Hierarchical Data Format (HDF) technology (The HDF Group, 2023). Loading a model from the file can significantly save computational time if the model is reused;

5. depending on the further request, the model performs the ray tracing simulation of attenuation or refraction based on the provided observation frequency and grid of elevation and azimuth angles. The elevation/azimuth grid is transformed into a latitude/longitude grid for each height during the simulation. The transformed grid usually does not match the precalculated grid; in such a case, to estimate local values of n_e and T_e from the precalculated data, bilinear interpolation using the nearest HEALPix pixels is performed.

A single `IonFrame` is insufficient to characterize a long set of observations. At the same time, calculating a new ionosphere model for each point of time is unreasonable, given the computational costs. For example, the MIST experiment records antenna temperature every ~ 41 s. For the observational time of 2 weeks, this would require around 30,000 calculated models. As a solution, the `IonModel` class was introduced. It consists of several `IonFrame` objects, equally separated in time. The `IonModel` performs the linear interpolation of n_e and T_e data from two adjacent `IonFrame` models to get an `IonFrame` for a specific time.

The workflow for the `IonModel` is the same as for the `IonFrame`, except now the user has to specify two times (start and end) of observation and a "minutes per frame" parameter. An additional feature of the `IonModel` is the ability to generate animated graphs representing the change of ionospheric effects in time.

Chapter 5

Results of Model Applications

This chapter demonstrates several examples of `dionpy` applications. Sec. 5.1 explains model's basic plots, such as maps of electron density or refraction. Sec. 5.2 compares the developed model with the more straightforward analogue that assumes a homogeneous ionosphere with some average electron density. The possible uncertainties in IRI and E-CHAIM models are explored in Sec. 5.3 (in the application of integrated electron density calculation); this was done using the developed `iricore` and `echaim` wrappers. The analysis of ionospheric effects in the simulation of antenna temperature (using the actual antenna beam and empirical foreground model) was performed in Sec. 5.4. The final section compares preliminary data from the MIST deployment at MARS in 2020 with ionosphere simulations made with `dionpy` for the location and time of observations.

5.1 Basic Examples of Model Visualization

Before going into more complex simulations, it is necessary to understand the basic `dionpy` behaviour. For this, we will use model visualizations made with the standard plotting procedures included in the module. The `dionpy` also includes methods for animation generation to represent the temporal evolution of the model; those animations follow the same plotting style as presented in this section. Fig. 5.1 and Fig. 5.2 show examples of calculated ionosphere model with `dionpy` for the location of the MIST deployment in Death Valley on May 7, 2022. The colour maps presented in polar plots correspond to the visible sky above the observer with a zenith angle along the radial axis and the azimuth along the angular axis ($0^\circ \equiv$ North, $90^\circ \equiv$ West, etc.). The central point corresponds to the zenith, while the plot's boundary represents the horizon line.

The attenuation and refraction in Fig. 5.2 follow the same colouring principle - more saturated colours represent higher ionospheric distortion; in case of absorption, it means lower attenuation factor, in case of refraction - more bending in degrees. By default, all attenuation, emission and refraction simulations include correction for tropospheric refraction (Sec. 4.2.6). The colour map in the plot of attenuation intentionally includes $f_a = 1$ as an upper limit for better visual perception.

The electron density and temperature calculations were done using the IRI-2020 model. In simulation the default `dionpy` model parameters were used; this includes:

- `NSIDE` = 64;
- N_l = 100 for both D-layer and F-layer;
- h_{bot}, h_{top} are (60 km, 90 km) for the D-layer, and (150 km, 500 km) for the F-layer.

Explanation of model parameters is provided in Sec. 4.2.2.

The close correlation between ionospheric effects and ionospheric electron density becomes obvious after comparing Fig. 5.1 and Fig. 5.2. Although emission in the D-layer also depends on electron temperature, the minor variations in T_e (~ 4 K in Fig. 5.1b) do not affect emission much. As a result, T_{em} highly correlates with n_e in the D-layer.

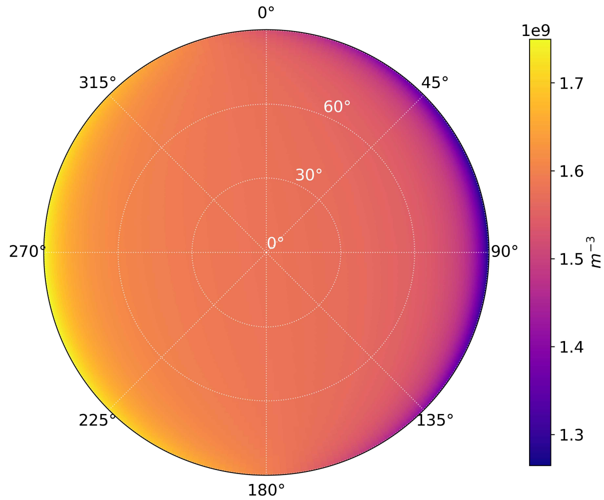

(a) Average n_e in the D-layer

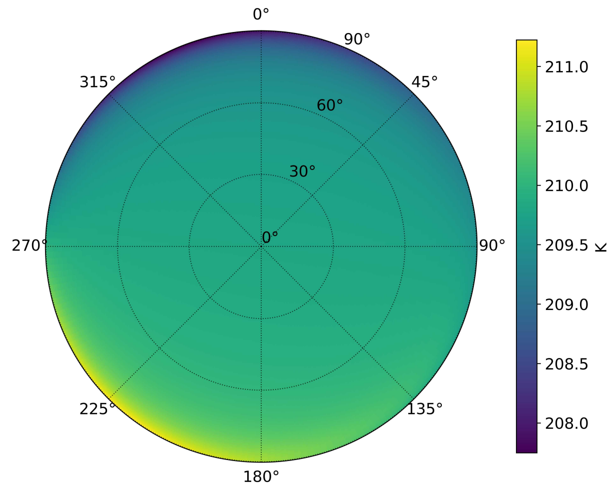

(b) Average T_e in the D-layer

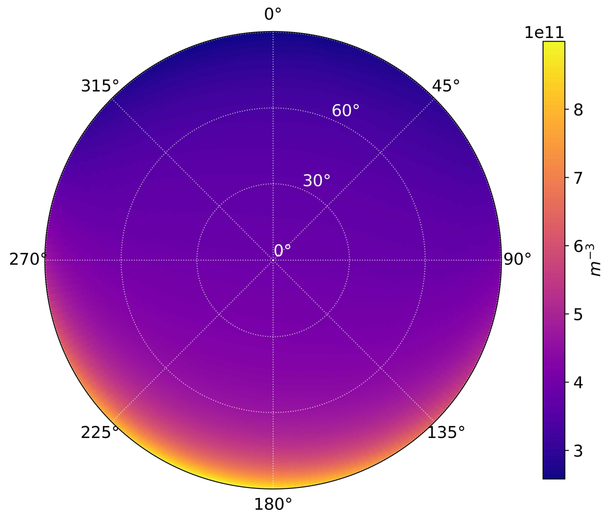

(c) Average n_e in the F-layer

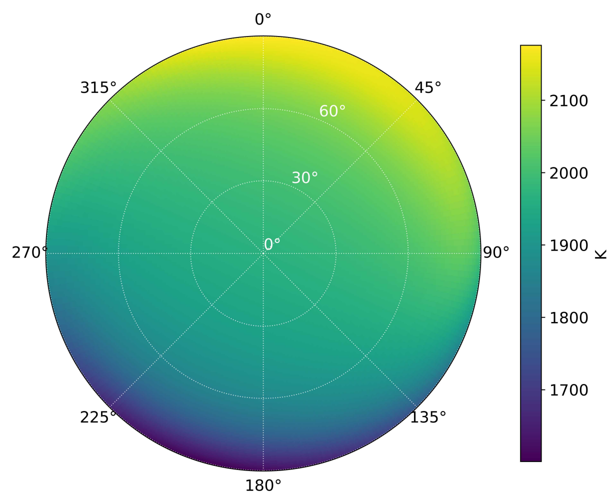

(d) Average T_e in the F-layer

Figure 5.1: Visualization of average electron density and electron temperature on the line of sight. The model was calculated at MIST deployment location in Death Valley, NV ($37.21333°$ N, $117.09111°$ W) for May 7, 2022, 23:00 UTC, which corresponds to 16:00 in the local timezone (PDT).

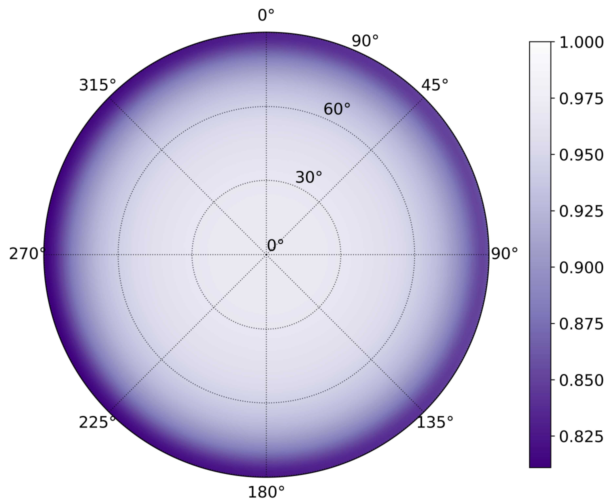

(a) Attenuation factor in the D-layer

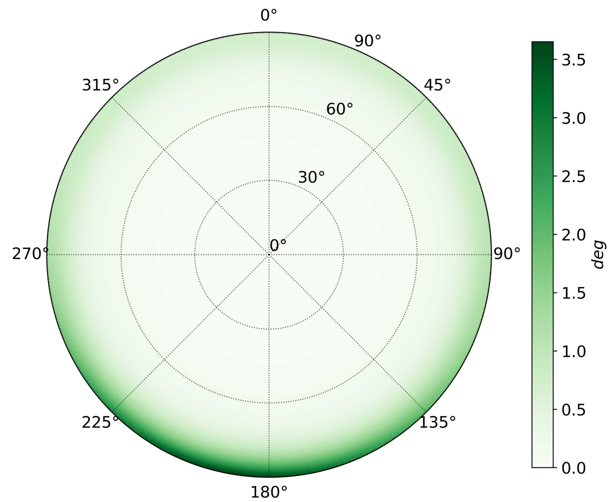

(b) Refraction angle in the F-layer

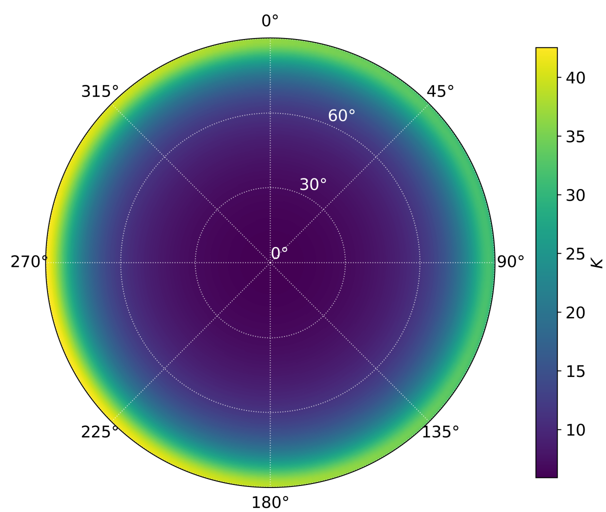

(c) Emission temperature in the D-layer

Figure 5.2: Visualization of attenuation factor, emission temperature and refraction angle on the line of sight. The model was calculated at MIST deployment location in Death Valley, NV ($37.21333°$ N, $117.09111°$ W). for May 7, 2022, 23:00 UTC, which corresponds to 16:00 in the local timezone (PDT). Ionospheric effects were calculated for observational frequency of 45 MHz.

5.2 Comparison with the Homogeneous Ionosphere Model

Although the `dionpy` goes beyond the static uniform ionospheric electron density assumption, it is still expected to yield similar results in scenarios close to those that used a homogeneous and static ionosphere. This section demonstrates how `dionpy` repeats and extends the homogeneous ionosphere model by evaluating and comparison of `dionpy` in similar conditions used in the work of Ved14.

Ved14 model the F-layer as homogeneous shell between the heights of 200 km and 400 km with assumed constant electron density $n_e = 5 \times 10^{11}$ m^{-3} which is considered to be a typical winter-time electron density value at mid-latitudes where LOFAR is situated.

To reproduce this scenario, the `dionpy` was evaluated at the Low-Frequency Aaray (LOFAR) location during the winter time with lower and upper limits of the F-layer set to the 200 km and 400 km correspondingly. It was found that according to the IRI model, the state of the ionosphere at the specified location was very close to one described in Ved14 on 15 Feb 2022 at 12:00 UTC with average electron density $n_e = 4.95 \times 10^{11}$ m^{-3}. The resulting electron density and refraction maps are shown in Fig. 5.3. The effect of low-elevation reflection (described in Sec. 4.2.5) can be noticed in Fig. 5.3b.

Fig. 5.4 shows side-by-side comparison of frequency profiles for different zenith angles θ. As expected, the model generated with `dionpy` generally follows the same behaviour as the simulation from Ved14. Moreover, the filled area behind average curves in Fig. 5.4b shows possible distribution of refraction angles depending on the azimuth of observation.

For the D-layer extending from 60 km to 90 km Ved14 used electron density $n_e = 5 \times 10^8$ m^{-3} and collision frequency $\nu_c = 10$ MHz. We found the `dionpy` model generated for LOFAR location on 15 Feb 2022, 7:30 UTC to be suitable for this comparison, since according to the IRI, the average electron density in the D-layer equals 5.24×10^8 m^{-3}. The resulting electron density and attenuation maps are shown in Fig. 5.5.

As in the case of refraction, the absorption profiles generated with `dionpy` and shown in Fig. 5.6 behave similarly to those calculated with the static homogeneous ionosphere

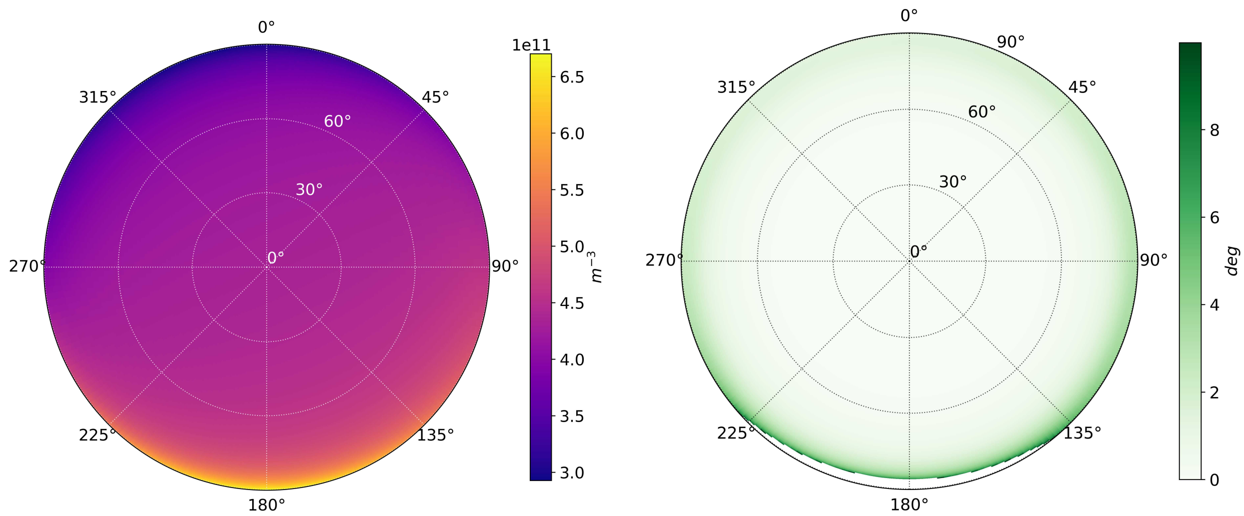

(a) Average n_e in the F-layer

(b) Refraction angle in the F-layer

Figure 5.3: Average electron density **(a)** and refraction angle **(b)** maps generated for LOFAR location ($52.90889°$ N, $6.86889°$ E) on 15 Feb 2022 at 12:00 UTC. The average electron density in panel **(a)** equals to 4.95×10^{11} m^{-3} and is close to that used in Ved14. The refraction in panel **(b)** was calculated for observational frequency of 30 MHz. At such a low frequency, the low-elevation reflection effect can be noticed around $\phi = 180°$, which corresponds to the region of highest electron density in panel **(a)**.

model with approximately the same average electron density. Still, the profiles calculated with `dionpy` introduce azimuthal variability that could potentially impact the recorded antenna temperature.

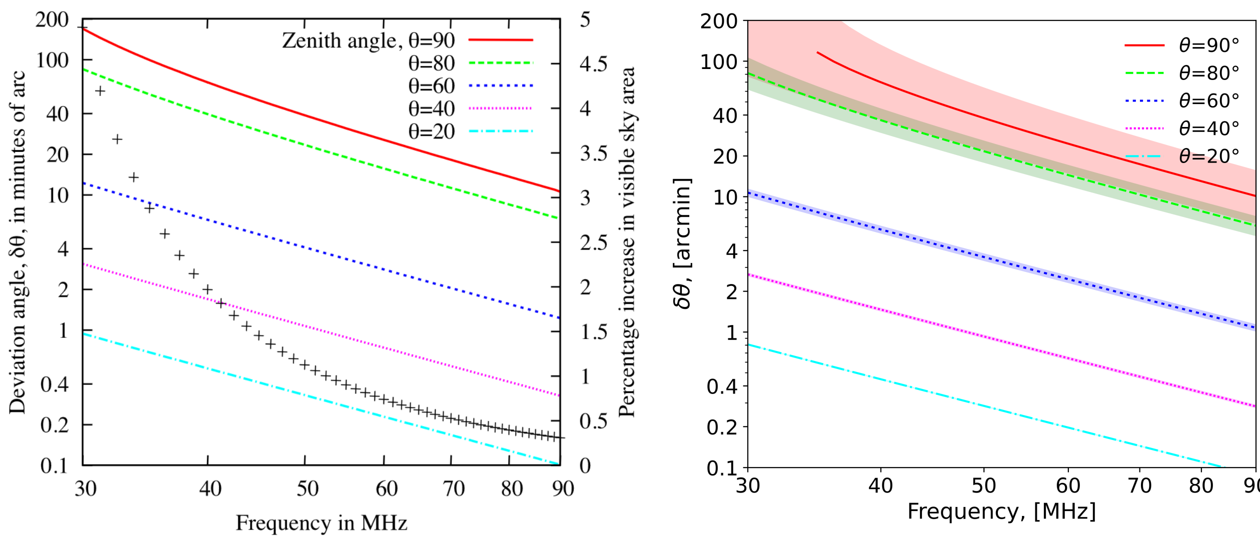

(a) Refraction in a homogeneous ionospheric shell with $n_e = 5 \times 10^{11}$ m^{-3}. "+" markers show the increase in area of visible sky (right axis). Reused from (Vedantham et al., 2014) with permission.

(b) Average refraction in an inhomogeneous ionospheric layer generated with IRI ($\langle n_e \rangle = 5 \times 10^{11}$ m^{-3}). Filled areas behind curves represent variation of refraction in dependence of azimuth (see Fig. 5.3b).

Figure 5.4: Calculated refraction angle for the ionospheric F-layer extending from 200 km to 400 km for the location of LOFAR instrument ($52.90889°$ N, $6.86889°$ E). Panel **(a)** shows the result for the static uniform electron density, while panel **(b)** features the model generated with `dionpy` for 15 Feb 2022 at 12:00 UTC. The cut-off of the red curve in panel **(b)** is due to the low-elevation reflection effect (see Fig. 5.3b).

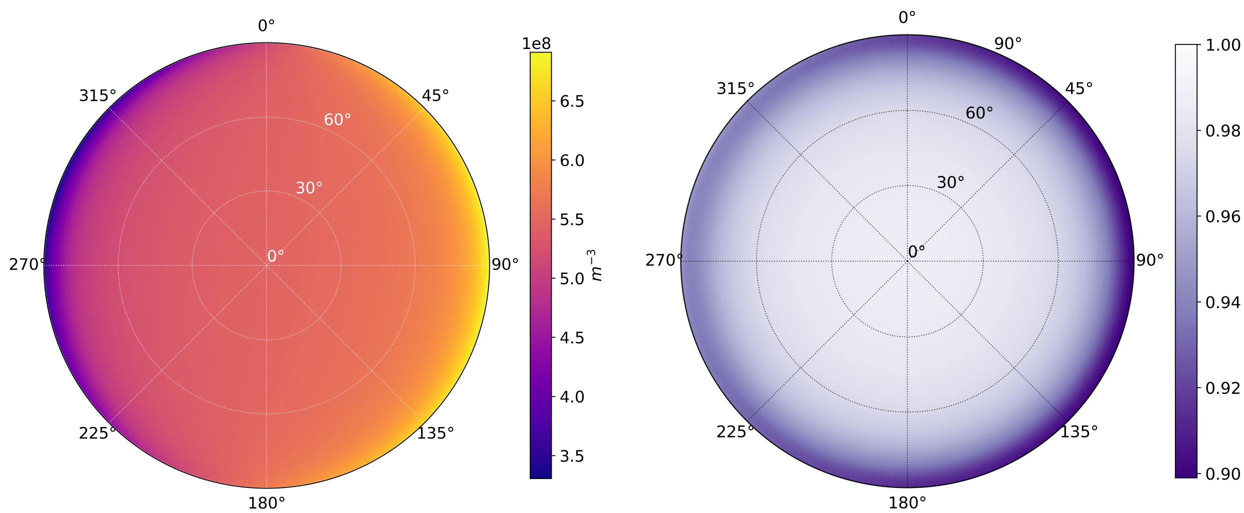

(a) Average n_e in the D-layer

(b) Attenuation factor in the D-layer at 40 MHz

Figure 5.5: Average electron density **(a)** and attenuation factor **(b)** maps generated for LOFAR location ($52.90889°$ N, $6.86889°$ E) on 15 Feb 2022 at 7:30 UTC. The average electron density in panel **(a)** equals to 5.24×10^8 m^{-3} and is close to that used in Ved14.

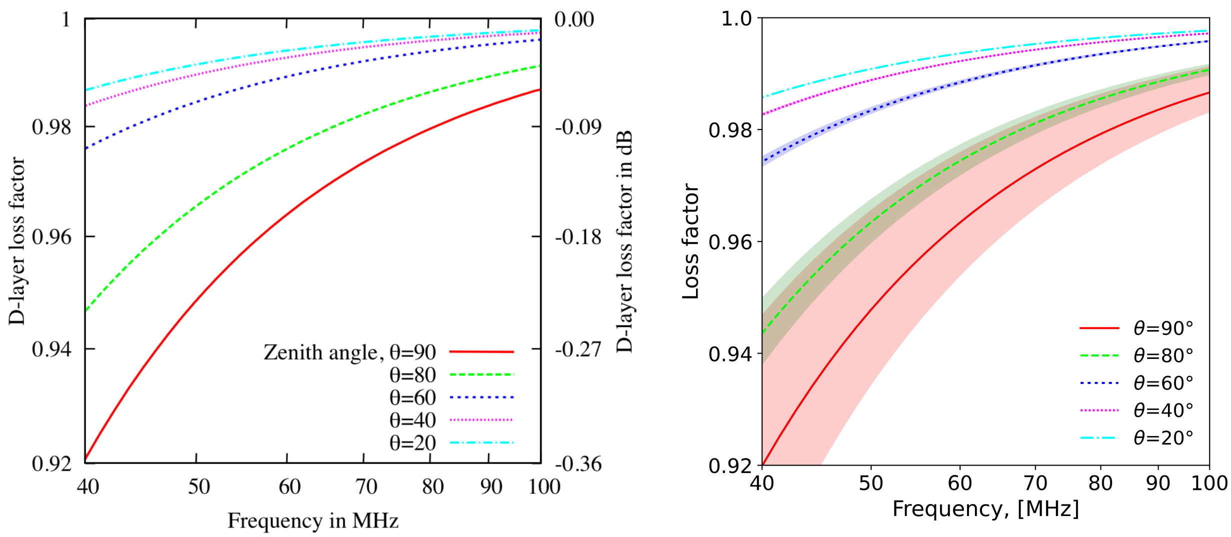

(a) Absorption in a homogeneous ionospheric shell with $n_e = 5 \times 10^8$ m^{-3}. Reused from (Vedantham et al., 2014) with permission.

(b) Average absorption in an inhomogeneous ionospheric layer generated with IRI ($\langle n_e \rangle = 5.24 \times 10^8$ m^{-3}).

Figure 5.6: Calculated attenuation factor for the ionospheric D-layer extending from 60 km to 90 km for the location of LOFAR instrument ($52.90889°$ N, $6.86889°$ E). Panel **(a)** shows the result for the static uniform electron density, while panel **(b)** features the model generated with `dionpy` for 15 Feb 2022 at 7:30 UTC. Filled areas behind curves in panel **(b)** represent variation of absorption in dependence of azimuth (see Fig. 5.5b)

5.3 Comparing Ionosphere Models with GNSS-Derived TEC

Neither IRI nor E-CHAIM provide error estimation for the modelled electron density. While it is possible to perform a selected comparisons with measurements from local stations (Cherniak et al., 2013; Abdu et al., 2004; Kumar et al., 2014), the derivation of the general models' uncertainties is a highly complex task, especially given that both IRI and E-CHAIM are composed of several altitude-specific models with data derived from hundreds of different instruments.

The comparisons made in this section aim to provide a "feeling" of possible models' uncertainties. As a reference dataset we chose the TEC maps provided by Crustal Dynamics Data Information System (CDDIS)[1] (Noll, 2010). The CDDIS TEC maps are derived from hundreds of GNSS stations scattered all over the planet. GNSS receivers can measure TEC through the impact of the ionosphere (phase delay) on the signal emitted by satellites on two frequencies: L1 (1575.42 MHz) and L2 (1227.60 MHz) (Leick et al., 2015). The CDDIS database provides access to TEC solutions from different analysis groups that use different methodologies; in this work, we use the dataset from Jet Propulsion Laboratory (JPL) group that utilizes the precise point positioning method of TEC calculation (Zumberge et al., 1997).

TEC maps were calculated for July 16, 2022. To match the CDDIS data, vertical electron density profiles provided by IRI and E-CHAIM were integrated within the range from 90 km to 2000 km (upper limit of both models) at the same set of geographical coordinates.

Fig. 5.7 compares global TEC maps from IRI and CDDIS. It is clear that IRI generally follows the real picture of electron density distribution. However, the TEC count calculated with IRI is substantially lower compared to CDDIS, up to ~ 30 TECU (1 TECU $= 10^{16}\,\mathrm{m}^{-2}$), as can be seen in Fig. 5.8. This can be partially explained by the contribution to the GNSS-derived TEC by the plasmasphere from above 2000 km. This contribution is maximum at the equatorial region where the ray from satellites traverses a longer distance through the

[1] https://cddis.nasa.gov/Data_and_Derived_Products/GNSS/atmospheric_products.html

plasmasphere compared to the higher latitudes and can vary from 10% during nighttime to 60% during daytime (Yizengaw et al., 2008).

The comparison for high latitudes is shown in Fig. 5.9; in this figure, all models were evaluated in the operational area of the E-CHAIM model. Once again, TECs from semi-empirical models of the ionosphere show much lower values compared to CDDIS - up to ~ 14 TECU (see Fig. 5.10), but this time the plasmaspheric TEC has relatively little impact. Another possible cause of discrepancy could be the instrumental biases (also known as differential code biases (DCBs)), which are the systematic errors caused by different, frequency-dependent processing times of L1 and L2 signals (Warnant, 1997; Montenbruck et al., 2014). The DCBs vary between instruments and evolve with time (for instance, due to changing surrounding temperature); different studies of particular receivers estimate the TEC difference introduced by DCB from a few TECU to tens of TECU (Li et al., 2018; Mylnikova et al., 2015; Themens et al., 2015). Apart from the DCB that impacts the GNSS-based TEC, semi-empirical models have their own biases. For instance, Themens et al. (2021) showed that E-CHAIM (with errors between 0.4 and 5.0 TECU) and IRI (with errors between 1.0 and 7.4 TECU) tend to underestimate the TEC at high latitudes.

Fig. 5.11 provides an alternative view of the data presented in Fig. 5.9; it shows the correlation of E-CHAIM and IRI models with respect to CDDIS data. For illustration, the first-order polynomials have been fitted to the data and used to bring all data to the same scale; Fig. 5.12 shows the result of the correction. The significant deviation from the correlation line can be noticed for the E-CHAIM model in Fig. 5.12; this is the result of the E-CHAIM being thorough in modelling the ionospheric features in auroral and polar regions, while the JPL TEC maps use interpolation between the closest stations (which are pretty far from the polar cap, see Fig. 5.9).

Summing it up, the ionospheric models can have unpredictable (and sometimes significant) errors. The possible errors must be accounted for in the direct calculations of ionospheric

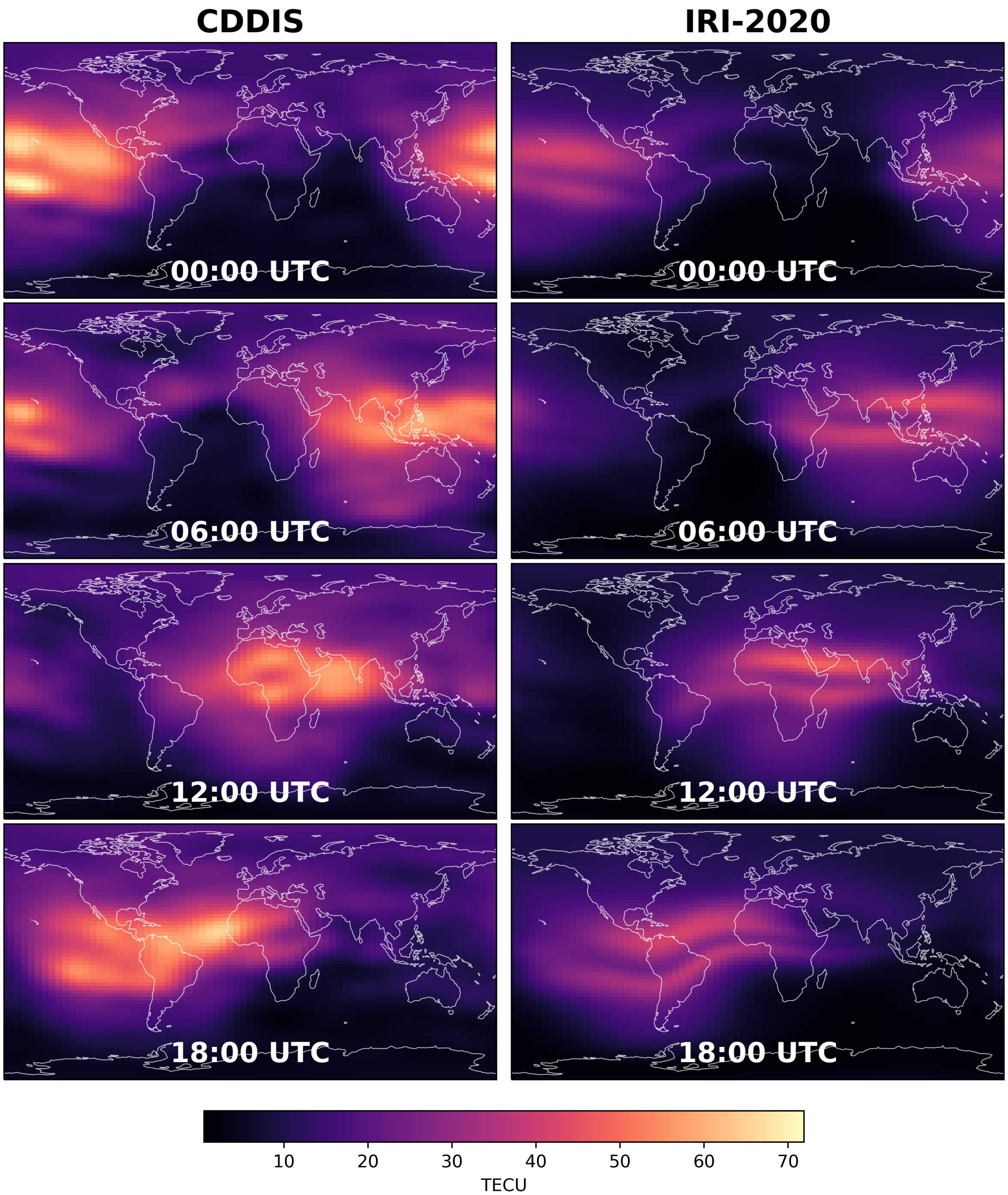

Figure 5.7: Comparison of CDDIS global TEC data with integrated TEC from the IRI model (in the $60 - 2000$ km range). The simulation was performed for 16 July 2022. Although IRI generally follows the real picture of electron density distribution, the absolute differences are significant. The residuals between the CDDIS data and the IRI model reach up to ~ 35 TECU near the equator and around ~ 10 TECU anywhere else (see Fig. 5.8). The discrepancies could be caused by: 1) the plasmaspheric TEC that is not accounted for in the IRI integration; 2) differential code bias of GNSS receivers.

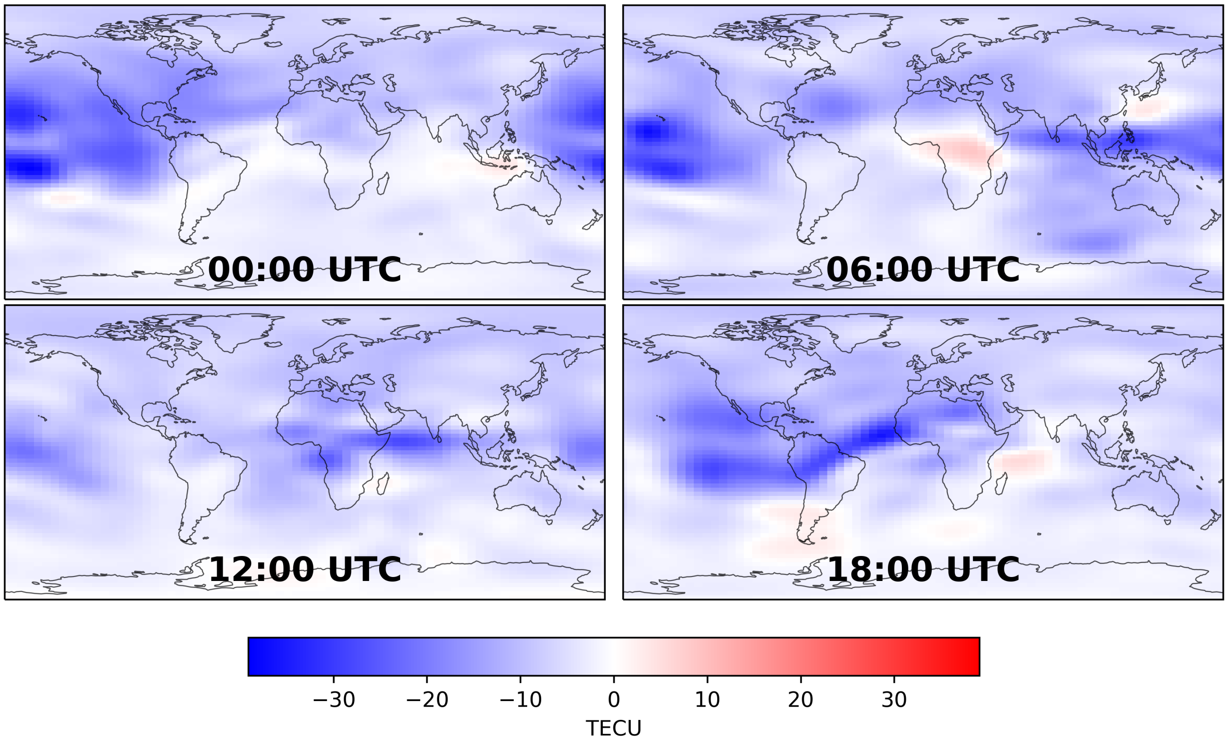

Figure 5.8: Difference of CDDIS and IRI global TEC maps shown in Fig. 5.7. The residuals between the CDDIS data and the IRI model reach up to ~ 35 TECU near the equator and around ~ 10 TECU anywhere else. The discrepancies are likely caused by: 1) the plasmaspheric TEC that is not accounted for in the IRI integration; 2) differential code bias of GNSS receivers.

effects for the 21cm experiments. Ideally, such calculations would be compared to actual ionosphere measurements during instrument deployments.

Still, the developed model can be used in simulations of the antenna temperature to study the dynamical ionosphere's effect on an observed antenna temperature. As will be shown in the next section, the ionospheric effects on simulated antenna temperatures are relatively small and can be removed with a `LINLOG` model of moderate complexity. A more in-depth analysis of possible uncertainties of simulated antenna temperatures (including integration over time) is left for future work.

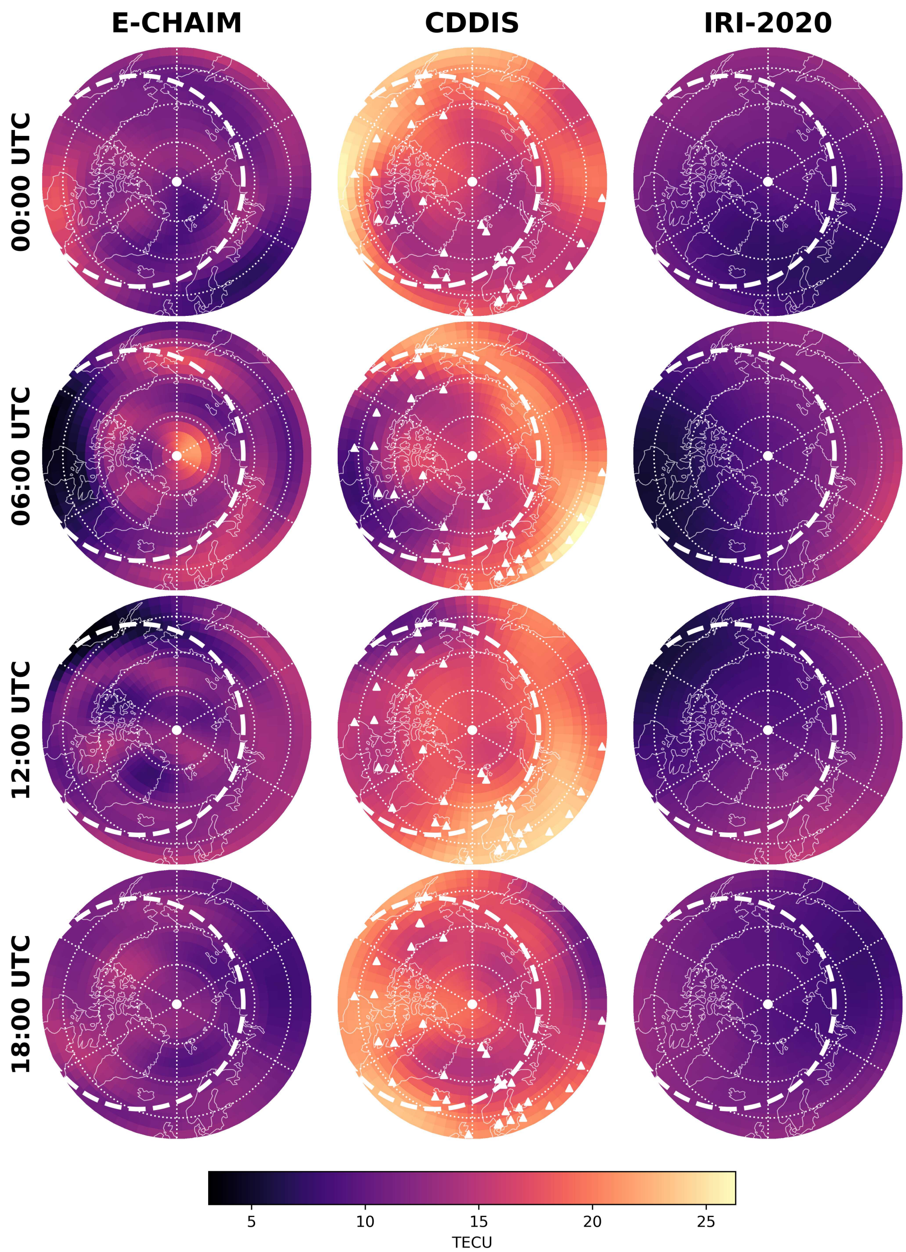

Figure 5.9: Comparison of integrated TEC from E-CHAIM (left) and IRI (right) models with CDDIS data in the polar region. The plot starts at the North pole in the centre and extents to 55 deg latitude. Simulation was performed for 16 July, 2022. The white dashed circle outlines the area of interest to the MIST instrument during the 2022 deployment in the Arctic. White triangles in the CDDIS plots represent GNSS receivers locations.Typical absolute differences between models and GNSS data are $\sim$ 10 TECU. The E-CHAIM model accounts for small scale structures in the polar cap and auroral region, which can be missed in the GNSS maps because of interpolation approach with lack of stations at high latitudes.

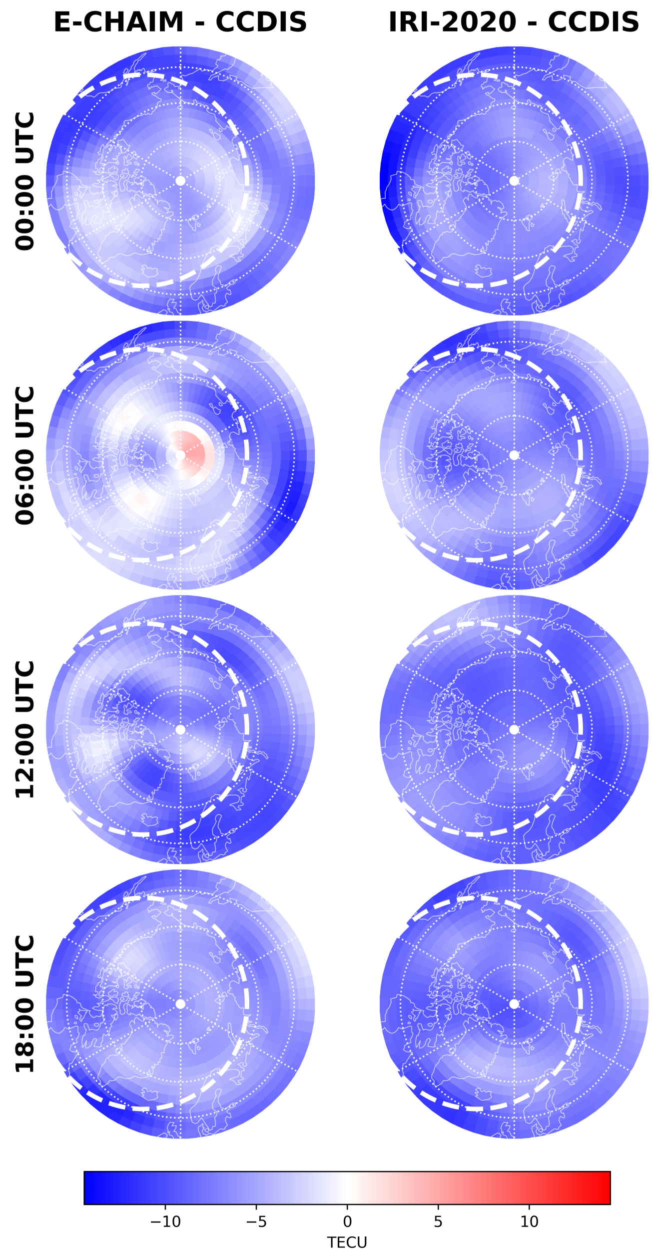

Figure 5.10: Residual maps of plots presented in Fig. 5.9. The plot starts at the North pole in the centre and extents to 55 deg latitude. Simulation was performed for 16 July, 2022. The white dashed circle outlines the area of interest to the MIST instrument during the 2022 deployment in the Arctic. Typical absolute differences between models and GNSS data are ~ 10 TECU. The E-CHAIM model accounts for small scale structures in the polar cap and auroral region, which can be missed in the GNSS maps because of interpolation approach with lack of stations at high latitudes.

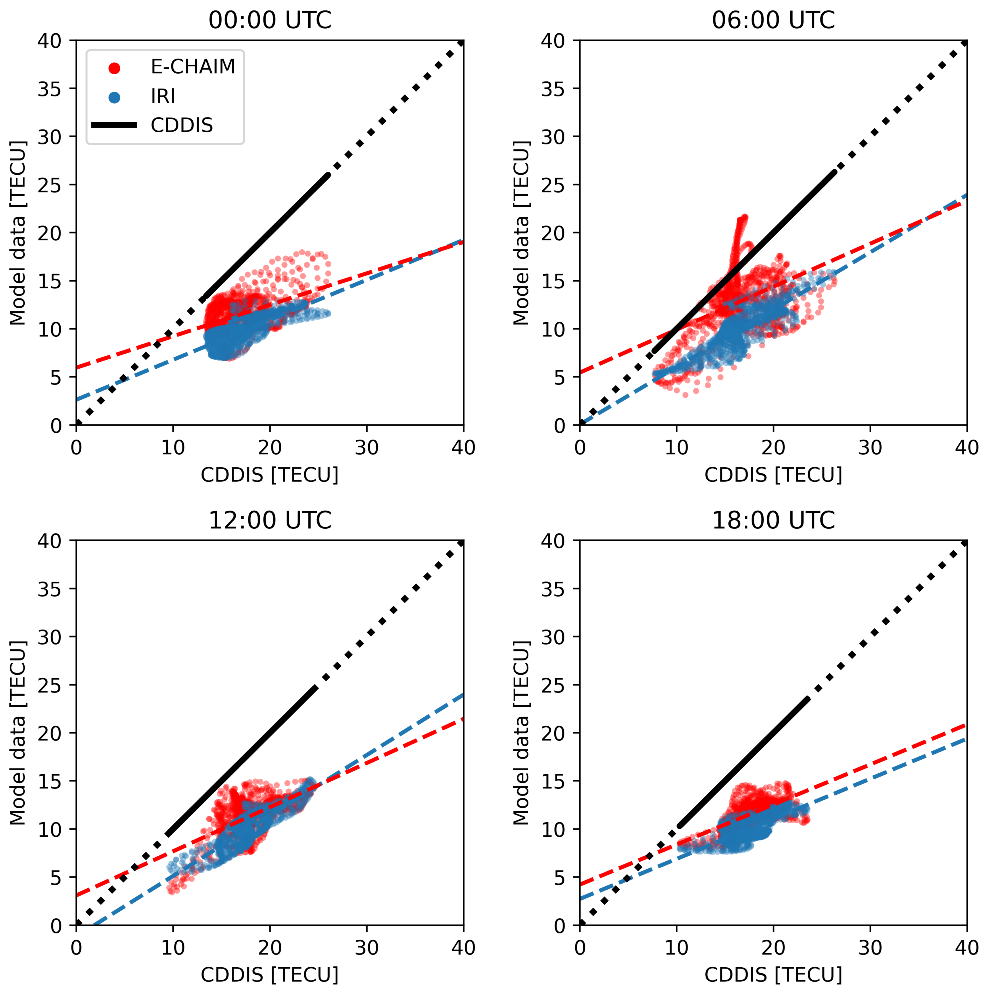

Figure 5.11: Correlation plots of data presented in Fig. 5.9 showing calculated TEC data (y-axis) versus CDDIS data at corresponding coordinates (x-axis). Coloured dashed lines represent the fitted polynomial $a \cdot x + b$ to the data of corresponding colour.

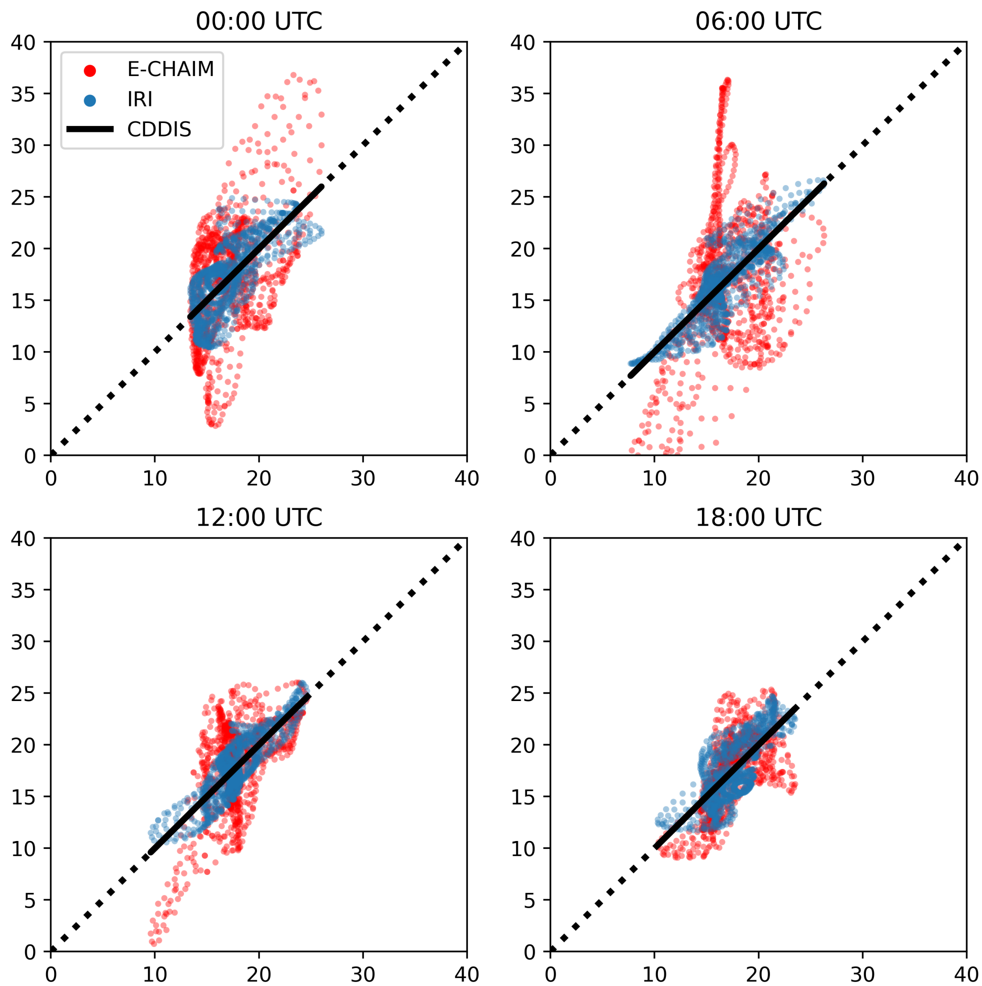

Figure 5.12: TEC data from E-CHAIM and IRI presented in Fig. 5.11 after applying correction $\mathrm{TEC}^* = (\mathrm{TEC} - b)/a$. The occasional large deviations in the E-CHAIM data are likely because of the incapability of GNSS maps to track small-scale structures at very high latitudes due to a lack of observational stations.

5.4 Exploring Ionospheric Effects on Simulated Antenna Temperature

The ionosphere's effects are the most interesting to study in the context of antenna temperature simulations. This kind of simulation directly shows how the ionosphere impacts the measurements. The examples of `dionpy`'s dependence on time will be shown in the next section; here we will focus on studying ionospheric effects for a specific time (July 16, 2022) and location (MARS). The simulation was performed by evaluating Eq. 2.1 with the foreground model based on observations and a simulated antenna beam for the MIST instrument. We will then fit a `LINLOG` model (Eq. 2.2) with different polynomial order to the simulated antenna temperature trying to see what ionosphere signals survive the foreground removal process.

Since the MIST experiment does not use a ground plane, so the soil is an integral part of the antenna. The work on accurate simulations of the MIST antenna beam is still ongoing. Here I use a nominal model of MIST antenna beam that was simulated using Feko[2] software using a soil model consisting of a single layer with nominal values of permittivity and conductivity (which are functions of position). The examples of the normalized beam are shown in Fig. 5.13.

We use the Low Frequency Sky Model (LFSM)[3] as a model of the galactic foreground at the frequencies of interest. The LFSM was built on top of several observational maps of galactic emission and provides data in the form of HEALPix map for a requested frequency with resolution `NSIDE`=64, which roughly corresponds to pixel area 0.9 sq. degree (Dowell et al., 2017). The LFSM evaluation at frequency 40 MHz is shown in Fig. 5.14. Fig. 5.15 features the LFSM at 40 MHz as visible from the instrument location during the MARS deployment.

The frequency-dependent LFSM (which will be referred to as "full LFSM"), which was used for simulation of antenna temperature by convolving it with the MIST antenna

[2] https://altair.com/feko
[3] http://lda10g.alliance.unm.edu/LWA1LowFrequencySkySurvey/

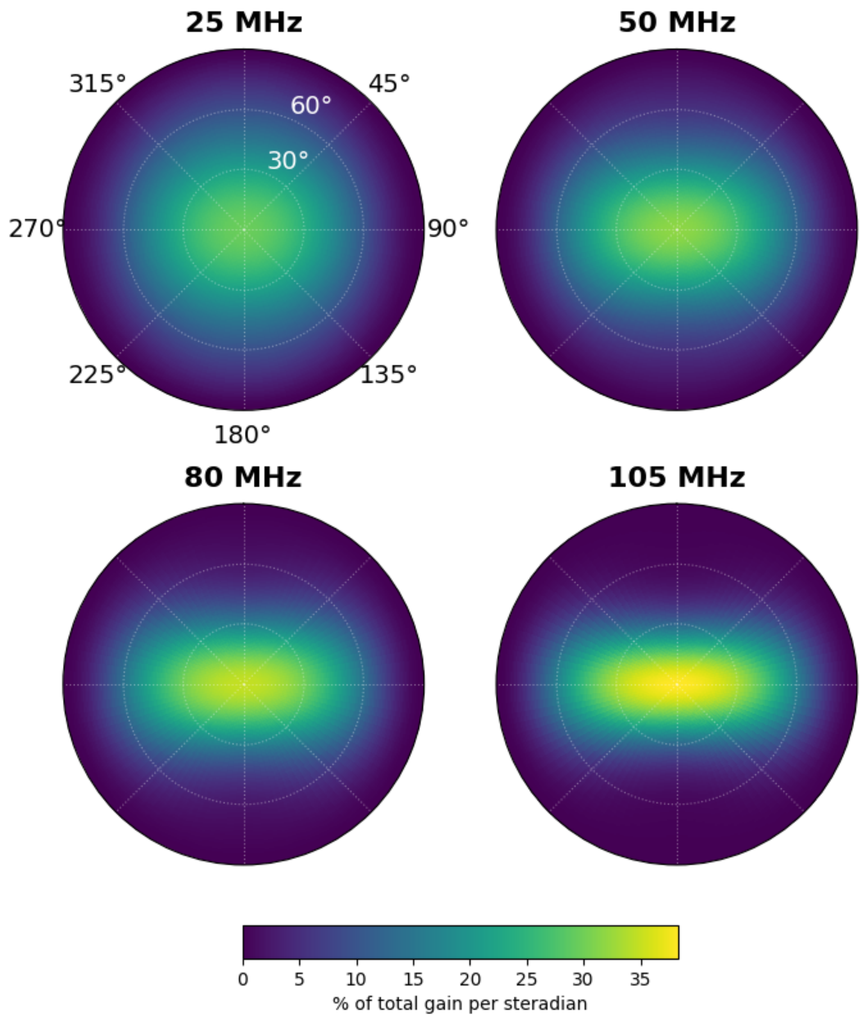

Figure 5.13: Simulated MIST beam for different frequencies using the soil model consisting of a single layer with nominal values of permittivity and conductivity. The effect of beam chromaticity can be clearly noticed between different panels that show the simulated beam at 25, 50, 80 and 105 MHz.

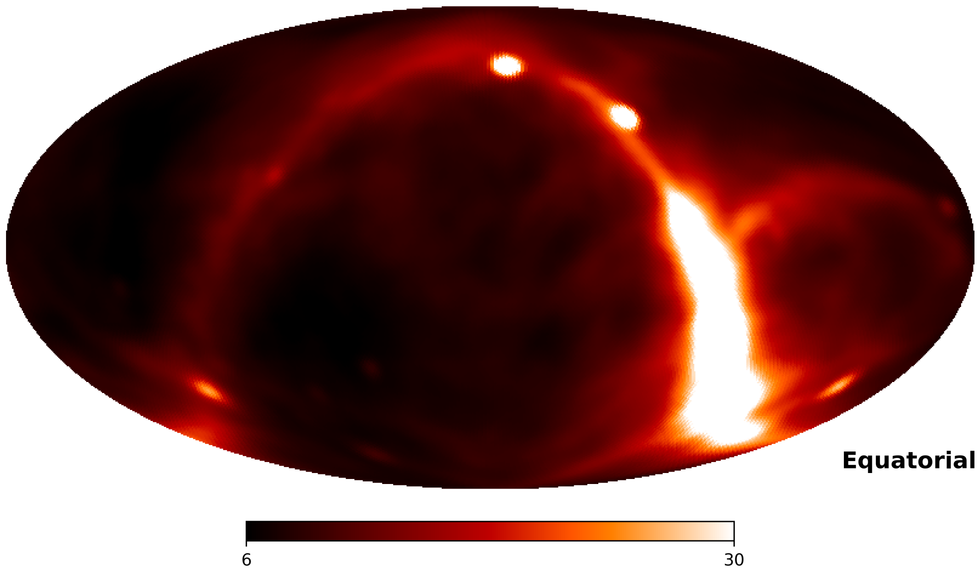

Figure 5.14: LFSM model (Dowell et al., 2017) evaluated at 40 MHz. The model is used in simulations of antenna temperature. The visible part of the foreground depends on the geographical location of the instrument and the time of observation. The examples of the visible foreground for the recent MIST deployment at MARS are shown in Fig. 5.15. The colour on the image maps the sky temperature in the thousands of Kelvin (kK).

beam, produced unexpected residuals during the `LINLOG` model fitting process (see Fig. 5.16). We think these sharp residuals are unphysical and likely result from the merging of different sets of observational maps in LFSM, since the other component of convolution - the antenna beam is smoothly varying with frequency. Instead, we evaluate the LFSM at 100 MHz and extrapolate it to other frequencies assuming a perfect power law with index -2.38 (this model will be referred to as "rescaled LFSM"). The β index was obtained by fitting a power law to the full LFSM evaluated at a range of frequencies ($25-125$ MHz) at one specific sky coordinate. The resulting β does not depend on the sky coordinate chosen for the fitting. The full LFSM (for one specific coordinate) and the rescaled LFSM are shown in Fig. 5.17. The rescaled LFSM will be used for all following antenna temperature simulations in this thesis.

The initial result of fitting different models to the simulated T_a is shown in Fig. 5.18. The first panel show the difference between the T_a and a fitted power law. The obtained

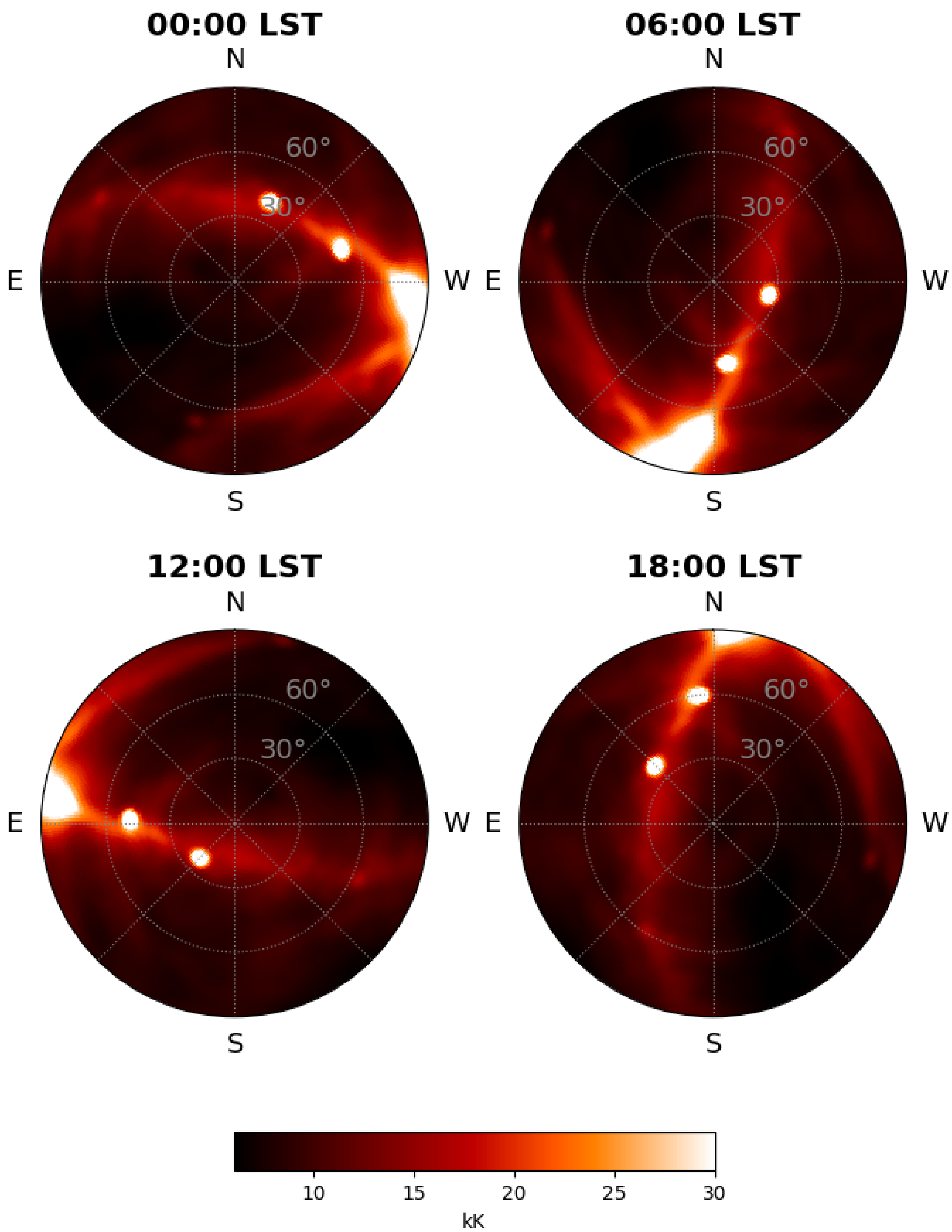

Figure 5.15: Visible foreground emission during the first day of the MIST deployment at MARS, simulated with LFSM at 40 MHz for 0 h, 6 h, 12 h and 18 h LST (corresponding to the figure panels in order). The radial axis corresponds to the zenith angle, and the angular axis corresponds to the azimuth of observation. The colour on the image maps sky temperature in the thousands of Kelvin (kK).

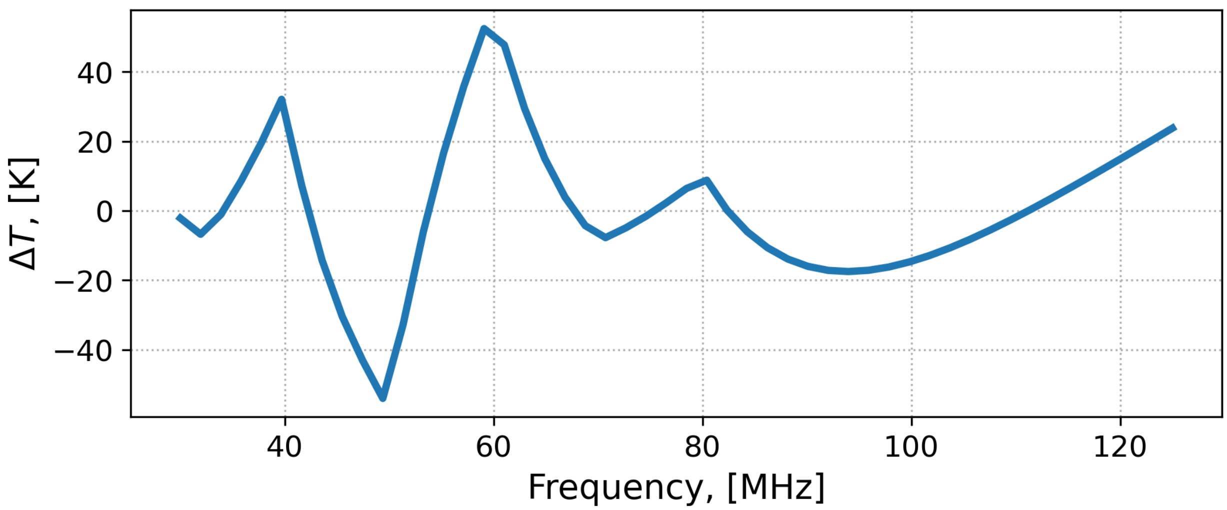

Figure 5.16: Residuals when fitting a LINLOG model to the frequency-dependent LFSM. The sky maps are observed with the MIST beam before LINLOG fitting. The sharp residuals look unphysical, so we instead adopt a perfect power law.

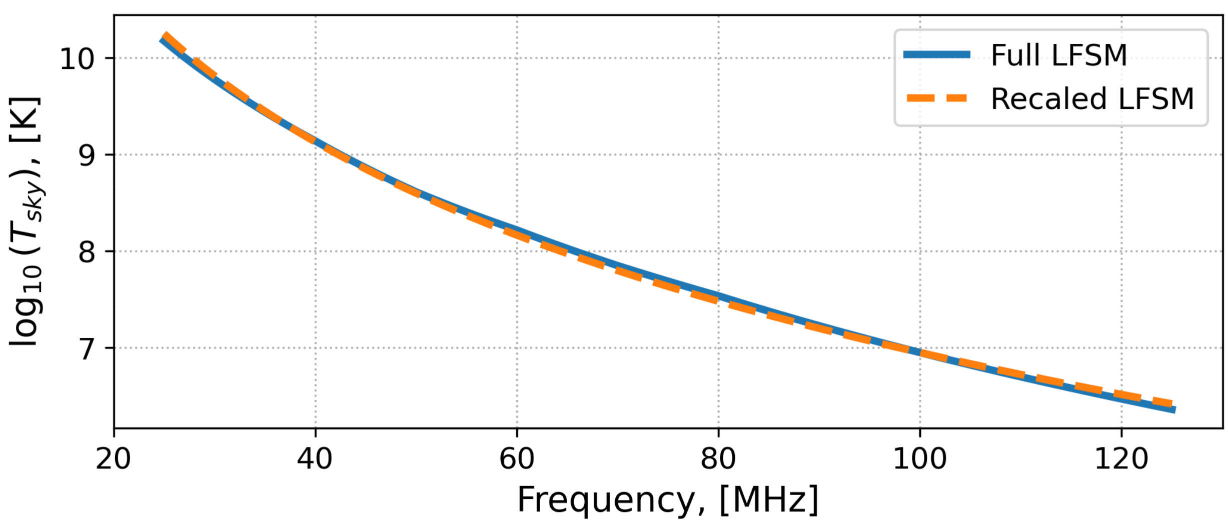

Figure 5.17: Solid blue curve represent the frequency dependent LFSM model (referred to as "full LFSM") at one particular sky coordinate. A perfect power law was fitted to the blue curve, yielding the spectral index $\beta = -2.38$. The resulting β does not depend on the sky coordinate chosen for fitting. The dashed orange curve represents the LFSM evaluated at 100 MHz and extrapolated to other frequencies using $\beta = -2.38$ (referred to as "rescaled LFSM"). The perfect power law model (orange curve) is used instead of LFSM in simulations in this work because of unphysical residuals produced by the full LFSM (see Fig. 5.16).

difference has an order of magnitude larger than the expected global 21cm signal, resulting from the antenna beam chromaticity, previously demonstrated in Fig. 5.13.

The second panel in Fig. 5.18 demonstrates the total chromatic impact of the ionosphere on the simulated T_a, which was subtracted from the T_a^* (the antenna temperature that includes all ionospheric effects). The ionosphere's effect is much higher than the expected 21cm signal; luckily, the former also has a predictable spectral behaviour, making it possible to model and remove (as shown in the following plots).

The third panel in Fig. 5.18 shows the difference between the T_a and a fitted high-order `LINLOG` model (specifically - fourth-order) in the $50-105$ MHz range. The obtained residuals have expected spectral behaviour (with three local extrema). At the same time, the residuals are still big - order of 0.1 K, which is comparable to the 21cm signal. This is because, generally, residuals depend on the frequency range used for fitting - the narrower frequency band is, the smaller are residuals. For this simulation we selected considerably broad range. For comparison, using slightly shorter frequency range - $60 - 100$ MHz produces residuals $\sim$ 0.05 K for the fitted `LINLOG` of the fourth order. In the same frequency range, as used for simulations ($50 - 105$ MHz), the fifth-order polynomial produces smaller residuals ($\sim$ 0.02 K), but at that level the numerical artifacts of fitting become visible.

To explore the impact of the ionosphere, our next step will involve carrying out the following procedure:

1. fit the `LINLOG` model to the T_a simulated without ionospheric effects and calculate residuals;

2. fit the `LINLOG` model to the T_a simulated including ionospheric absorption / refraction / emission / all effects and calculate residuals;

3. calculate the difference between both residuals. This will show how much the ionosphere impacts the result of the fitting. We expect that the higher order of polynomials in the `LINLOG` model will lead to a smaller difference between residuals.

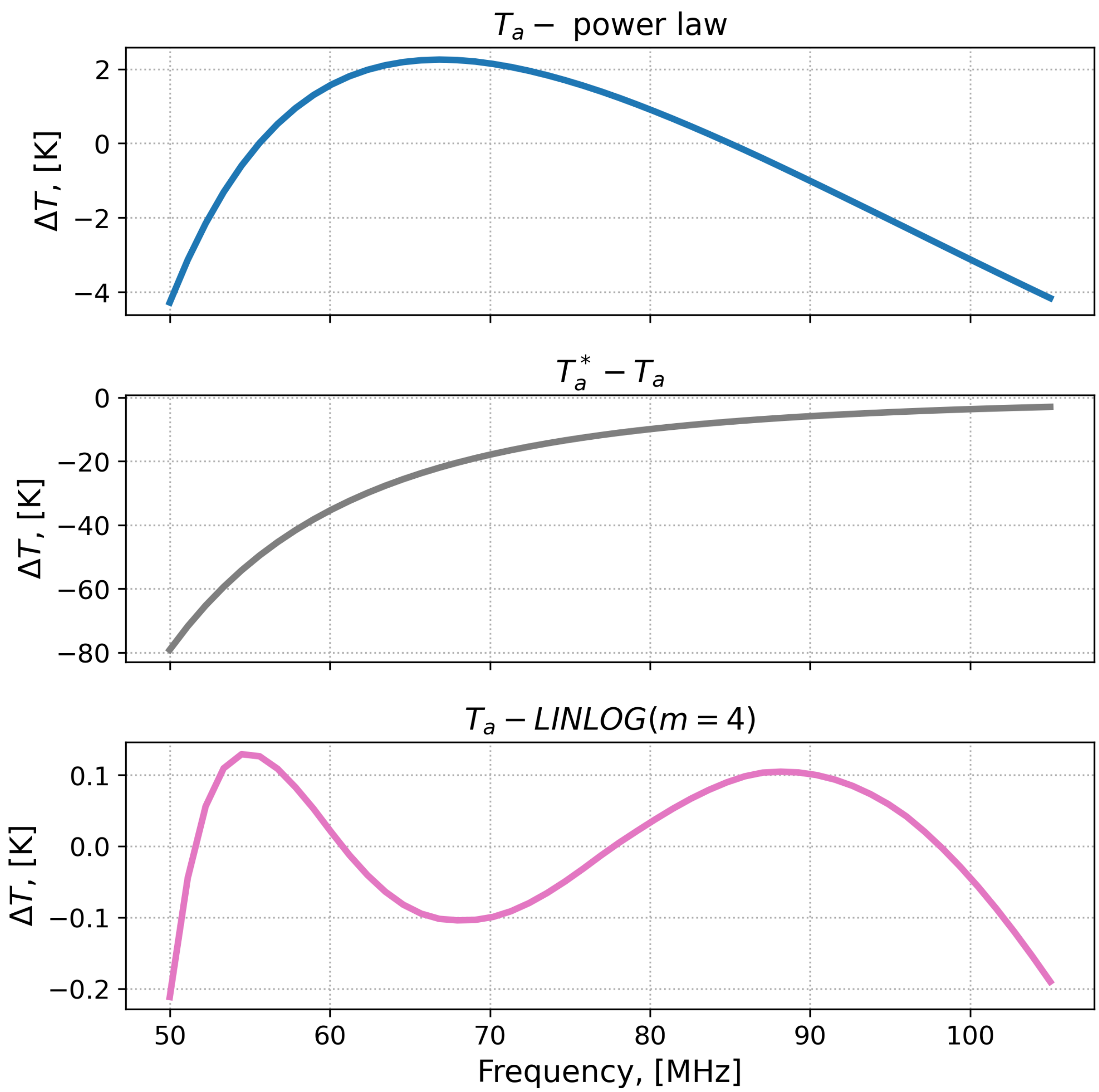

Figure 5.18: Residuals of simulated antenna temperature with different models. **Panel 1** shows residuals of T_a (simulated with the rescaled LFSM and and the MIST beam) and a power law, fitted to simulated T_a. These residuals demonstrate the beam chromaticity effect on the convolution of the beam and sky models. **Panel 2** demonstrates the total impact of ionospheric effects on the simulated antenna temperature. The plot shows the difference of T_a^* (includes refraction, absorption and emission) and T_a (antenna temperature simulated without ionospheric effects). **Panel 3** shows residuals of the simulated antenna temperature (without ionospheric effects) and the fitted `LINLOG` model of the fourth order.

Fig. 5.19 shows the difference of residuals that includes absorption only. The first, second and third panels show the difference for the fitted `LINLOG` model of the third, fourth and fifth order correspondingly. Assuming the amplitude of the global 21cm signal to be ~ 0.25 K (see Fig. 1.4), it will take at least a fourth order of `LINLOG` model to remove the effects of the absorption with a $\sim 10\%$ error.

Fig. 5.20 shows a similar procedure applied for the refraction effect. The effect of refraction has a smaller impact on the antenna temperature than absorption and therefore needs a lower-order model to be removed. The first panel in Fig. 5.20 shows that the difference in residuals for the `LINLOG` model of the second order is already much smaller than the approximate 21cm signal amplitude (the refraction effect is removed with a $\sim 2\%$ error).

The impact of the D-layer emission and the difference in residuals for T_a with and without included emission is shown in Fig. 5.21. Although the emission's amplitude has an order of magnitude of the expected 21cm signal, this effect is easily removed even with the second-order `LINLOG` model. As a side note, one may notice a considerable difference between the emission in Fig. 5.21 and the one shown earlier in Fig. 5.2. The main reason for that is the difference in time chosen for simulations. The simulation from Fig. 5.2 was performed at 4 pm in local time when the position of the Sun was higher compared to 5.21 (midnight), which causes more absorption and, therefore, higher emission. The simulations were also performed for different locations separated by ~ 40 degrees in latitude, which also contributes to the difference.

Finally, the combined effect of absorption, refraction and emission is shown in Fig. 5.22. Since the absorption effect dominates, the model of combined effects, in general, follows the behaviour of the absorption, previously shown in Fig. 5.19: at least a fourth-order of the `LINLOG` model is needed to remove all ionospheric effects with a $\sim 10\%$ error in the current simulation of antenna temperature.

It is important to notice that the simulation performed in this section studies only the effect of the inhomogeneous model of the ionosphere on the simulated antenna temperature.

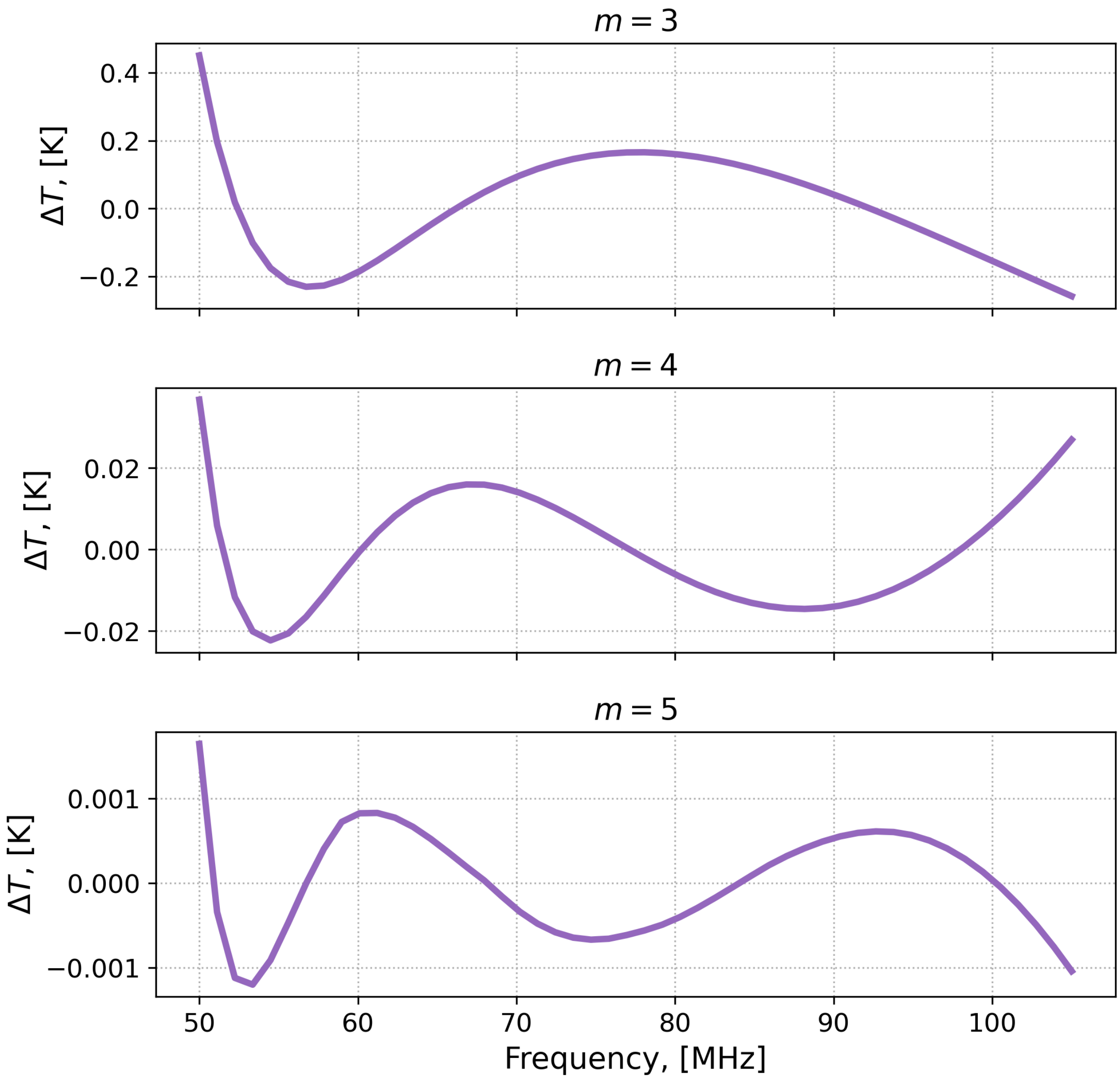

Figure 5.19: The efficiency of `LINLOG` in removing the effect of **absorption** in simulated antenna temperature. First, the T_a and T_a^* were calculated as a convolution of models of the foreground and antenna beam. Then a `LINLOG` models of an n-th order was fitted to both simulated temperatures, producing residuals similar to that shown in Panel 3 of Fig. 5.18. Finally, the difference of both residuals was calculated and presented in this plot. The calculations in the first, second and third panels used the `LINLOG` model of the third, fourth and fifth orders correspondingly. Assuming the expected 21cm signal amplitude ~ 0.25 K (see Fig. 1.5), at least a **fourth**-order polynomial is necessary to remove the absorption effect with a $\sim 10\%$ error.

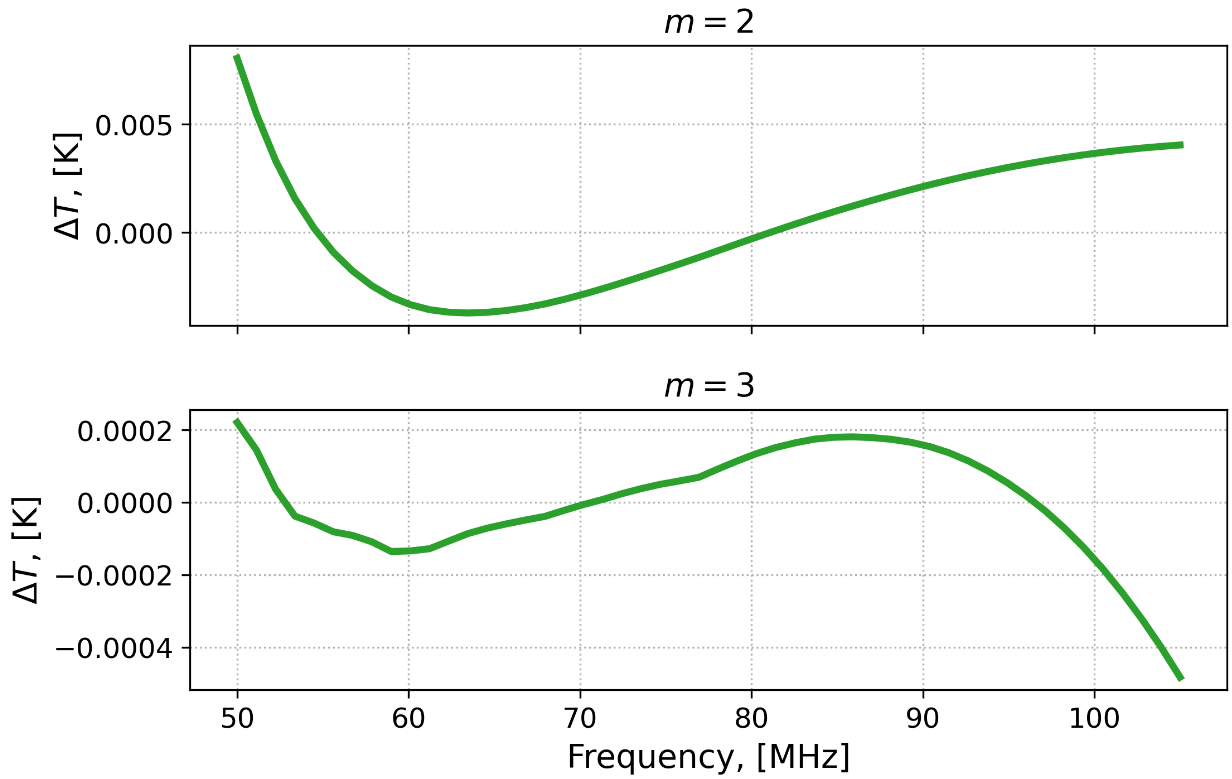

Figure 5.20: The efficiency of `LINLOG` in removing the effect of **refraction** in simulated antenna temperature. This plot repeats the procedure described in Fig. 5.19. The calculations in the first and second panels used the `LINLOG` model of the second and third orders correspondingly. Assuming the expected 21cm signal amplitude ~ 0.25 K (see Fig. 1.5), at least a **second**-order polynomial is necessary to remove the absorption effect with a $\sim 2\%$ error.

Studying dynamic effects (on a day, month and other scales) is left for future work. The comparison of inhomogeneous and homogeneous ionosphere models is also planned for the future.

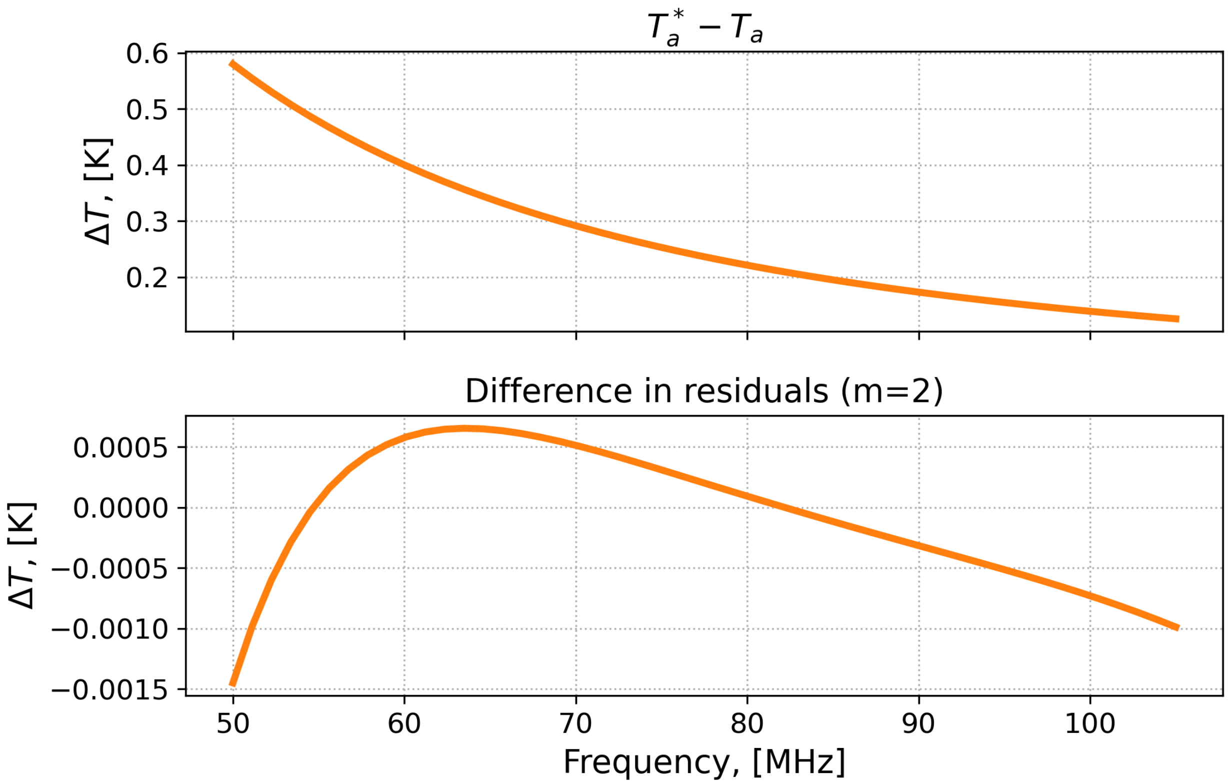

Figure 5.21: The efficiency of `LINLOG` in removing the effect of **emission** in simulated antenna temperature. The **first panel** shows the difference between simulated T_a^* that includes ionospheric emission and T_a that was simulated without included emission. The **second panel** repeats the procedure described in Fig. 5.19 for the `LINLOG` model of the second order. This plot shows that the effect of emission is negligible even when fitting low-order polynomials.

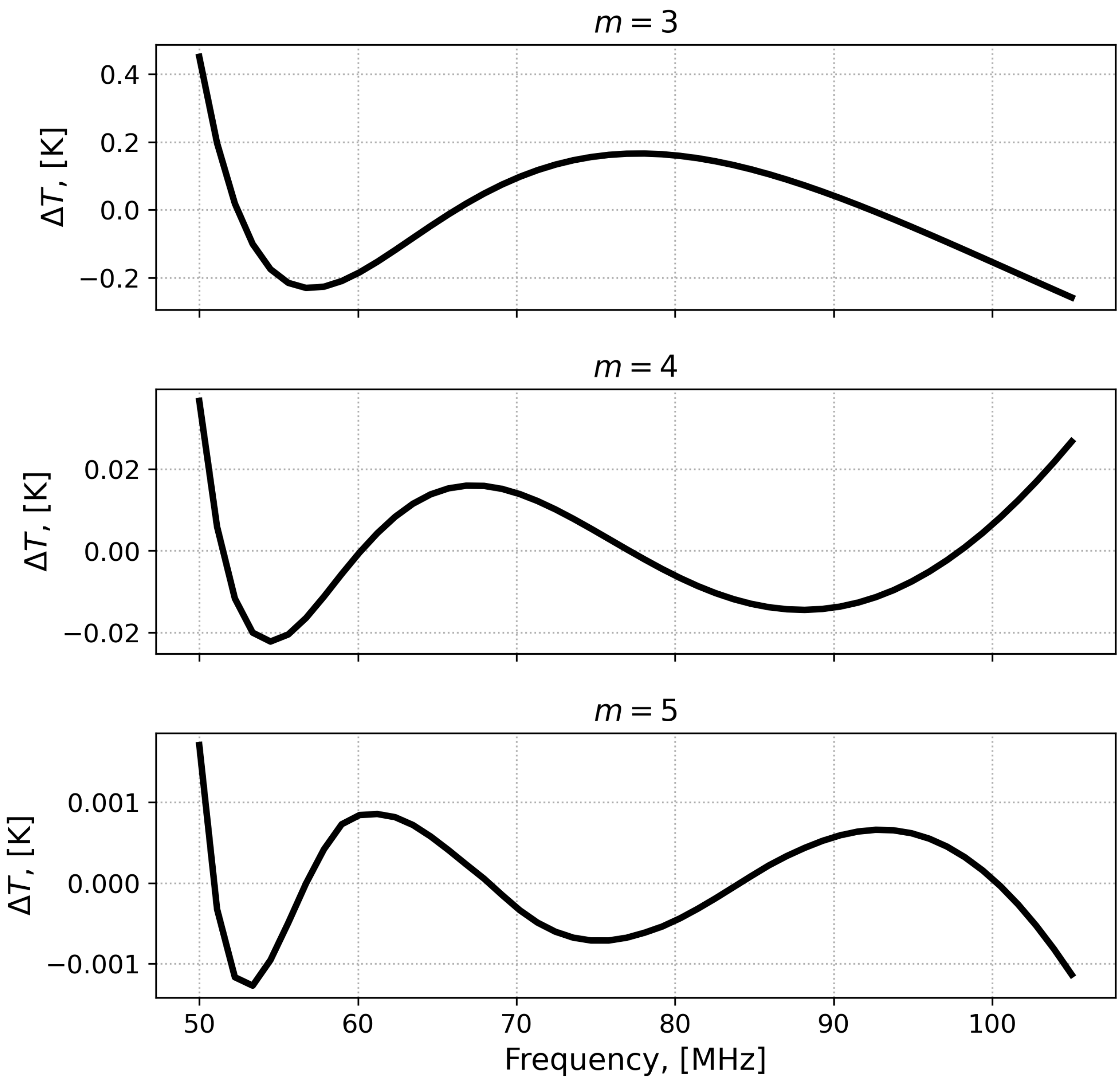

Figure 5.22: The efficiency of `LINLOG` in removing the effect of **all effects** of the ionosphere in simulated antenna temperature. This plot repeats the procedure described in Fig. 5.19. The calculations in the first, second and third panels used the `LINLOG` model of the third, fourth and fifth orders correspondingly. Assuming the expected 21cm signal amplitude ~ 0.25 K (see Fig. 1.5), at least the **fourth**-order polynomial is necessary to remove the absorption effect with a $\sim 10\%$ error.

5.5 Simulations for the MIST Deployment in Arctic and Comparison with Data

In the first place, `dionpy` was created to become a model of the dynamic ionosphere. The additional (time) dimension in the model opens many new possibilities for antenna temperature simulations. While more in-depth studies of temporal variation of the ionosphere are left for the future, this section presents an example simulation of ionospheric effects for the MIST deployment at MARS in 2022. For comparison, I also show the binned within defined LST blocks, preliminary MIST data from the deployment.

Fig. 5.23 shows the first 14 hours of observation for different deployment sites in 2022. Since the accurate calibration pipeline is still in development, only initial calibration was applied in the form:

$$T_a = T_{NS} \frac{P_a - P_L}{P_{L+NS} - P_L} + T_L, \tag{5.1}$$

where P_a, P_L and P_{L+NS} are PSDs from the antenna, load and load + noise source correspondingly; T_L and T_{NS} represent assumption for the noise temperatures of the load and the noise source respectively (in this work $T_L = 2000$ K and $T_{NS} = 300$ K are assumed); T_a, P_a, P_L and P_{L+NS} are functions of time and frequency (Monsalve et al., 2017). Easy to notice (especially in the 85-105 MHz range) that the MARS location has a much cleaner RFI environment compared to other sites.

The data from the MARS deployment will be used for comparison with ionospheric effects in this section. To directly compare spectra from different days, we apply a binning procedure in predefined LST blocks with a duration of 2 minutes within the same day. Fig. 5.24 shows the LST occupancy by the MIST data during the 13 days of observation at the MARS deployment site (lower panel) and the number of days available for each LST block.

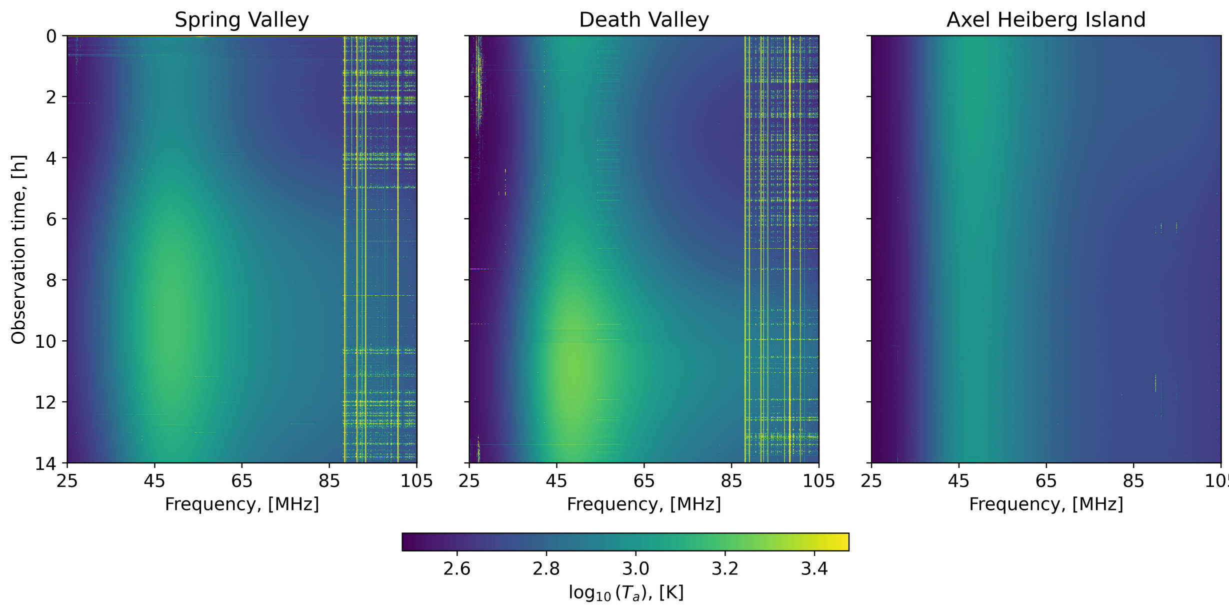

Figure 5.23: Comparison of the first 14 hours of MIST observation from different deployment sites. Only initial calibration (Eq. 5.1) was applied. The three panes in the picture correspond to the Spring Valley (California, USA), Death Valley (Nevada, USA) and MARS (Nunavut, Canada) in order. The MARS location shows the significantly lower RFI presence in data, especially in the 85-105 MHz range.

Since the calibration of the recorded data is incomplete, comparing the absolute temperature values is unreasonable. Instead, we will compare the relative change in the T_a between the actual data and simulations of the ionosphere.

For illustration purposes, we first smooth the binned spectra (by convolving it with the Gaussian kernel) and then apply the singular value decomposition (SVD) algorithm (Golub and Van Loan, 2013). We then reconstruct the spectra using only the first two SVD modes to highlight the large-scale variation of T_a with frequency, discarding the large portion of noise. The result is presented in Fig. 5.25 for LST=12 h, where the spectrum of the second observational day (the first day with full LST coverage) is subtracted from others as a reference point. In the plot, we can notice some evolution of the T_a over time, especially around 55 MHz.

For the simulations of the ionosphere during the MARS deployment the `IonModel` class (see Sec. 4.4) was used with 15-minute time resolution and IRI as an ionosphere

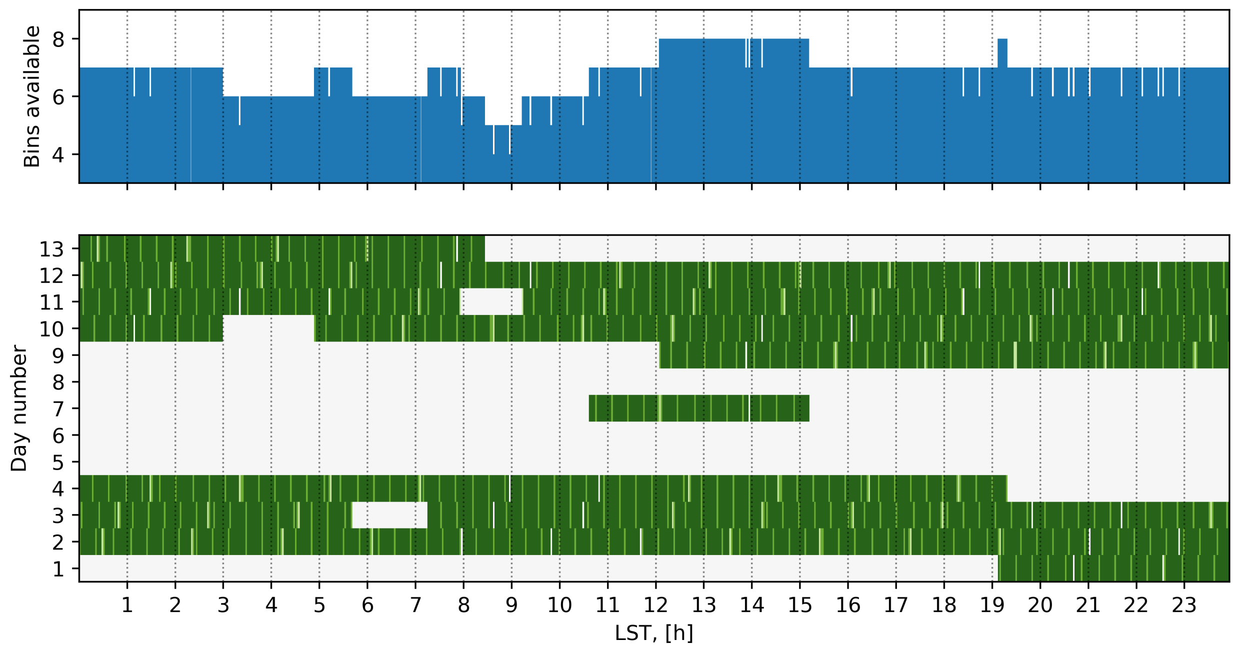

Figure 5.24: LST occupancy by the MIST data during the 13 days of observation at the MARS deployment site. The lower panel shows all available data averaged within LST blocks with a 2-minute duration. The most saturated green colour corresponds to bins with the maximum number of spectra available (specifically, three spectra rows, since MIST records data with interval ~ 40 s); lighter green colours correspond to 1-2 spectra rows, which means that within that block the instrument switched to recording the calibration data; white blocks reflect an absence of the data. The upper panel shows the total number of days available for each LST block.

model. The result of the simulation is shown in Fig. 5.26 in the decibel scale. As the plot shows, ionospheric absorption at all simulated frequencies decreases with time.

Fig. 5.27 shows the evolution of absorption as a percentage of the total temperature. For the simulation convolved with MIST antenna beam (solid blue curve), the total change in absorption at 30 MHz is around 1% over 13 days. Compared to Fig. 5.25, where relative changes in temperature at 30 MHz can reach 1% only within one day (for instance, day 10 and 11), it is clear that the effect of the ionosphere cannot be found in the observational data on the current stage of calibration. The visible variation in the observed temperature

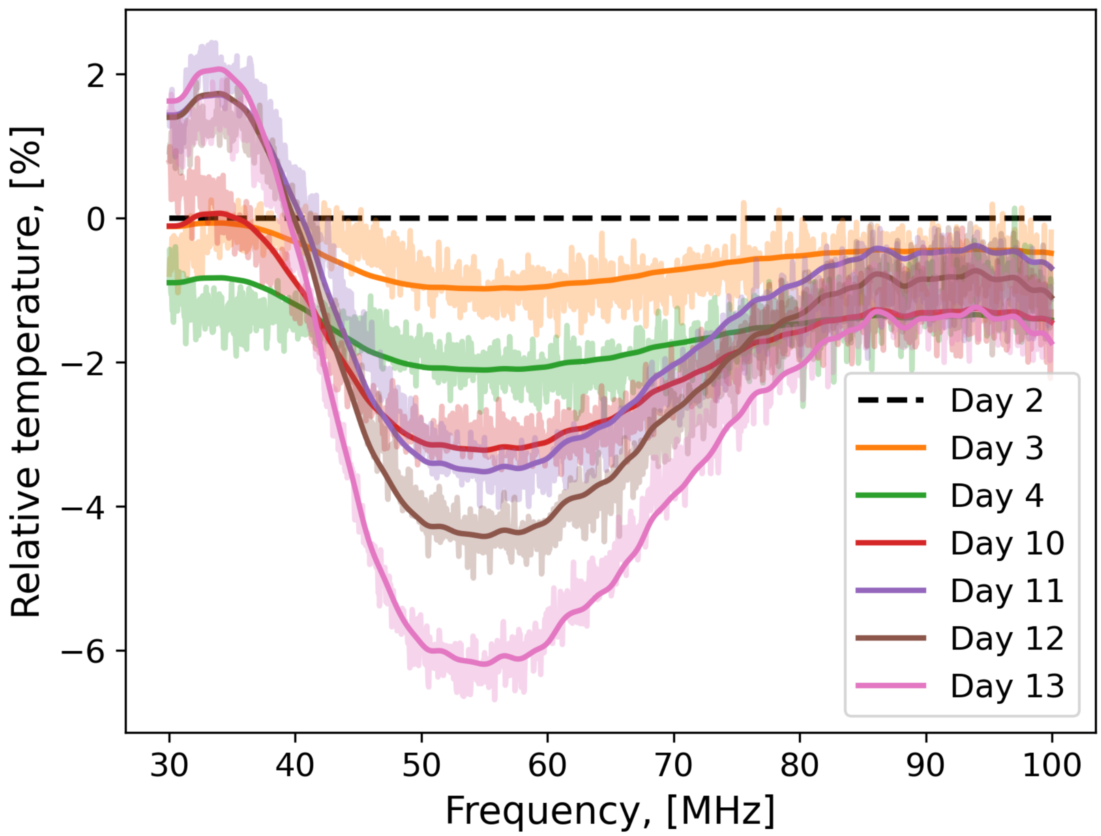

Figure 5.25: MIST data from MARS deployment - binned within 2 minute LST blocks, smoothed and reconstructed from an SVD using the first two modes. The lighter-coloured lines represent the unfiltered data before SVD applied. The plot corresponds to LST=12 h.

could be related to other time-dependent effects, for example - ambient temperature or soil reflection properties.

The result of the simulation for the refraction effect is shown in Fig. 5.28. The relative impact of the refraction on the simulated antenna temperature is smaller than 0.025% even at low frequencies (30 MHz), while its variation during the observation time is smaller than 0.01%. The simulated effect of refraction is negligible compared to absorption and definitely cannot be noticed in the observed data on the current calibration stage.

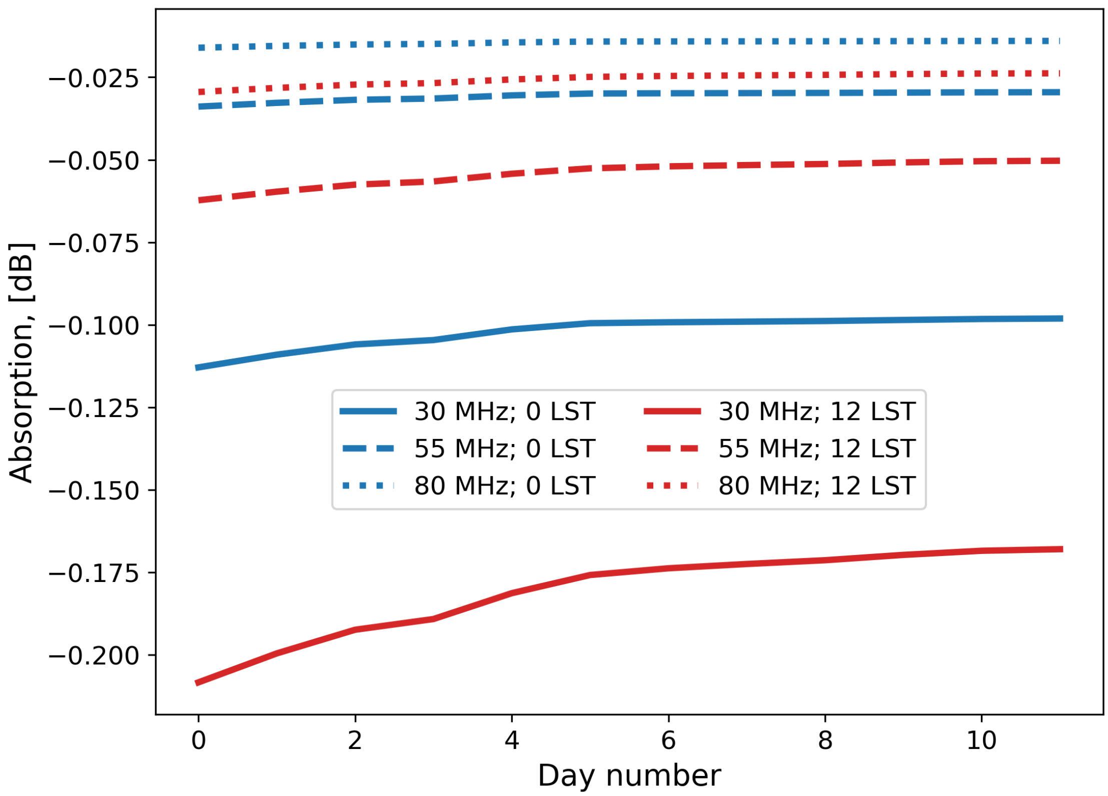

Figure 5.26: Simulated absorption during MIST deployment at MARS, starting on July 16, 2022. The absorption map was convolved with the model of MIST antenna beam, described in Sec. 5.4. In the plot, blue represents simulations for 0 h LST, while simulations for 12 h LST are painted red. The solid, dashed and dotted line styles represent 30, 55 and 80 MHz simulations, respectively.

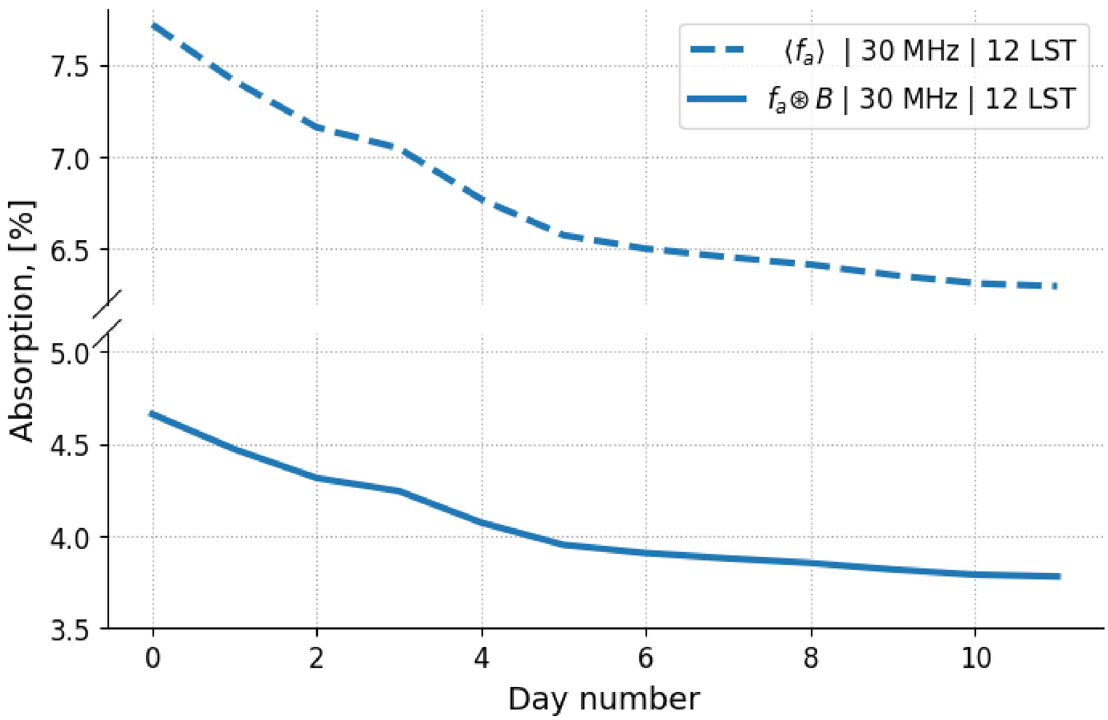

Figure 5.27: Simulated absorption during MIST deployment at MARS at 30 MHz and 12 h LST. The dashed blue curve shows absorption averaged over the whole sky, which can also be interpreted as a convolution with a uniform antenna beam. The solid blue curve shows the absorption convolved with the model of MIST antenna beam, described in Sec. 5.4. The latter simulations show considerably lower total absorption since the MIST instrument has lower directivity towards low elevations, where the absorption is the highest.

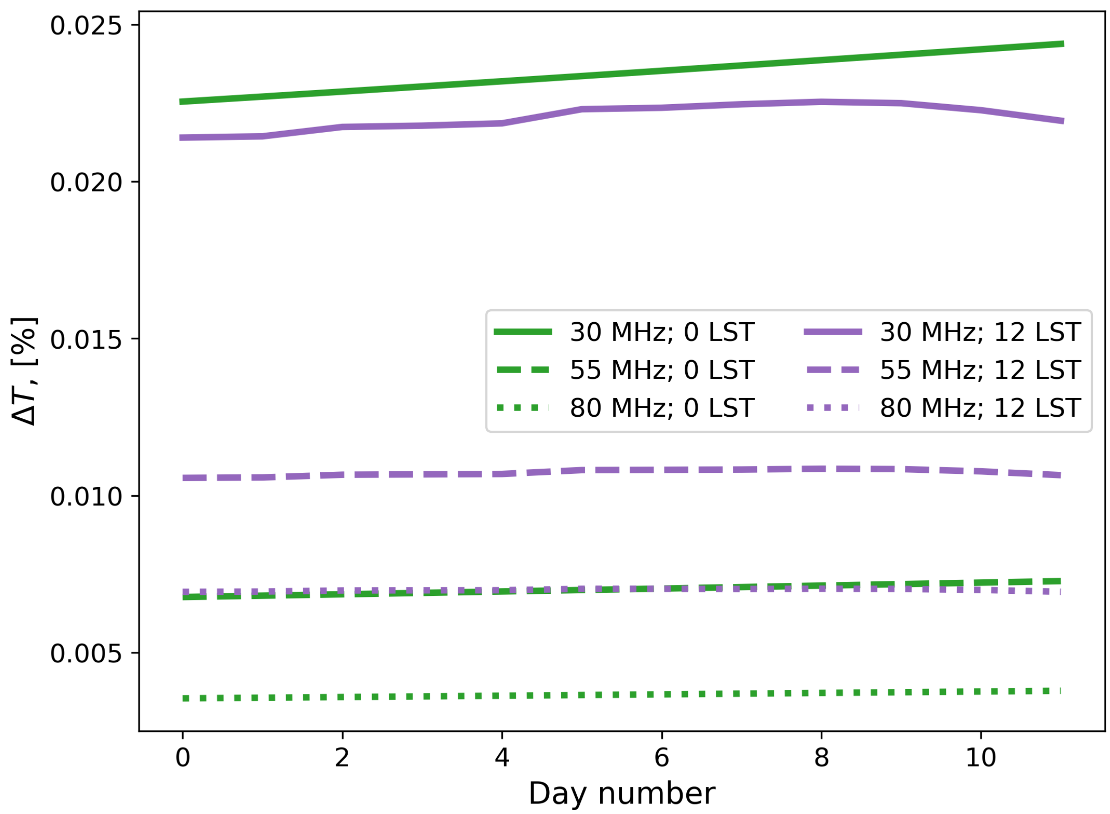

Figure 5.28: Simulated refraction during MIST deployment at MARS. The map of refraction was applied during the LFSM evaluation convolved with the model of MIST antenna beam, described in Sec. 5.4. The vertical axis shows the per cent temperature change compared to the antenna temperature simulated without applying the refraction effect. In the plot, the green colour represents simulations for 0 h LST, while simulations for 12 h LST are painted purple. The solid, dashed and dotted line styles represent 30, 55 and 80 MHz simulations, respectively.

Chapter 6

Discussion and Future Work

6.1 Model Overview

In this thesis, I introduced and described the dynamic model of the ionosphere based on IRI. The model uses electron density profiles generated by IRI to simulate the propagation of radio waves through the ionosphere. The ionospheric corruption effects taken into account include collisional absorption (D-layer), thermal emission (D-layer) and refraction (F-layer). The model also allows using the E-CHAIM instead IRI, which is expected to produce more accurate electron density profiles at high ($\gtrsim 55°$) latitudes.

The created model was implemented in Python programming language and published in open access as an installable Python package `dionpy`. In the process of `dionpy` creation, it was necessary to develop custom Python wrappers for IRI and E-CHAIM models since they both were implemented in different languages. The created wrappers were published in the form of separate packages as well (`iricore` for IRI and `echaim` for E-CHAIM). Although the primary purpose of `iricore` was to be used in `dionpy`, several other research groups (such as Canadian Hydrogen Intensity Mapping Experiment (CHIME)[1]) have already expressed interest in using the `iricore` package for ionosphere modelling.

[1] https://chime-experiment.ca/en

Since simulations of dynamic inhomogeneous ionosphere require a large amount of computations, the implementation was heavily focused on performance optimization. As mentioned in Sec.4.3.1, the created `iricore` package is ~ 100 times faster than the previously existing IRI Python wrapper. The `dionpy` also provides an "out-of-the-box" possibility for high-level parallel computations.

The `dionpy` produces maps of attenuation, emission and refraction at any frequency. These maps can be calculated for any custom set of altitude and azimuth through pre-implemented interpolation algorithms, which makes it easier to match coordinate grids of gain or galaxy foreground. The interpolation between the models at different points in time is also implemented, allowing the generation of ionospheric models with custom time resolution. Instead of recalculation, generated models can be saved in HDF format and easily re-loaded on the need.

While developing the model, we assumed the negligibility of the magnetic field impact on the wave propagation (see Sec. 4.1.2); this assumption will necessarily be violated in a real ionospheric environment (specifically, in the D-layer), which can lead to a significant change in absorption. The investigation of the magnetic field effect is left for future work. In particular, we consider incorporating an existing model of global magnetic field parameters directly into `dionpy`. The possible models include International Geomagnetic Reference Field (IGRF)[2] (Alken et al., 2021) and World Magnetic Model (WMM)[3] (Chulliat et al., 2020).

6.2 Model Evaluation Results

The implemented dynamic model opens vast possibilities for exploring the ionospheric impact on the global 21cm experiments through simulations. Sec. 5.2 shows how `dionpy` compares to and extends the assumption of the homogeneous ionosphere, which was often used in previous simulations of global 21cm signal (Vedantham et al., 2014; Shen

[2]https://www.ncei.noaa.gov/products/international-geomagnetic-reference-field
[3]https://www.ncei.noaa.gov/products/world-magnetic-model

et al., 2021; Datta et al., 2014). The `dionpy` adds another level of complexity to the antenna temperature simulations while remaining quick in evaluation (the continuous ionospheric model can be generated within several minutes).

Some examples of model evaluation have been presented in this thesis. For instance, Sec. 5.4 describes an initial exploration of the ionospheric effect on simulated antenna temperature using the real antenna gain (from MIST experiment) and galaxy foreground (LFSM) models. The immediate result shows that one would need at least the fourth order of the fitted `LINLOG` model (Eq. 2.2) to remove the simulated effects of the ionosphere from residuals with a $\sim 10\%$ error. The Sec. 5.4 features ionospheric effects only for a specific date. With the dynamical model in hand, it would be interesting to conduct research on temporal variations of ionospheric influence, which is planned for future work. Apart from that, we also plan to repeat the simulation using other analytical and empirical foreground models.

In Sec. 5.5, I made a quick comparison of predicted ionospheric effects with the actual data observed during the MIST deployment at MARS site in Canadian Arctic in 2022. I performed simulations and demonstrated the expected behaviour of the ionosphere at different frequencies during the whole observational period. However, the magnitude of simulated effects turned out to be smaller than the temporal variations seen in the data; these variations may be the consequence of other time-evolving external factors, such as soil reflections. At the current data calibration stage, it is impossible to clearly distinguish the ionosphere's influence. Therefore, comparing data and simulations will be repeated as the MIST data calibration pipeline develops.

Finally, I compared the IRI and E-CHAIM TEC integrations with CDDIS TEC data derived from GNSS measurements. Although the discrepancies between the two approaches are considerably significant (up to ~ 14 TECU), they can be justified by different biases, such as DCB of GNSS or bias of climatological models of the ionosphere. The uncertainties in IRI and E-CHAIM are unpredictable and sometimes significant, excluding the possibility of using the ionosphere models for directly correcting the data from 21cm experiments.

Still, it can be helpful in simulations for studying the temporal and spectral impact of the ionosphere on antenna temperature.

6.3 Potential Improvements to the Model's Accuracy

We consider two different approaches for increasing the accuracy of the `dionpy`. The first suggests employing assimilative ionosphere models that use near-real-time data from satellites and ground stations to adjust the model to the short-scale temporal variations of the ionosphere. One existing assimilative version of IRI is IRI-based Real-Time Assimilative Model (IRTAM) (Reinisch et al., 2012), which was used for the development of Global Assimilative Modeling of Bottomside Ionospheric Timelines (GAMBIT)[4] - an online tool that provides access to IRTAM evaluations on data from GIRO[5]. The possibility of automatic GAMBIT data scrapping from Python was not explored yet but seems plausible with the condition of registered access account. The Assimilative Canadian High Arctic Ionospheric Model (A-CHAIM)[6] is based on E-CHAIM and implements a highly non-linear assimilation scheme utilizing data from different ground- and space-based sources. The A-CHAIM only provides information about near-real-time ionosphere for the last three hours. For retrospective evaluation of assimilative algorithms, the Reanalysis Canadian High Arctic Ionospheric Model (R-CHAIM)[7] was developed, which, unfortunately, is not maintained at the moment.

The second approach for improving the accuracy of `dionpy` is a comparison with the actual ionosphere measurements. For example, ISRs can be used to estimate the total attenuation coefficient of the ionosphere. In particular, the Resolute Bay Incoherent Scatter Radar - North (RISR-N)[8] is located at Resolute Bay in Canadian Arctic and points deep into the polar cap, covering the location of MIST deployment at MARS. We plan to

[4] https://giro.uml.edu/GAMBIT/
[5] https://giro.uml.edu/
[6] https://www.rspl.ca/index.php/projects/chaim/a-chaim
[7] https://chain-new.chain-project.net/index.php/projects/chaim/r-chaim
[8] https://amisr.com/amisr/about/resolute-bay-isrs/

access the RISR-N data in the future to compare it to (and, maybe, calibrate) the `dionpy` prediction.

Although the work on improving the `dionpy` code is ongoing, most results from this thesis (those that do not use unpublished MIST data) can be easily reproduced and modified. The code used for simulations in this work will be published in the "Examples" section on the `dionpy` website[9] soon.

[9] `https://dionpy.readthedocs.io/en/latest/`

Chapter 7

Summary

In this thesis, I presented the developed ionospheric absorption, emission and refraction model based on IRI - a climatological semi-empirical model of ionospheric electron density. I discussed all the details behind the implementation and outlined model limitations. I introduced the `dionpy` - an efficient Python implementation of the proposed model, which is open for public access.

The developed model opens new possibilities for advanced simulations of global 21cm cosmology experiments. Some examples of model applications (such as the impact of the ionosphere on simulated antenna temperature or temporal evolution of ionospheric effects) were shown and discussed in the scope of this work. The planned future work on model improvements includes: 1) incorporating a model of the Earth's magnetic field into `dionpy`; 2) exploring the possibility of using assimilative models of ionospheric electron density for improved accuracy. I also plan to perform more in-depth simulations using the current `dionpy` version to study the dynamical effects of the ionosphere, in particular in the context of the MIST experiment.

Appendix A

Impact of magnetic field in Appleton-Hartree equation

To estimate the impact of the magnetic field in Eq. 4.2, we use assumptions close to those used in Ved14 for the proper comparison. For the D-layer we assume $n_e = 5 \times 10^8$ m^{-3}, $\nu_c = 10$ MHz (Aggarwal et al., 1979), $B \approx 0.3$ G (estimated using IGRF (Alken et al., 2021)). The relative difference of the imaginary part of the refraction index in the D-layer is shown in Fig. A.1. The biggest noticeable difference occurs when the magnetic field is parallel to the wave vector, and the wave has left-hand circular polarization (which corresponds to "+" in the denominator). At low frequencies, the relative change is $\sim 40\%$ of the refraction factor, corresponding to a ~ 0.4 dB for typical daytime value of electron density in the D-layer.

For the F-layer we assume $n_e = 5 \times 10^{11}$ m^{-3}, $\nu_c = 10^{-3}$ MHz (Aggarwal et al., 1979), $B \approx 0.3$ G (estimated using IGRF). The result of the estimation is shown in Fig. A.2. Here, the biggest noticeable relative difference for the real part of the refraction index reaches $\sim 10^{-4}$, which agrees with Ved14.

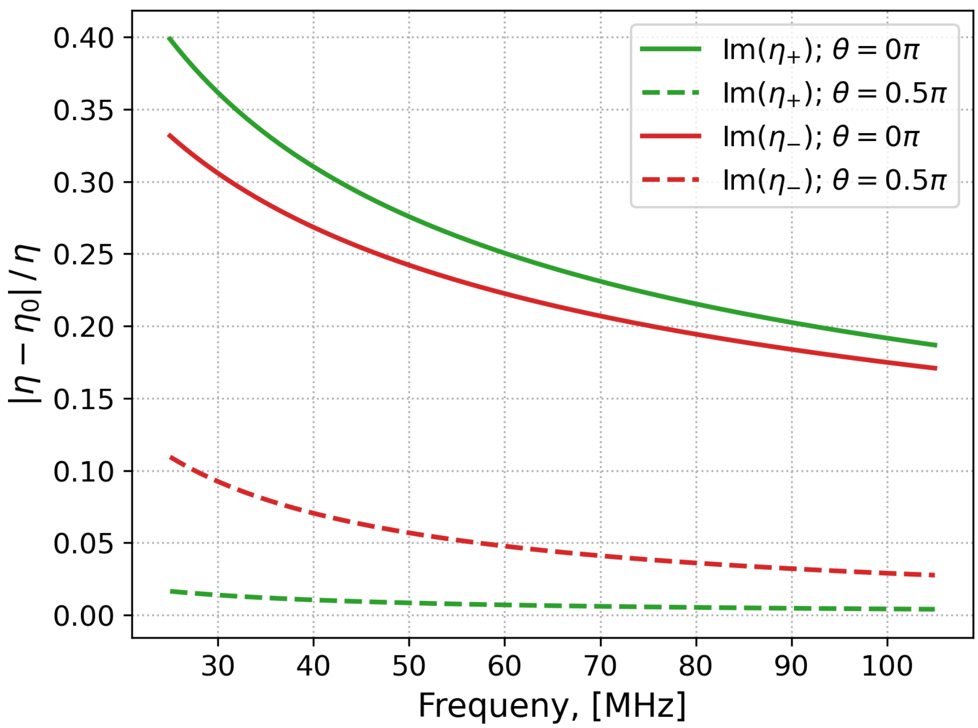

Figure A.1: Magnetic field impact on the imaginary part of the refraction index in the D-layer. The estimation was made for different polarizations and angles θ between the magnetic field and the wave vector. The η_+ corresponds to the plus sign in the denominator of Eq. 4.2 and η_- corresponds to the minus sign. For the estimation values $n_e = 5 \times 10^8$ m^{-3}, $\nu_c = 10$ MHz, $B \approx 0.3$ G were used.

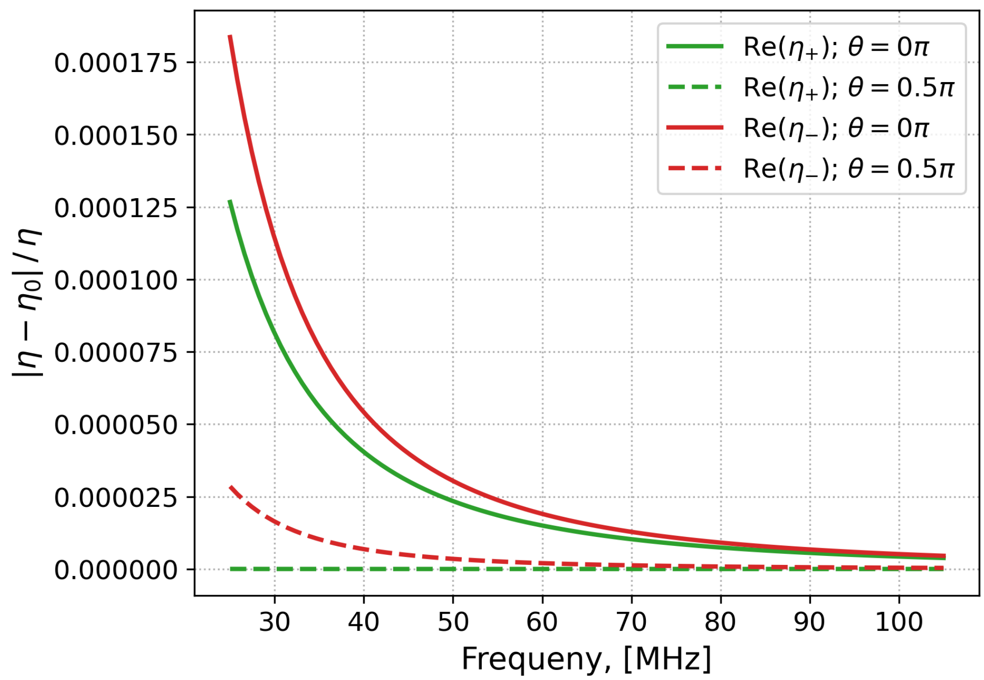

Figure A.2: Magnetic field impact on the real part of the refraction index in the F-layer. The estimation was made for different polarizations and angles θ between the magnetic field and the wave vector. The η_+ corresponds to the plus sign in the denominator of Eq. 4.2 and η_- corresponds to the minus sign. For the estimation values $n_e = 5 \times 10^{11}$ m^{-3}, $\nu_c = 10^{-3}$ MHz, $B \approx 0.3$ G were used.

Bibliography

Abdu, M., Batista, I., Reinisch, B., and Carrasco, A. (2004). Equatorial f-layer heights, evening prereversal electric field, and night e-layer density in the american sector: Iri validation with observations. *Advances in Space Research*, 34(9):1953–1965. IRI: Quantifying Ionospheric Variability.

Abdu, M. A. (2020). Chapter 12 - equatorial f region irregularities. In Materassi, M., Forte, B., Coster, A. J., and Skone, S., editors, *The Dynamical Ionosphere*, pages 169–178. Elsevier.

Aggarwal, K. M., Nath, N., and Setty, C. S. G. K. (1979). Collision frequency and transport properties of electrons in the ionosphere. Planet. Space Sci., 27(6):753–768.

Alken, P. et al. (2021). International Geomagnetic Reference Field: the thirteenth generation. *Earth, Planets and Space*, 73(1):49.

Altadill, D., Magdaleno, S., Torta, J., and Blanch, E. (2013). Global empirical models of the density peak height and of the equivalent scale height for quiet conditions. *Advances in Space Research*, 52(10):1756–1769. IRI Over the African Region.

Altadill, D., Torta, J., and Blanch, E. (2009). Proposal of new models of the bottom-side b0 and b1 parameters for iri. *Advances in Space Research*, 43(11):1825–1834. Ionosphere - Modelling, Forecasting, and Telecommunications I.

Appleton, E. V. and Barnett, M. A. F. (1925). On Some Direct Evidence for Downward Atmospheric Reflection of Electric Rays. *Proceedings of the Royal Society of London Series A*, 109(752):621–641.

Appleton, E. V. and Naismith, R. (1932). Some Measurements of Upper-Atmospheric Ionisation. *Proceedings of the Royal Society of London Series A*, 137(831):36–54.

Bale, S. D. et al. (2023). LuSEE 'Night': The Lunar Surface Electromagnetics Experiment. *arXiv e-prints*, page arXiv:2301.10345.

Barkana, R. (2018). Possible interaction between baryons and dark-matter particles revealed by the first stars. Nature, 555(7694):71–74.

Barkana, R. and Loeb, A. (2001). In the beginning: the first sources of light and the reionization of the universe. *Physics reports*, 349(2):125–238.

Berlin, A., Hooper, D., Krnjaic, G., and McDermott, S. D. (2018). Severely constraining dark-matter interpretations of the 21-cm anomaly. *Phys. Rev. Lett.*, 121:011102.

Bevins, H. T. J. et al. (2021). GLOBALEMU: A novel and robust approach for emulating the sky-averaged 21-cm signal from the cosmic dawn and epoch of reionisation. *arXiv:2104.04336 [astro-ph]*. arXiv: 2104.04336.

Bidula, V. (2022a). Ionosphere simulation with dionpy. Technical report, MIST collaboration. Available at `https://www.physics.mcgill.ca/mist/memos/MIST_memo_69.pdf`.

Bidula, V. (2022b). Optimization of the IRI2016 Ionosphere Model: the `iricore` package. Technical report, MIST collaboration. Available at `https://www.physics.mcgill.ca/mist/memos/MIST_memo_62.pdf`.

Bilitza, D. et al. (2022). The international reference ionosphere model: A review and description of an ionospheric benchmark. *Reviews of Geophysics*, 60(4):e2022RG000792. e2022RG000792 2022RG000792.

Bilitza, D. and Xiong, C. (2021). A solar activity correction term for the iri topside electron density model. *Advances in Space Research*, 68(5):2124–2137. International Reference Ionosphere - Progress and New Inputs.

Bowman, J. D. et al. (2018). An absorption profile centred at 78 megahertz in the sky-averaged spectrum. Nature, 555(7694):67–70.

Bradley, R. F., Tauscher, K., Rapetti, D., and Burns, J. O. (2019). A Ground Plane Artifact that Induces an Absorption Profile in Averaged Spectra from Global 21 cm Measurements, with Possible Application to EDGES. ApJ, 874(2):153.

Bye, C. H., Portillo, S. K. N., and Fialkov, A. (2022). 21cmVAE: A Very Accurate Emulator of the 21 cm Global Signal. ApJ, 930(1):79.

Chen, X. and Miralda-Escudé, J. (2008). The 21 cm signature of the first stars. *The Astrophysical Journal*, 684(1):18.

Cherniak, I., Zakharenkova, I., and Dzyubanov, D. (2013). Accuracy of iri profiles of ionospheric density and temperatures derived from comparisons to kharkov incoherent scatter radar measurements. *Advances in Space Research*, 51(4):639–646. Representation of the Auroral and Polar Ionosphere in the International Reference Ionosphere (IRI).

Chulliat, A. et al. (2020). The US/UK World Magnetic Model for 2020-2025: Technical Report. Technical report, NESDIS (National Environmental Satellite, Data, and Information Service) and NCEI (National Centers for Environmental Information).

Cohen, A., Fialkov, A., Barkana, R., and Lotem, M. (2017). Charting the parameter space of the global 21-cm signal. *Monthly Notices of the Royal Astronomical Society*, 472(2):1915–1931.

Cohen, A., Fialkov, A., Barkana, R., and Monsalve, R. A. (2020). Emulating the global 21-cm signal from Cosmic Dawn and Reionization. MNRAS, 495(4):4845–4859.

Datta, A. et al. (2014). Effects Of The Ionosphere On Ground-Based Detection Of The Global 21 CM Signal From The Cosmic Dawn And The Dark Ages. *arXiv e-prints*, page arXiv:1409.0513.

Datta, A. et al. (2016). The Effects of the Ionosphere on Ground-based Detection of the Global 21 cm Signal from the Cosmic Dawn and the Dark Ages. ApJ, 831(1):6.

Davies, K. (1990). *Ionospheric radio*. Number 31. IET.

de Lera Acedo, E. (2019). Reach: Radio experiment for the analysis of cosmic hydrogen. In *2019 International Conference on Electromagnetics in Advanced Applications (ICEAA)*, pages 0626–0629.

Dodelson, S. and Schmidt, F. (2020). *Modern cosmology*. Academic press.

Dowell, J. et al. (2017). The LWA1 Low Frequency Sky Survey. *Monthly Notices of the Royal Astronomical Society*, 469(4):4537–4550.

Dyson, T. et al. (2021). Radio-Frequency Interference at the McGill Arctic Research Station. *Journal of Astronomical Instrumentation*, 10(2):2150007–564.

Evans, J. V. and Hagfors, T. (1968). *Radar astronomy*.

Fejer, B. G., Jensen, J. W., and Su, S.-Y. (2008). Quiet time equatorial F region vertical plasma drift model derived from ROCSAT-1 observations. *Journal of Geophysical Research (Space Physics)*, 113(A5):A05304.

Fejer, B. G. and Maute, A. (2021). *Equatorial Ionospheric Electrodynamics*, chapter 9, pages 159–183. American Geophysical Union (AGU).

Feng, C. and Holder, G. (2018). Enhanced Global Signal of Neutral Hydrogen Due to Excess Radiation at Cosmic Dawn. ApJ, 858(2):L17.

Fialkov, A. and Barkana, R. (2019). Signature of excess radio background in the 21-cm global signal and power spectrum. MNRAS, 486(2):1763–1773.

Field, G. B. (1958). Excitation of the hydrogen 21-cm line. *Proceedings of the IRE*, 46(1):240–250.

Fixsen, D. J. (2009). The Temperature of the Cosmic Microwave Background. ApJ, 707(2):916–920.

Foster, J. C. et al. (2005). Multiradar observations of the polar tongue of ionization. *Journal of Geophysical Research (Space Physics)*, 110(A9):A09S31.

Friedrich, M., Pock, C., and Torkar, K. (2018). FIRI-2018, an Updated Empirical Model of the Lower Ionosphere. *Journal of Geophysical Research (Space Physics)*, 123(8):6737–6751.

Friedrich, M. and Torkar, K. M. (1992). An empirical model of the nonauroral d region. *Radio Science*, 27(06):945–953.

Fuller-Rowell, T., Araujo-Pradere, E., and Codrescu, M. (2000). An empirical ionospheric storm-time correction model. *Advances in Space Research*, 25(1):139–146. Lower Ionosphere: Measurements and Models.

Furlanetto, S. R., Oh, S. P., and Briggs, F. H. (2006). Cosmology at low frequencies: The 21 cm transition and the high-redshift Universe. Phys. Rep., 433(4-6):181–301.

Gnedin, N. Y. and Ostriker, J. P. (1997). Reionization of the universe and the early production of metals. *The Astrophysical Journal*, 486(2):581.

Golub, G. H. and Van Loan, C. F. (2013). *Matrix computations*. JHU press.

Górski, K. M. et al. (2005). HEALPix: A Framework for High-Resolution Discretization and Fast Analysis of Data Distributed on the Sphere. ApJ, 622(2):759–771.

Hecht, E. (2016). *Optics, Global Edition*. Pearson Education.

Hills, R., Kulkarni, G., Meerburg, P. D., and Puchwein, E. (2018). Concerns about modelling of the EDGES data. Nature, 564(7736):E32–E34.

Hirata, C. M. and Sigurdson, K. (2007). The spin-resolved atomic velocity distribution and 21-cm line profile of dark-age gas. *Monthly Notices of the Royal Astronomical Society*, 375(4):1241–1264.

Huang, Q.-Z., Wu, F.-Q., Ansari, R., and Chen, X. (2018). Extracting 21 cm signal by frequency and angular filtering. *Research in Astronomy and Astrophysics*, 18(9):114.

Hubble, E. (1929). A Relation between Distance and Radial Velocity among Extra-Galactic Nebulae. *Proceedings of the National Academy of Science*, 15(3):168–173.

Hunsucker, R. D. and Hargreaves, J. K. (2007). *The high-latitude ionosphere and its effects on radio propagation*. Cambridge University Press.

ISO-16457:2022 (2022). Space environment (natural and artificial) — The Earth's ionosphere model — International reference ionosphere (IRI) model and extensions to the plasmasphere. Standard, International Organization for Standardization, Geneva, CH.

Itikawa, Y. (1971). Effective collision frequency of electrons in atmospheric gases. Planet. Space Sci., 19(8):993–1007.

Itikawa, Y. (1973). Effective collision frequency of electrons in gases. *Physics of Fluids*, 16(6):831–835.

ITU-T (2017). Effects of tropospheric refraction on radiowave propagation. Recommendation P.834, International Telecommunication Union, Geneva.

Jarosik, N. et al. (2011). Seven-year Wilkinson Microwave Anisotropy Probe (WMAP) Observations: Sky Maps, Systematic Errors, and Basic Results. ApJS, 192(2):14.

Kumar, S. et al. (2014). Validation of the IRI-2012 model with GPS-based ground observation over a low-latitude Singapore station. *Earth, Planets and Space*, 66:17.

Leick, A., Rapoport, L., and Tatarnikov, D. (2015). *GPS satellite surveying*. John Wiley & Sons.

Li, G. et al. (2021). Challenges to Equatorial Plasma Bubble and Ionospheric Scintillation Short-Term Forecasting and Future Aspects in East and Southeast Asia. *Surveys in Geophysics*, 42(1):201–238.

Li, M. et al. (2018). Estimation and analysis of the short-term variations of multi-gnss receiver differential code biases using global ionosphere maps. *Journal of Geodesy*, 92:889–903.

Liu, A. and Shaw, J. R. (2020). Data Analysis for Precision 21 cm Cosmology. PASP, 132(1012):062001.

Liu, R. Y., Smith, P. A., and King, J. W. (1983). A new solar index which leads to improved foF2 predictions using the CCIR Atlas. *Telecommun. J*, 50(8):408–414.

Loeb, A. and Zaldarriaga, M. (2004). Measuring the small-scale power spectrum of cosmic density fluctuations through 21 cm tomography prior to the epoch of structure formation. *Phys. Rev. Lett.*, 92:211301.

Lühr, H., Alken, P., and Zhou, Y.-L. (2021). *The Equatorial Electrojet*, chapter 12, pages 281–299. American Geophysical Union (AGU).

McKinley, B. et al. (2020). The All-Sky SignAl Short-Spacing INterferometer (ASSASSIN) – I. Global-sky measurements with the Engineering Development Array-2. *Monthly Notices of the Royal Astronomical Society*, 499(1):52–67.

Menvielle, M. and Berthelier, A. (1991). The K-derived planetary indices - Description and availability. *Reviews of Geophysics*, 29:415–432.

Mertens, C. J. et al. (2013). Empirical storm-e model: Ii. geomagnetic corrections to nighttime ionospheric e-region electron densities. *Advances in Space Research*, 51(4):575–

598. Representation of the Auroral and Polar Ionosphere in the International Reference Ionosphere (IRI).

Miralda-Escudé, J. (2003). The dark age of the universe. *Science*, 300(5627):1904–1909.

Mirocha, J. (2014). Decoding the X-ray properties of pre-reionization era sources. MNRAS, 443(2):1211–1223.

Mirocha, J., Furlanetto, S. R., and Sun, G. (2017). The global 21-cm signal in the context of the high- z galaxy luminosity function. MNRAS, 464(2):1365–1379.

Mirocha, J. et al. (2018). Unique signatures of Population III stars in the global 21-cm signal. MNRAS, 478(4):5591–5606.

Mirocha, J., Skory, S., Burns, J. O., and Wise, J. H. (2012). Optimized Multi-frequency Spectra for Applications in Radiative Feedback and Cosmological Reionization. ApJ, 756(1):94.

Monsalve, R. A. (2023). Private Communication.

Monsalve, R. A. et al. (2023). Mapper of the IGM Spin Temperature (MIST): Instrument Overview. [Manuscipt in preparation].

Monsalve, R. A. et al. (2021). Absolute Calibration of Diffuse Radio Surveys at 45 and 150 MHz. ApJ, 908(2):145.

Monsalve, R. A., Rogers, A. E. E., Bowman, J. D., and Mozdzen, T. J. (2017). Calibration of the EDGES High-band Receiver to Observe the Global 21 cm Signature from the Epoch of Reionization. ApJ, 835(1):49.

Montenbruck, O., Hauschild, A., and Steigenberger, P. (2014). Differential code bias estimation using multi-gnss observations and global ionosphere maps. *Navigation: Journal of the Institute of Navigation*, 61(3):191–201.

Mozdzen, T. J., Bowman, J. D., Monsalve, R. A., and Rogers, A. E. E. (2017). Improved measurement of the spectral index of the diffuse radio background between 90 and 190 MHz. MNRAS, 464(4):4995–5002.

Mozdzen, T. J. et al. (2019). Spectral index of the diffuse radio background between 50 and 100 MHz. MNRAS, 483(4):4411–4423.

Muñoz, J. B. and Loeb, A. (2018). Insights on Dark Matter from Hydrogen during Cosmic Dawn. *arXiv e-prints*, page arXiv:1802.10094.

Mylnikova, A., Yasyukevich, Y., Kunitsyn, V., and Padokhin, A. (2015). Variability of gps/glonass differential code biases. *Results in Physics*, 5:9–10.

Nava, B., Coïsson, P., and Radicella, S. (2008). A new version of the nequick ionosphere electron density model. *Journal of Atmospheric and Solar-Terrestrial Physics*, 70(15):1856–1862. Ionospheric Effects and Telecommunications.

Noll, C. E. (2010). The crustal dynamics data information system: A resource to support scientific analysis using space geodesy. *Advances in Space Research*, 45(12):1421–1440. DORIS: Scientific Applications in Geodesy and Geodynamics.

Norton, K. (1941). The calculation of ground-wave field intensity over a finitely conducting spherical earth. *Proceedings of the IRE*, 29(12):623–639.

Patra, N., Subrahmanyan, R., Raghunathan, A., and Udaya Shankar, N. (2013). SARAS: a precision system for measurement of the cosmic radio background and signatures from the epoch of reionization. *Experimental Astronomy*, 36(1-2):319–370.

Peebles, P. J. E. (1993). *Principles of physical cosmology*, volume 27. Princeton university press.

Penzias, A. A. and Wilson, R. W. (1965). A Measurement of Excess Antenna Temperature at 4080 Mc/s. ApJ, 142:419–421.

Planck Collaboration et al. (2020a). Planck 2018 results. I. Overview and the cosmological legacy of Planck. A&A, 641:A1.

Planck Collaboration et al. (2020b). Planck 2018 results. VI. Cosmological parameters. A&A, 641:A6.

Pritchard, J. R. and Furlanetto, S. R. (2006). Descending from on high: Lyman-series cascades and spin-kinetic temperature coupling in the 21-cm line. MNRAS, 367(3):1057–1066.

Pritchard, J. R. and Loeb, A. (2012). 21 cm cosmology in the 21st century. *Reports on Progress in Physics*, 75(8):086901.

Raghunathan, A. et al. (2021). A floating octave bandwidth cone-disk antenna for detection of cosmic dawn. *IEEE Transactions on Antennas and Propagation*, 69(10):6209–6217.

Rawer, K., Bilitza, D., and Ramakrishnan, S. (1978). Goals and status of the international reference ionosphere. *Reviews of Geophysics and Space Physics*, 16:177–181.

Rawer, K., Lincoln, J., and Conkright, R. (1981). International Reference Ionosphere–IRI 79. *World Data Center A for Solar-Terrestrial Physics, Report UAG-82, Boulder, Colorado*, 245:245.

Razoumov, A. O., Norman, M. L., Abel, T., and Scott, D. (2002). Cosmological hydrogen reionization with three-dimensional radiative transfer. *The Astrophysical Journal*, 572(2):695.

Reinisch, B. W., Huang, X., Galkin, I., and Bilitza, D. (2012). A Real-Time Assimilative Model for IRI. In *EGU General Assembly Conference Abstracts*, EGU General Assembly Conference Abstracts, page 12828.

Richards, P. G., Bilitza, D., and Voglozin, D. (2010). Ion density calculator (IDC): A new efficient model of ionospheric ion densities. *Radio Science*, 45(5):RS5007.

Rogers, A. E. E. and Bowman, J. D. (2012). Absolute calibration of a wideband antenna and spectrometer for accurate sky noise temperature measurements. *Radio Science*, 47(4):RS0K06.

Rogers, A. E. E. et al. (2015). Radiometric measurements of electron temperature and opacity of ionospheric perturbations. *Radio Science*, 50(2):130–137.

Rybicki, G. B. (2006). Improved Fokker-Planck Equation for Resonance-Line Scattering. ApJ, 647(1):709–718.

Rybicki, G. B. and Lightman, A. P. (1986). *Radiative Processes in Astrophysics*.

Santos, M. G. and Cooray, A. (2006). Cosmological and astrophysical parameter measurements with 21-cm anisotropies during the era of reionization. *Phys. Rev. D*, 74:083517.

Shen, E. et al. (2021). Quantifying ionospheric effects on global 21-cm observations. MNRAS, 503(1):344–353.

Shkarofsky, I. P. (1961). Generalized appleton-hartree equation for any degree of ionization and application to the ionosphere. *Proceedings of the IRE*, 49(12):1857–1871.

Shkarofsky, I. P., Bachynski, M. P., and Johnston, T. W. (1961). Collision frequency associated with high temperature air and scattering cross-sections of the constituents. Planet. Space Sci., 6:24–46.

Shubin, V. (2015). Global median model of the f2-layer peak height based on ionospheric radio-occultation and ground-based digisonde observations. *Advances in Space Research*, 56(5):916–928.

Singh, S. et al. (2022). On the detection of a cosmic dawn signal in the radio background. *Nature Astronomy*, 6:607–617.

Singh, S. and Subrahmanyan, R. (2019). The redshifted 21 cm signal in the edges low-band spectrum. *The Astrophysical Journal*, 880(1):26.

Spinelli, M. et al. (2021). Spectral index of the Galactic foreground emission in the 50-87 MHz range. MNRAS, 505(2):1575–1588.

The HDF Group (1997-2023). Hierarchical Data Format, version 5. https://www.hdfgroup.org/HDF5/.

Thekkeppattu, J. N. et al. (2022). System design and calibration of sitara—a global 21 cm short spacing interferometer prototype. *Publications of the Astronomical Society of Australia*, 39:e018.

Themens, D. R., Jayachandran, P., and Langley, R. B. (2015). The nature of gps differential receiver bias variability: An examination in the polar cap region. *Journal of Geophysical Research: Space Physics*, 120(9):8155–8175.

Themens, D. R. and Jayachandran, P. T. (2016). Solar activity variability in the IRI at high latitudes: Comparisons with GPS total electron content. *Journal of Geophysical Research (Space Physics)*, 121(4):3793–3807.

Themens, D. R. et al. (2018). Topside Electron Density Representations for Middle and High Latitudes: A Topside Parameterization for E-CHAIM Based On the NeQuick. *Journal of Geophysical Research (Space Physics)*, 123(2):1603–1617.

Themens, D. R., Jayachandran, P. T., Galkin, I., and Hall, C. (2017). The Empirical Canadian High Arctic Ionospheric Model (E-CHAIM): N_mF_2 and h_mF_2. *Journal of Geophysical Research (Space Physics)*, 122(8):9015–9031.

Themens, D. R. et al. (2019). A Bottomside Parameterization for the Empirical Canadian High Arctic Ionospheric Model. *Radio Science*, 54(5):397–414.

Themens, D. R., Jayachandran, P. T., Nicolls, M. J., and MacDougall, J. W. (2014). A top to bottom evaluation of IRI 2007 within the polar cap. *Journal of Geophysical Research (Space Physics)*, 119(8):6689–6703.

Themens, D. R. et al. (2021). E-chaim as a model of total electron content: Performance and diagnostics. *Space Weather*, 19(11):e2021SW002872.

Themens, D. R. et al. (2022). New Features for the Empirical Canadian High Arctic Ionospheric Model (E-CHAIM) v4.0.0. In *AGU Fall Meeting Abstracts*, volume 2022, pages SM52C–1428.

Thompson, A. R., Moran, J. M., and Swenson, G. W. (2017). *Interferometry and synthesis in radio astronomy*. Springer Nature.

Truhlik, V., Bilitza, D., and Triskova, L. (2012). A new global empirical model of the electron temperature with the inclusion of the solar activity variations for IRI. *Earth, Planets and Space*, 64(6):531–543.

Truhlik, V., Bilitza, D., and Triskova, L. (2015). Towards better description of solar activity variation in the international reference ionosphere topside ion composition model. *Advances in Space Research*, 55(8):2099–2105. INTERNATIONAL REFERENCE IONOSPHERE AND GLOBAL NAVIGATION SATELLITE SYSTEMS.

Vedantham, H. K. et al. (2014). Chromatic effects in the 21 cm global signal from the cosmic dawn. MNRAS, 437(2):1056–1069.

Warnant, R. (1997). Reliability of the tec computed using gps measurements—the problem of hardware biases. *Acta Geodaetica et Geophysica Hungarica*, 32:451–459.

Watson, C. et al. (2011). GPS TEC technique for observation of the evolution of substorm particle precipitation. *Journal of Geophysical Research (Space Physics)*, 116(A10):A00I90.

Wouthuysen, S. A. (1952). On the excitation mechanism of the 21-cm (radio-frequency) interstellar hydrogen emission line. AJ, 57:31–32.

Xiong, C., Lühr, H., and Ma, S. (2013). The subauroral electron density trough: Comparison between satellite observations and iri-2007 model estimates. *Advances in Space Research*, 51(4):536–544. Representation of the Auroral and Polar Ionosphere in the International Reference Ionosphere (IRI).

Yizengaw, E. et al. (2008). Global plasmaspheric tec and its relative contribution to gps tec. *Journal of Atmospheric and Solar-Terrestrial Physics*, 70(11):1541–1548.

Zahn, O. et al. (2007). Simulations and analytic calculations of bubble growth during hydrogen reionization. *The Astrophysical Journal*, 654(1):12.

Zaldarriaga, M., Furlanetto, S. R., and Hernquist, L. (2004). 21 centimeter fluctuations from cosmic gas at high redshifts. *The Astrophysical Journal*, 608(2):622.

Zhang, Y., Paxton, L. J., Bilitza, D., and Doe, R. (2010). Near real-time assimilation in iri of auroral peak e-region density and equatorward boundary. *Advances in Space Research*, 46(8):1055–1063. International Reference Ionosphere – Progress in Ionospheric Modelling.

Zumberge, J. et al. (1997). Precise point positioning for the efficient and robust analysis of gps data from large networks. *Journal of geophysical research: solid earth*, 102(B3):5005–5017.